2015

Uncertainty Analyses of Climate Change Impact on Hydrologic Projections

Ehsan Beigi
Louisiana State University and Agricultural and Mechanical College, ehsbeigi@gmail.com

UNCERTAINTY ANALYSES OF CLIMATE CHANGE IMPACT ON HYDROLOGIC PROJECTIONS

A Dissertation

Submitted to the Graduate Faculty of the
Louisiana State University and
Agricultural and Mechanical College
in partial fulfillment of the
requirements for the degree of
Doctor of Philosophy

in

The Department of Civil and Environmental Engineering

by
Ehsan Beigi
B.S., Isfahan University of Technology, 2005
M.S., Sharif University of Technology, 2010
May 2015

For My Family and Friends

and Anybody Else That Has

Missed Me for the Past Four Years

Acknowledgments

I would like to express my sincere gratitude to my advisor, Dr. Frank Tsai, for his excellent guidance, support, and supervision throughout all the stages of this dissertation.

I am thankful to my Ph.D. committee members, Dr. John Pardue, Dr. Clinton Willson, Dr. Yijun Xu and Dr. Shih-Chieh Kao for their time and support.

Special thanks goes to my friends and colleagues in Dr. Tsai's research group students Dr. Ahmed Ellshall, Dr. Nima Chitsazan, Mr. Hai Pham, and Mr. Amir Mani for their support and help during the last four years.

I want to give my thanks to LSU HPC and LONI for providing great computational facilities. My acknowledgments go to the U.S. Geological Survey–National Institute for Water Resources and the Louisiana Water Resources Research Institutes for providing financial resources for this study. We acknowledge the World Climate Research Programme's Working Group on Coupled Modelling, which is responsible for CMIP, and we thank the climate modeling groups (listed in Table 5.1) for producing and making available their model output. For CMIP, the U.S. Department of Energy's Program for Climate Model Diagnosis and Intercomparison provides coordinating support and led development of software infrastructure in partnership with the Global Organization for Earth System Science Portals.

Finally and most importantly, I want to thank my family members for their kindness and support during the past four years. I would like to dedicate this Doctoral dissertation to my father, Mohammad Taghi, the kindest, most supportive, generous and peaceful person I have ever met in my life.

Table of Contents

Abstract

This study conducts uncertainty analysis on future region-scale hydrologic projections under the uncertain climate change projections of the IPCC Fifth and Forth Assessment Reports. The hierarchical Bayesian model averaging (HBMA) method is adopted to segregate and prioritize sources of climate projection uncertainty, obtain ensemble mean of hydrologic projection, and quantify the hydrologic projection uncertainty arising from individual uncertainty sources. This study deals with the choices of greenhouse gas (GHG) concentration trajectories, global climate models (GCMs), and GCM initial conditions as three major uncertainty sources in downscaled precipitation and temperature projections. The method is applied to investigate future hydrologic projections in southwestern Mississippi and southeastern Louisiana. Six sets and 133 sets of 1/8-degree-BCCA-downscaled daily precipitation and temperature projections, respectively, from CMIP3 and CMIP5 climate projections, are used as inputs to the hydrologic model HELP3 to project surface runoff, evapotranspiration and groundwater recharge from 2010 to 2099. The 6 sets derived from B1, A2 and A1FI emission scenarios of the PCM and GFDL models and the 133 sets derived from four emission paths, 21 CMIP5 GCMs, and different number of GCM initial conditions. The results show that future recharge in southwestern Mississippi and southeastern Louisiana is more sensitive to climate projections and exhibits much higher variability than runoff and evapotranspiration. In general, future recharge is projected to increase in next several decades and has great uncertainty toward the end of the century. Runoff is likely to decrease while evapotranspiration is likely to increase in the next century. The major hydrological projection uncertainty comes from the use of different GCMs. Contribution of uncertain GCM initial conditions to hydrologic projections uncertainty reduces over time as contribution from emission path uncertainty becomes more evident.

1. Introduction

1.1. Literature Review

1.1.1. Climate Change

Increases in global average air and ocean temperatures, extensive melting of snow and ice and rising global average sea level indicate that the Earth's climate is changing. Climate change is a change in the statistical properties of the climate system over long periods of time (i.e., decades to millions of years). According to the Fifth Assessment Report (AR5) of the Intergovernmental Panel on Climate Change (IPCC), “Not only is climate change happening, but every continent on earth is now experiencing its impacts”. The Earth average temperature has risen 0.8 °C over the past century and is projected to increase as much as 6 ºC over the next century. This increase caused by climate change might not seem a lot, however, it can have severe effects considering that the fact that the average Earth temperature during the last Ice Age was about 4−8 ºC lower than it is today (Stocker et al. 2013).

The IPCC in its fourth assessment (AR4) reported that climate change is primarily caused by human activities through increasing concentrations of greenhouse gases (CHG) in the atmosphere (e.g. use of fossil fuels, agriculture, and deforestation). The greenhouse gases trap heat (energy) in the lower part of the atmosphere. Increasing greenhouse gases to the atmosphere will trap more heat, which results in higher air temperatures, change in the amount and pattern of precipitation, increase of the frequency and severity of extreme climate events, droughts, increased danger of wildland fires, and so on. Future climate change and its consequential impacts will differ from region to region across the globe (Bates et al. 2008). Climate change is likely to bring about major disruptions on many ecosystems and human life and activities. Rising sea levels due to the melting of the polar ice caps may increase coastal erosion and submergence

of low-lying island regions and inhabited areas. This can result in massive migration of population as an adaptive response to climate change (Goderniaux et al. 2009).

Climate change issues have actually raised awareness in societies and political leadership around the world. International environmental treaties related to climate change have urged political will of government leaders, business community leaders, and civil society leaders to ensure the reduction of greenhouse gases emissions in their agenda. In 1992, world leaders and citizens of 176 countries gathered to develop the United Nations Framework Convention on Climate Change (UNFCCC), which main objective was to stabilize greenhouse gas concentrations in the atmosphere at a level that would prevent dangerous anthropogenic interference with the climate system. In 1997, The Kyoto Protocol extends the 1992 UNFCCC that parties agreed to reduce greenhouse gas on an average 5% compared to 1990 emissions over the period 2008-2012. In 2014, the post-Kyoto legal framework obligated all major polluters to pay for CO_2 emissions (UNFCCC, 2015).

One possible response to climate change is known as the climate change mitigation, which includes (GHG) emissions reduction. Climate change adaptation is another policy response to offset the effects of climate change, which includes reducing the vulnerability of social and biological systems to climate change by planning for the changes that are expected to occur. Climate change also indirectly threatens water as one of key natural resources, which is evidently vital for human life and activities and associated food security issues worldwide (Stocker et al. 2013).

1.1.2. Climate Change Impact on Hydrological Projections

Significantly increased emissions of greenhouse gases from anthropogenic activities has caused climate to change (Solomon et al. 2007). As reported by the IPCC, the global mean

surface temperature and the global mean sea level have risen by 0.6±0.2 °C and by 20±5 cm, respectively since the late 19th century. Additionally, the IPCC predicted 2 to 4 °C global temperature increase and 18 to 59 cm sea level rise in the 21st century (Stocker et al. 2013). The global warming is projected to intensify the global hydrologic cycle, alter precipitation amount, pattern and intensity, increase atmospheric water vapor, evaporation and evapotranspiration, and change groundwater recharge and runoff (Huntington, 2006).

Climate variation can impact on availability of groundwater through evapotranspiration and recharge processes (Bates et al. 2008). Because precipitation and surface water are the main sources to recharge aquifers, evaluating the impact of climate change on groundwater systems needs reliable estimation of recharge (Goderniaux et al. 2009), which is important for assessing drought, water quality, groundwater availability and sustainability (Alley 2001). Improving the understanding and modelling of climate changes on groundwater recharge has been highlighted in the last five IPCC reports (Houghton et al. 1996; Watson et al. 1998; Leonard et al. 1999; McCarthy et al. 2001; Bates et al. 2008; Stocker et al. 2013). Recently, the increasing number of climate change studies with regard to groundwater resources has shown the importance of this subject (e.g., Allen et al. 2010; Crosbie et al. 2010; Jackson e al. 2011; Ali et al. 2012; Barthel et al. 2012; Hiscock et al. 2012; Holman et al. 2012; Scott et al. 2012; Stoll et al. 2011; Raposo et al. 2013).

Knowledge of groundwater recharge under climate change is particularly vital to the areas where groundwater is the major source of water supply. Recharge plays a major role in groundwater availability as well as for evaluating aquifer vulnerability to contamination (Scanlon et al. 2002a). Reliable recharge estimation is important for efficient and sustainable groundwater resource management (Sophocleous 1991; Scanlon et al. 2002b) and for aquifer

protection from rapidly expanding urbanization, drought or climate change (Dripps and Bradbury 2007).

Aquifers are recharged through either direct infiltration of precipitation, leakage from surface water bodies such as streams and lakes, or human-induced activities such as urbanization or irrigation (Lerner et al. 1990). Hence, many factors affect recharge including climate variables such as precipitation and evaporation (Fitts 2002) and the attributes of land surface, topography, vegetation cover, and land use. In addition, recharge is controlled by existing soil moisture stored in the soil profile and by aquifer hydraulic properties (Makanjuola et al. 2012). Also, recharge rates can be significantly influenced by human-induced activities (Lerner 2002). This study estimates potential recharge due to infiltration of precipitation, which is known as diffuse recharge (Healy 2010). Assessing recharge rate is one of the most challenging issues in groundwater investigations. A variety of methods have been used to estimate groundwater recharge (Allison 1988; Allison et al. 1994; De Vries and Simmers, 2002; Gee and Hillel, 1988; Lerner et al. 1990; Scanlon et al. 2002a). The required spatial and temporal scales in addition to the objectives of the recharge assessment determine the appropriate techniques for quantifying recharge at a particular site (Scanlon et al. 2002a).

Groundwater recharge is stated as the process of replenishing the groundwater reservoir through either direct infiltration of precipitation or by leakage from surface bodies like streams, lake or via human-induced activities such as urbanization or irrigation. The recharge refers to the process of downward movement of water within unsaturated zones until the water table is reached (Lerner et al. 1990). In this study recharge from infiltration of precipitating is considered, which is referred either as diffuse recharge (Healy 2010), or direct recharge (Simmers et al. 1997). As precipitated water moves from the surface through the unsaturated

zone a percentage will be removed by evaporation, some will be drawn by plants (evapotranspiration), and some will store within the unsaturated zone. The remaining water will continue infiltrating deeper into the underlying soil layers, which will eventually reach to saturated groundwater zone and become groundwater recharge. Groundwater recharge is affected by many aspects including climatic factors such as the amount and intensity of rainfall and evaporation (Fitts 2002). Also, the characteristics of the land surface including topography, the type and amount of vegetation cover, and the nature of land use influence the recharge. In addition, recharge is controlled by existing soil moisture stored in the soil profile from previous rainfall events and also aquifer hydraulic properties to capture and transmit water (Makanjuola et al. 2012). Additionally, human activities and the increasing of residential developments can significantly affect recharge rates. Although it may be broadly recognized that urban development reduces the recharge rates through growing impervious surfaces, leakage from water and wastewater mains, and over irrigation of lawns and parks result in a potential increase on recharge rates to the groundwater, called urban recharge (Lerner 2002).

However, estimating the rate of aquifer replenishment is probably one of the most difficult elements to measure in the evaluation of ground water resources. Various techniques have been used to estimate groundwater recharge as noted in other reviews (Allison et al. 1994; De Vries and Simmers 2002; Gee and Hillel 1988; Lerner et al. 1990; Scanlon et al. 2002a). Robust estimation of recharge and the ensuring sustainable use of groundwater resources rely on choosing the suitable methods fitted to local conditions. Moreover, groundwater recharge assessing techniques have been categorized into surface water, unsaturated, and saturated-zone procedures; and each of these cases include physical, tracer and numerical modeling methods. The determination of appropriate techniques for quantifying recharge in a particular site depends

on the required spatial and temporal scales and also on the objectives of the recharge assessment (Scanlon et al. 2002a).

This study focuses on groundwater recharge estimation, runoff and evapotranspiration in humid areas, which are generally characterized by shallow water tables and have dominant downward movement into the unsaturated zone. Due to the higher precipitation than evapotranspiration, the water budget method for estimating groundwater recharge is more useful in humid regions. Aquifer recharge from direct percolation of precipitation to the water table is dominant and aquifer recharge from stream flow and lakes is less significant because groundwater discharges to streams and lakes, and recharge from surface water bodies can only occur during periods when stream stages are above the water level in the aquifer system (Simmers 1987). Contrary to humid areas, in dry regions recharge comprises a smaller portion of the water budget and the recharge term contains a cumulative error resulting from subtracting of all other large terms of the water budget method. Therefore, water budget approaches are generally more accurate in humid regions than in semiarid and arid regions (Gee and Hillel 1988). Consequently, application of the water budget method, for example the HELP3 model (Schroeder et al. 1994), for estimating recharge in a humid area such as the area of the Southern Hills aquifer system can be justified. However, HELP3 is not a proper model for estimating groundwater recharge in semi-arid and arid regions, where the magnitude of the recharge rate is small relative to that of the other components, in particular evapotranspiration, in the water budget equation (Scanlon et al. 2002a). Moreover, HELP3 does not account for the upward movement of water below the root zone, which can be significant in dry areas (Toews and Allen 2009).

Most of the climate change impact studies on groundwater recharge, runoff and evapotranspiration focused on quantifying direct effects of either discrete perturbations of precipitation and temperature patterns or downscaled outputs from global climate models (GCMs) to the regional resolution. These studies have used a wide range of modeling techniques, including (1) empirical models that represent groundwater recharge as linear functions of precipitation and temperature (e.g., Aguilera and Murillo 2009; Chen et al. 2002; Kruger et al. 2001; Serrat-Capdevilla et al. 2007), (2) physically based soil water balance models (e.g., Bouraoui et al. 1999; Crosbie et al. 2010; Jyrkama and Sykes 2007; Mileham et al. 2009; McCallum et al. 2010; Ng et al. 2010; Vaccaro 1992), (3) groundwater flow models (e.g., Allen et al. 2004; Brouyere et al. 2004; Dawes et al. 2012; Goderniaux et al. 2009; Kirshen 2002; Scibek and Allen 2006; Toews and Allen 2009; Yusoff et al. 2002; Woldeamlak et al. 2007), and (4) conceptual models of the streamflow (e.g., Cooper et al. 1995; Croley and Luukkonen 2003; Eckhardt and Ulbrich 2003; Loaiciga et al. 2000; Loaiciga 2003; Neukum and Azzam 2012).

1.1.3. Uncertainty of Climate Projections

The IPCC Fifth Assessment Report (AR5) and the U.S. National Climate Assessment Report have not adequately addressed the issue of uncertainty in assessments and projections of climate change (Katz et al., 2013). The need to carefully characterize and quantify uncertainty in climate change projections is essential not only for detection and attribution purposes, but also for effective climate change adaptation and mitigation strategies (Solomon et al., 2007). The future climate projections from global climate models (GCMs) are an important tool in tracing the impacts of anthropogenic forcings in the Earth's climate. However, these GCM projections are subjected to considerable uncertainties derived from three main sources: model uncertainty, scenario uncertainty and internal variability (Yip et al., 2011). Model uncertainty stems from

inaccuracies in the climate models due to an imperfect understanding and representation of complex physical, chemical, biological and other processes of climate system. Additionally, model uncertainty arises when different models response differently to the same external forcing due to the differences in model structures (e.g. physical and numerical formulations). Scenario uncertainty occurs because of insufficient knowledge about future greenhouse gases (GHG) emissions and other external forcings that influence the climate system. The internal variability which is the fluctuation of natural processes within the climate system that occurs without external forcing's effect (Deser et al., 2012). The outputs from GCMs are used as inputs to hydrological models to investigate the hydrological impacts of climate change for global and regional water resources. In addition to the uncertainty associated with future projections of climate, there are other sources of uncertainty such as downscaling method and hydrological model uncertainty. However, uncertainties resulting from GCMs and GHG emissions, generally have been given more attention as the major sources of uncertainty in quantifying the climate change impacts on hydrology (Chen et al., 2011). There have been a growing number of studies to evaluate overall uncertainty of projected climate impacts on hydrology using combination of emission scenarios, climate models, downscaling methods and hydrological models (e.g., Wilby and Harris, 2006; Déqué et al., 2007; Kay et al., 2009; Görgen et al., 2010; Chen et al., 2012; Habets et al., 2013).

Using a single model likely underestimates prediction uncertainty and tends to statistically biased modeling. Due to inaccuracy of each individual GCM, no single model can be declared as the best model; hence, future projections should exhibit the results of all GCMs (Knutti et al., 2010; McAvaney et al., 2001). It is generally believed that multi-model ensemble of GCMs often provides additional and more reliable information with higher confidence than

any single GCM and the average of a multi-model ensemble agrees more with climate observations than any single model (Gleckler et al., 2008; Pierce et al., 2009; Knutti et al., 2010). The IPCC suggests using multi-model ensembles for detection and attribution as well as for impact and adaptation studies, and provides recommendations for good practice on assessing and combining multi-model climate projections (Stocker et al., 2010). The spread of multi-model ensembles can assist in characterizing uncertainty, which demands understanding how the variation across an ensemble was produced. Weighting models according to some measure of skill might increase the reliability of projections. Recent studies have aimed to improve the credibility of projections and to quantify uncertainties more accurately by using a weighted average of a multi-model ensemble, where weights are defined based on model performance in simulating historical climate (Doblas-Reyes et al., 2003; Yun et al., 2003; Schmittner et al., 2005; Connolley and Bracegirdle, 2007; Murphy et al., 2007; Tebaldi and Knutti, 2007; Waugh and Eyring, 2008).

Bayesian model averaging (BMA) (Hoeting et al., 1999) is a robust multi-model method to combine multiple prediction models and conduct uncertainty analysis. The BMA predictive probability density function (PDF) of a quantity of interest is a weighted average of the individual model PDFs, which weights are obtained from corresponding posterior model probability of each model. The BMA predictive variance decomposes into two components, corresponding to between-model variance and within-model variance. BMA has been successfully implemented to provide reliable prediction and to conduct uncertainty analysis in various studies, such as weather forecasting (e.g., Raftery et al., 2005; Tebaldi et al., 2005; Min et al., 2007; Buser et al., 2009; Smith et al., 2009), inverse groundwater modeling (e.g., Tsai and Li, 2008a,b; Li and Tsai, 2009), and hydrological prediction (e.g., Ajami et al., 2007, Duan et al.,

2007; Vrugt et al., 2007; Zhang et al., 2009; Najafi et al., 2010; Dong et al., 2013; Liang et al., 2013). BMA has shown better performance compared to other multi-model methods (e.g., Bernardo et al., 1999; Raftery et al., 2003). However, the BMA framework does not quantify contributions of individual sources of uncertainty to total prediction uncertainty, whereas addressing this issue is very important for a thorough uncertainty analysis (Wagener and Gupta 2005). Li and Tsai (2009) and Tsai (2010) developed a new BMA formulation to discuss individual impacts of two sources of model uncertainty in groundwater prediction and remediation designs. Thereafter, Tsai and Elshall (2014) generalized the formulation and developed a hierarchical Bayesian model averaging (HBMA) method to analyze uncertainty from different types of groundwater model components. HBMA systematically segregates and prioritizes distinct sources of uncertainty in a hierarchical structure known as BMA trees for analyzing model uncertainty and uncertainty propagation for model prediction.

1.2. The Scope of the Dissertation

Figure 1.1 shows the schematic diagram of this research. The ultimate goals of the research are to quantify the uncertainty in the hydrological projections under climate change and to understand the impact of the climate change on hydrology of southwestern Mississippi and southeastern Louisiana. The uncertainties in future hydrological projections arising from climate modeling and emission path is investigated. However, uncertainties associated with hydrological model (parameter uncertainly and structural uncertainty) is not discussed in this study.

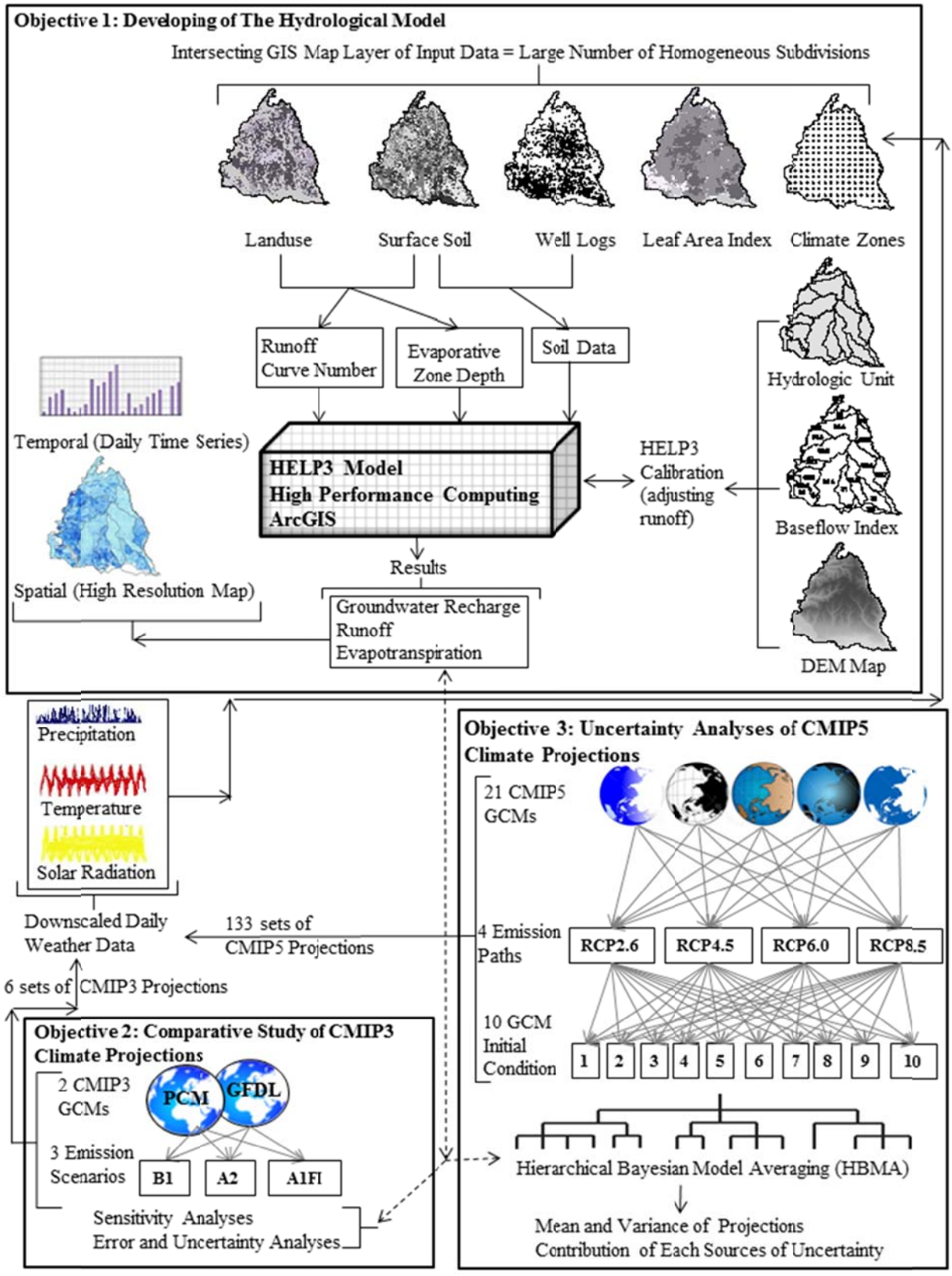

Figure 1.1: The schematic diagram of research

The first goal of this research is to develop a hydrological model to estimate groundwater recharge, surface runoff and evapotranspiration in large-scale humid regions. To this end, a water budget framework using HELP3 (Schroeder et al. 1994) coupled with a geographic information system (GIS) is developed. The framework is applied to the area of the Southern Hills aquifer system, southeastern Louisiana and southwestern Mississippi, which is shown in Figure 1.2. To obtain high spatial resolution hydrologic predictions, the study area was divided into a large number of subdivisions (286,355) using GIS by intersecting the vector-based maps of surficial soil type, land use/land cover, leaf area index, topographic slope, lithology, base flow index, HUC8, and climate zones. Each subdivision has homogeneous model parameters for HELP3.

The second goal of this research is to implement a comparative study of CMIP3 climate projections on hydrology of the Southern Hills aquifer system. Therefore, the aforementioned developed water budget framework in first objective was linked with three different emission scenarios of two CMIP3 GCMs to estimate potential recharge, surface runoff and evapotranspiration under high performance computing. The downscaled daily precipitation and temperature projections are input to a hydrological model, HELP3 (Schroeder et al. 1994), to project future surface runoff, evapotranspiration and groundwater recharge. The historical condition in 1950-2009 is used as a baseline and is compared to the results of six climate change scenarios for three future periods: 2010-2039, 2040-2069 and 2070-2099.

The final and the most important goal of the research is to adopt the hierarchical Bayesian model averaging (HBMA) method to analyze climate modeling uncertainty and emission scenario uncertainty in projecting future precipitation and temperature, their impacts on future hydrologic projections, and their uncertainty contributions to total uncertainty. Climate modeling uncertainty includes the use of different GCMs and GCM initial conditions.

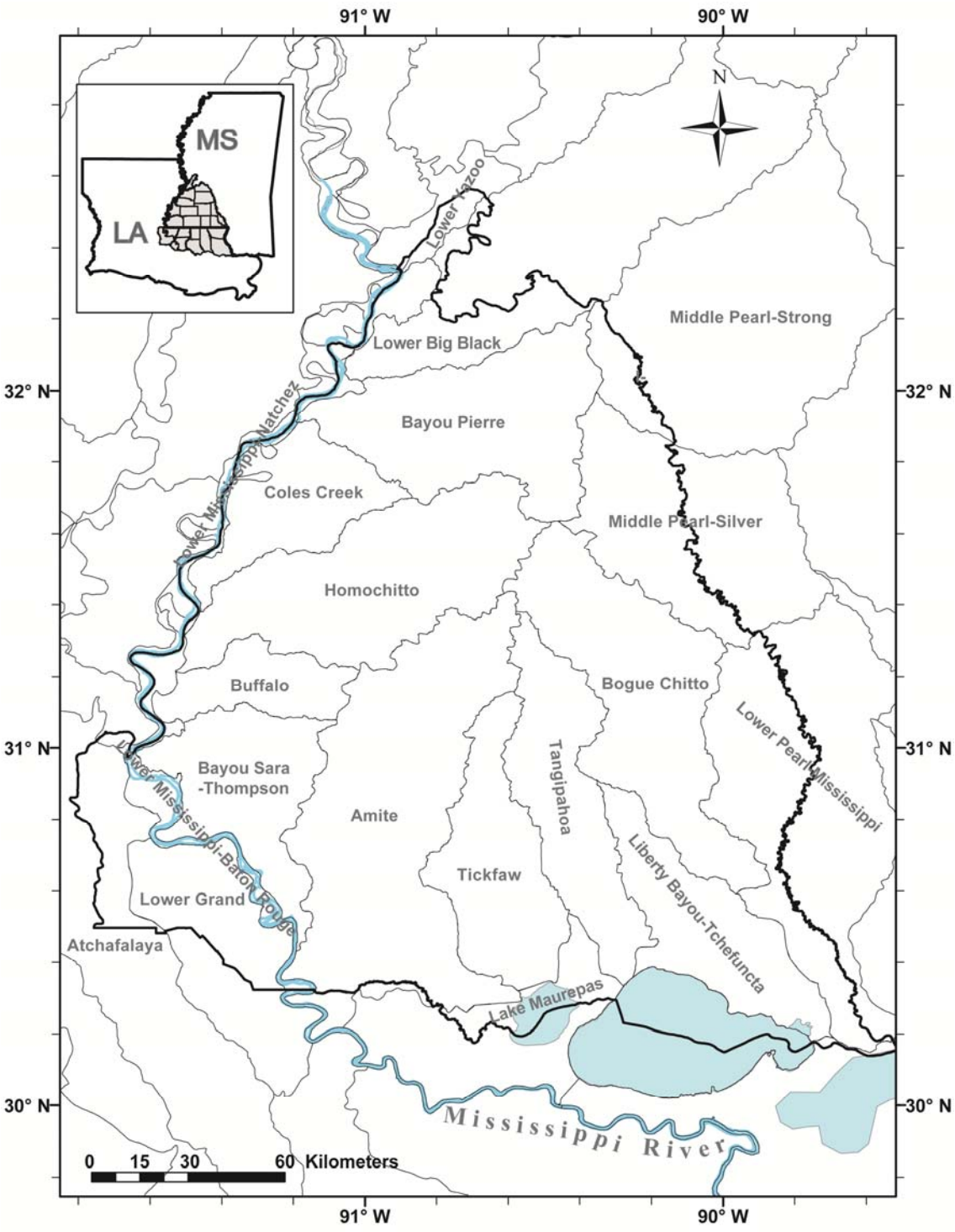

Figure 1.2: Map of the study area of the Southern Hills aquifer system and the corresponding hydrologic units (base map adapted from Atlas, Louisiana's Statewide GIS and Mississippi Geospatial Clearinghouse; data of shapefile of Southern Hills Aquifer System obtained from the U.S. EPA; data of shapefile of HUC8 obtained from the USGS)

The emission path uncertainty arises from the assumption of future GHG emissions, atmospheric GHG concentrations and other climate drivers. For the illustration purpose, this study utilizes the precipitation and temperature projections derived by 21 GCMs with different initial conditions and four representative concentration pathways (RCPs) of the Coupled Model Intercomparison Project phase 5 (CMIP5) (Maurer et. al, 2013; USBR 2013). The newest versions of climate models, emission scenarios in addition to the most recent soil data and high-resolution land use were applied in objective 3 in order to improve the framework of the research in the objective 2. Moreover, the study area is expanded to include the area of the southern Louisiana up to Gulf of Mexico. As a result, the study area covers higher number of subdivisions (2,669,533).

2. Methodology

2.1. Hydrologic Modeling

2.1.1. Hydrological Evaluation of Landfill Performance (HELP) Model

The Hydrological Evaluation of Landfill Performance model version 3.07 (HELP3) (Schroeder et al. 1994) is used to indirectly estimate regional groundwater recharge, surface runoff and evapotranspiration (ET) via a water budget approach. The HELP3 is developed by the U.S. Army Waterways Experiment Station in order assist in landfill design by conducting the water balance of landfills on a daily basis. HELP3 is a quasi-two-dimensional, physically based, deterministic, water routing model which simulates all of the important processes in the hydrologic cycle including surface runoff, evapotranspiration, vegetative growth, soil moisture storage, and vertical unsaturated drainage for each discrete layered soil column. Darcy's law models the vertical water movement for each soil layer using unsaturated hydraulic conductivity computed by Campbell hydraulic equation along with Brooks-Corey parameters. Daily infiltration is determined indirectly from a surface-water balance by assuming that infiltration is equal to the sum of rainfall and snowmelt, minus the sum of runoff, surface storage, surface evaporation and plant transpiration. Vertical percolation leaving the bottom of the deepest model layer is assumed to reach water table, and eventually become groundwater recharge (Schroeder et al. 1994). HELP3 computes runoff based on daily amount of precipitation using the U.S. Department of Agriculture (USDA) Soil Conservation Service (SCS) curve number method (USDA, SCS, 1985). Potential evapotranspiration is modeled by an energy-based Penman method (Penman, 1963). Evaporation from soil and plant transpiration is computed using the method developed by Ritchie (1972).

The HELP3 model has been used in many hydrological studies to estimate groundwater recharge, runoff and evapotranspiration (Gogolev 2002; Jyrkama and Sykes 2007; Jyrkama et al. 2002; Khire et al. 1997; Risser et al. 2005; Scibek et al. 2007; Toews and Allen 2009). The HELP model has been broadly tested by its developers (Peyton and Schroeder 1988; Schroeder et al. 1994; Schroeder and Peyton 1987) and was found to be a proper tool for this purpose. Also, Gogolev (2002) compared simulated recharge obtained from HELP model and from HELP/VS2DT model that solves the Richard's equation and found both models had similar average annual recharge. The maximum difference was 12%. Since HELP is incomparably faster and more efficient than HELP/VS2DT, Gogolev (2002) concluded that HELP model has potential to become a core of the computational technology for evaluating groundwater recharge rates. Also, Risser et al. (2005) compared HELP3 with the recession-curve displacement method (RORA) and the hydrograph separation method (PART) for estimating groundwater recharge and found that HELP3 model was in the best agreement with direct recharge measurements of an Agricultural Research Service (ARS) research site in a small watershed in the eastern United States. In addition, HELP3 has been used to simulate percolation through a composite soil cover constructed on mine tailings. And the results from the HELP modeling demonstrated to be consistent with field measurements of percolation which was observed to be 4% of precipitation (Woyshner and Yanful 1995).

HELP3 requires daily climatologic (weather) data including precipitation, mean temperature and total global solar radiation. The general climate data required by HELP3 consist of growing season, average annual wind speed, quarterly relative humidity, normal mean monthly temperatures, maximum leaf area index, evaporative zone depth and latitude. HELP3 requires the maximum leaf area index (LAI) to calculate transpiration rates for vegetation. Plant

transpiration is an important component in the water budget. The greater the leaf area index, the higher the plant transpiration. Therefore, the more leaf area index would result in less groundwater recharge, and vice versa (Eckhardt and Ulbrich 2003). In the HELP3 model, the vegetative or evaporative zone depth is the maximum depth of soil layers from which water can be removed by evapotranspiration, affecting the quantity of water available for recharge. HELP3 requires the beginning and the end of a growing season to compute seasonal variation in LAI through a general vegetative growth model. Typically, the length of the growing season in which plants grow can be presumed to be the number of successive frost free days or days with temperatures above 0 (Lavalle et al. 2009). HELP3 model requires soil texture and soil thickness for each soil layer. The soil data required by HELP3 are comprised of porosity, field capacity, wilting point, saturated hydraulic conductivity, initial moisture storage, and Soil Conservation Service (SCS) runoff curve number for antecedent moisture condition II (AMC-II).

2.1.2. Parallel Computation for High-Resolution Hydrologic Predictions

Due to a great number of subdivisions, hydrologic predictions become computationally impractical when running HELP3 sequentially in a single-core processor. This study develops a parallel procedure using Python programming language to divide large number of HELP3 model runs to multiple cores of supercomputers at Louisiana State University, QueenBee of the Louisiana Optical Network Initiative (LONI) and SuperMike-II, for parallel computation. The embarrassingly parallel method (Foster, 1995) is used because there are no communication or (dependencies) between those parallel HELP3 runs. The runtime, speedup and efficiency using a large number of cores for the study area are discussed in chapter 3 (section 3.2).

2.2. Uncertainty Analysis

2.2.1. BMA tree

Sources of uncertainty that causes climate projection uncertainty can be structured in a hierarchical order, each of which results in a number of propositions. For example, Figure 2.1 shows a hierarchical structure using precipitation and temperature projections by CMIP5 multi-model ensembles. Emission path uncertainty is at the first level, which contains four propositions: emission paths RCP2.6, RCP4.5, RCP6.0, and RCP8.5. Under each emission path, projection uncertainty caused by using different GCMs is represented at level 2. A GCM is a proposition at level 2. Given a GCM, initial condition uncertainty is considered at level 3. An initial condition is a proposition at level 3. Projection uncertainty using all considered emission paths, GCMs and their corresponding initial conditions is presented at the hierarch level. Figure 2.1 is called a BMA tree since projection means and variances for propositions at each level will be derived by the BMA. Figure 2.1 can be expanded to include different types of uncertainty sources other than aforementioned.

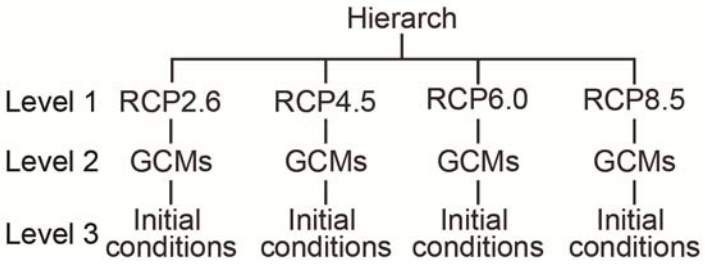

Figure 2.1: Hierarchical structure of sources of uncertainty for precipitation and temperature projections in the CMIP5 multi-model ensembles.

Each level in the BMA tree represents a targeted source of uncertainty, which stacks on the top of other sources of uncertainty below it. The base level of the BMA tree contains base models that are all climate models developed as a result of combinations of propositions at

different levels. Increasing the number of sources of uncertainty increases the number of levels of the BMA tree and the number of models. In the BMA tree, a parent model is a model at a vertex of a level with respect to child models immediately one level below. BMA is performed to average child model outputs to obtain their parent model outputs. All models above the base level are BMA models that are developed by averaging the models one level below them. The top-most BMA model is called the hierarch model, which averages models at level 1.

2.2.2. Annotations

Considering p sources of uncertainty, a base model is denoted as $M_{\underbrace{(ij...lm)}_{p}} = \mathbf{M}_p^{(m)} \in \mathbf{M}_p$ at level p. The subscript $\underbrace{(ij...lm)}_{p}$ is an index list that locates a base model hierarchically top down from the first level, to the second level and so forth to reach to base level p. For instance, the ith model at the first level of a BMA tree is denoted by $M_i = \mathbf{M}_1^{(i)} \in \mathbf{M}_1$, the jth model at level 2, a child model of $\mathbf{M}_1^{(i)}$, is denoted by $M_{ij} = \mathbf{M}_2^{(j)} \in \mathbf{M}_2$, and so forth, until the base level p is reached. On this account, models $\mathbf{M}_{p-1}$ at level $p-1$ are BMA models of their corresponding child base models $\mathbf{M}_p$ at level p, models $\mathbf{M}_{p-2}$ at level $p-2$ are BMA models of their corresponding child BMA models $\mathbf{M}_{p-1}$ at level $p-1$, and so forth, until the hierarch level is reached. The hierarch level of the hierarchy consists of one prediction model, which is termed the hierarch BMA model. The hierarch level is level zero. Eventually, the hierarch model averages predictions of all base models and thus is the same as the BMA model (Hoeting et al. 1999).

2.2.3. Hierarchical Bayesian Model Averaging (HBMA)

Let $\Pr(\Delta \mid \mathbf{D}, \mathbf{M}_n)$ be the posterior probability of predicted quantity Δ given data **D** and models $\mathbf{M}_n$ at level *n*. According to the law of total probability, the posterior probability for predicted quantity Δ given data **D** at level *n* is

$$\Pr(\Delta \mid \mathbf{D}, \mathbf{M}_n) = E_{\mathbf{M}_{n+1}}\left[\Pr(\Delta \mid \mathbf{D}, \mathbf{M}_{n+1})\right] \tag{1}$$

where $E_{\mathbf{M}_{n+1}}$ is the expectation operator, which calculates mean over models $\mathbf{M}_{n+1}$ as follows:

$$E_{\mathbf{M}_{n+1}}\left[\Pr(\Delta \mid \mathbf{D}, \mathbf{M}_{n+1})\right] = \sum_m \Pr(\Delta \mid \mathbf{D}, \mathbf{M}_{n+1}^{(m)}) \Pr(\mathbf{M}_{n+1}^{(m)} \mid \mathbf{D}, \mathbf{M}_n) \tag{2}$$

where $\Pr(\mathbf{M}_{n+1}^{(m)} \mid \mathbf{D}, \mathbf{M}_n)$ is the conditional posterior model probability for models at level $n+1$ under their parent models at level n, which is calculated by

$$\Pr(\mathbf{M}_{n+1}^{(m)} \mid \mathbf{D}, \mathbf{M}_n) = \frac{\Pr(\mathbf{M}_{n+1}^{(m)} \mid \mathbf{D})}{\Pr(\mathbf{M}_n \mid \mathbf{D})} \tag{3}$$

where $\Pr(\mathbf{M}_{n+1}^{(m)} \mid \mathbf{D})$ is the posterior model probabilities at level $n+1$ and posterior model probabilities at level n is given by

$$\Pr(\mathbf{M}_n \mid \mathbf{D}) = \sum_m \Pr(\mathbf{M}_{n+1}^{(m)} \mid \mathbf{D}) \tag{4}$$

Eq. (4) shows that posterior model probabilities at level n can be calculated as long as posterior model probabilities of base models are known.

Since Eq. (1) is a recursive equation, one can expand the right-hand side of Eq. (1) up to base models:

$$\Pr(\Delta \mid \mathbf{D}, \mathbf{M}_n) = E_{\mathbf{M}_{n+1}} E_{\mathbf{M}_{n+2}} \cdots E_{\mathbf{M}_p}\left[\Pr(\Delta \mid \mathbf{D}, \mathbf{M}_p)\right] \tag{5}$$

Using the law of total expectation and law of total variance, the expectation and variance of predicted quantity Δ at level n are

$$E(\Delta \mid \mathbf{D}, \mathbf{M}_n) = E_{\mathbf{M}_{n+1}} E_{\mathbf{M}_{n+2}} \cdots E_{\mathbf{M}_p} \left[E(\Delta \mid \mathbf{D}, \mathbf{M}_p) \right] \tag{6}$$

$$\mathrm{Var}(\Delta \mid \mathbf{D}, \mathbf{M}_n) = E_{\mathbf{M}_{n+1}} \left[\mathrm{Var}(\Delta \mid \mathbf{D}, \mathbf{M}_{n+1}) \right] + \mathrm{Var}_{\mathbf{M}_{n+1}} \left[E(\Delta \mid \mathbf{D}, \mathbf{M}_{n+1}) \right] \tag{7}$$

where $E(\Delta \mid \mathbf{D}, \mathbf{M}_p)$ is the prediction mean of Δ given data $\mathbf{D}$ and models $\mathbf{M}_p$ at level p. $\mathrm{Var}(\Delta \mid \mathbf{D}, \mathbf{M}_{n+1})$ is the prediction variance of models at level n+1. $\mathrm{Var}_{\mathbf{M}_{n+1}}[\bullet]$ is the variance operator, which calculates the between-model variance using models at level n+1. The first term at the right-hand side of Eq. (7) is the within-model variance of prediction Δ using models of level n+1. The second term is the between-model variance of prediction that accounts for the spreading of mean predicted Δ by different models at level n+1. Since Eq. (7) is a recursive equation, the within-model variance is obtained by

$$E_{\mathbf{M}_{n+1}} \left[\mathrm{Var}(\Delta \mid \mathbf{D}, \mathbf{M}_{n+1}) \right] = E_{\mathbf{M}_{n+1}} \left[E_{\mathbf{M}_{n+2}} \left[\mathrm{Var}(\Delta \mid \mathbf{D}, \mathbf{M}_{n+1}) \right] + \mathrm{Var}_{\mathbf{M}_{n+2}} \left[E(\Delta \mid \mathbf{D}, \mathbf{M}_{n+2}) \right] \right] \tag{8}$$

The between-model variance is

$$\mathrm{Var}_{\mathbf{M}_{n+1}} \left[E(\Delta \mid \mathbf{D}, \mathbf{M}_{n+1}) \right] = E_{\mathbf{M}_{n+1}} \left[\left[E(\Delta \mid \mathbf{D}, \mathbf{M}_{n+1}) - E(\Delta \mid \mathbf{D}, \mathbf{M}_n)^2 \right] \right] \tag{9}$$

2.2.4. Prediction Mean and Variance at Hierarch Level

The prediction mean of Δ at the hierarch level can be obtained by averaging the prediction means of models at level 1 or using Eq. (2) recursively from base level to level 1:

$$E(\Delta \mid \mathbf{D}) = E_{\mathbf{M}_1} \left[E(\Delta \mid \mathbf{D}, \mathbf{M}_1) \right] = E_{\mathbf{M}_1} E_{\mathbf{M}_2} \cdots E_{\mathbf{M}_p} \left[E(\Delta \mid \mathbf{D}, \mathbf{M}_p) \right] \tag{10}$$

The total prediction variance of Δ at the hierarch level is

$$\mathrm{Var}(\Delta \mid \mathbf{D}) = E_{\mathbf{M}_1} \left[\mathrm{Var}(\Delta \mid \mathbf{D}, \mathbf{M}_1) \right] + \mathrm{Var}_{\mathbf{M}_1} \left[E(\Delta \mid \mathbf{D}, \mathbf{M}_1) \right] \tag{11}$$

Contribution of individual sources of uncertainty to the total uncertainty can be evaluated by using Eq. (11). Using Figure 2.1 as an example, the total variance of climate projection can be expanded for three levels:

$$\begin{aligned}\mathrm{Var}(\Delta \mid \mathbf{D}) = {} & \mathrm{Var}_{\mathbf{M}_1}\left[E\left(\Delta \mid \mathbf{D}, \mathbf{M}_1\right)\right] + E_{\mathbf{M}_1}\mathrm{Var}_{\mathbf{M}_2}\left[E\left(\Delta \mid \mathbf{D}, \mathbf{M}_2\right)\right] \\ & + E_{\mathbf{M}_1}E_{\mathbf{M}_2}\mathrm{Var}_{\mathbf{M}_3}\left[E\left(\Delta \mid \mathbf{D}, \mathbf{M}_3\right)\right] + E_{\mathbf{M}_1}E_{\mathbf{M}_2}E_{\mathbf{M}_3}\left[\mathrm{Var}\left(\Delta \mid \mathbf{D}, \mathbf{M}_3\right)\right],\end{aligned} \tag{12}$$

The first term at the right-hand side of Eq. (12) is the projection variance due to emission path uncertainty. The second term is the projection variance caused by using different GCMs. The third term is the projection variance due to using different GCM initial conditions. The fourth term is the projection variance caused by parameter uncertainty in individual GCMs. Contributions of these sources of uncertainty is defined as the proportions of their corresponding variance terms to the total variance. It is emphasized that the HBMA is able to distinguish uncertainty contributions of individual sources of uncertainty while BMA (Hoeting et al., 1999) cannot.

3. High-Resolution Hydrologic Prediction of Large-Scale Humid Regions

The goal of the chapter is to develop a water budget framework using HELP3 coupled with a geographic information system (GIS) to estimate groundwater recharge, surface runoff and ET in large-scale humid regions. The framework is applied to the area of the Southern Hills aquifer system, which is divided into 286,355 subdivisions. Each subdivision has homogeneous model parameters for HELP3.

Previous hydrologic estimations using HELP3 has been applied to relatively small scale study areas. Jyrkama and Sykes (2007) adopted HELP3 and GIS for groundwater recharge, runoff and ET estimation of the Grand River watershed, south-western Ontario, Canada. Their study area covers approximately 7,000 km^2, which was divided into more than 47,000 unique combinations of HELP3 input data. Risser et al. (2005) used HELP3 and GIS to estimate recharge for a small watershed 197 km^2, which was divided into 577 homogenous units based on unique soil type, slope, vegetation, and precipitation. Moreover, recharge has been estimated using WetSpass (a spatially distributed water balance model) and GIS (Batelaan and De Smedt 2007; Tilahun and Merkel 2009; Gebreyohannes et al. 2013). The largest study area was 1,912 km^2 with a grid resolution of 50×50 m. To the best of our knowledge, HELP3 has not been applied to such a large scale problem in terms of the size of area and the number of subdivisions.

3.1. Study Area

The area of the Southern Hills aquifer system shown in Figure 1.2 is located in southwestern Mississippi and southeastern Louisiana and covers 32,678 km^2. It lies between latitude from 30° 9' 0" N to 32° 33' 36" N and longitude from 89° 33' 36" W to 91° 48' 36" W. It consists of 14 counties in Mississippi and 10 parishes in Louisiana. The study area covers 235 climate zones with a grid resolution of 12×12 km. Additionally, the study area covers 24 8-digit

hydrologic units (HUC8), of which 4 HUC8 are located in water areas and were not considered in the recharge simulation. Each HUC8 delineates a subbasin with average size of 588 square kilometer in a hierarchical system of hydrologic units defined by United States Geological Survey (USGS). The area of the Southern Hills aquifer system covers 25 different land use/land cover classes. They are cropland and pasture (33.1 %), mixed forest land (29.5 %), evergreen forest land (15.9 %), deciduous forest land (7.4 %), forested wetland (5.0 %), and residential (2.5 %) land use/land cover. Other types of land use/land cover (e.g., industrial) cover less than 2.0 % of the study area.

A digital elevation model (DEM) with a resolution of 10 m shows that the area has an average slope of 11 % with an elevation varying from -2 m to 172 m above mean sea level. The thickness of the unsaturated zone ranges from 2 m to 115 m with an average of 18.2 m. The lithology is comprised of a series of sandy gravel to clayey formations that generally dip south towards the Gulf of Mexico. The study area is covered by silty loam (56.8 %), sandy loam (10.3 %), fine sandy loam (10.0 %), sand (5.8 %), clay (5.0 %) and silty clay loam (3.7 %). Other types of the U.S. Department of Agriculture (USDA) soil texture class (e.g., coarse sand) cover less than 1.0 % of the area of the Southern Hills aquifers system. The formations range in age from early Miocene at the north and northwest to Pleistocene and Holocene extending from northeast to south of the aquifer system (Dicken et al. 2005). The Miocene deposits consist of Catahoula, Pascagoula, and Hattiesburg formations, the Pleistocene deposits include Citronelle and Terraces, and the Holocene deposits account for Mississippi river and other major stream alluvium (Buono 1983). Groundwater recharge through the outcrops in southwestern Mississippi provides an important freshwater source to the deep aquifers in southeastern Louisiana. The U.S. Environmental Protection Agency (USEPA) designates the Southern Hills aquifer system as one

of the sole source aquifers (SSAs), which is the only source of potable water consumed in the area overlying the aquifers and has no substitute drinking water source(s). The SSA protection program secures the Southern Hills aquifer system in order to ensure the strictest protection of the local groundwater resources from contamination, under the section 1424 of Public Law 93-523, the Safe Drinking Water Act of 1974 (U.S. Congress, 1996).

3.2. Hydrologic Estimation

To estimate recharge for a subdivision, HELP3 solves the water budget equation and calculates the drainage out of the last soil layer as deep percolation. This study considers that some part of deep percolation eventually can seep back into surface water bodies such as stream channels as base flow (Fitts 2002). As a result, recharge is estimated by subtracting the baseflow from deep percolation.

The first step was to compute baseflow for each subdivision in the hydrologic units shown in Figure 1.2. We assumed that baseflow is proportional to deep percolation for each subdivision. Therefore, the baseflow is calculated by

$$BF_{i,u} = BFI_u \times Q_u^{\text{WaterWatch}} \times \left(\frac{R_{i,u}^{\text{HELP3}}}{R_u^{\text{HELP3}}} \right) \tag{13}$$

where $BF_{i,u}$ is the baseflow for subdivision *i* in hydrologic unit *u*, BFI_u is the baseflow index for hydrologic unit *u* obtained from Wolock (2003), $Q_u^{\text{WaterWatch}}$ is the computed runoff from the USGS WaterWatch database for hydrologic unit *u*, $R_{i,u}^{\text{HELP3}}$ is the deep percolation obtained from HELP3 for subdivision *i* in hydrologic unit *u*, and R_u^{HELP3} is the area-averaged deep percolation from HELP3 for hydrologic unit *u*, which is

$$R_u^{\text{HELP3}} = \frac{\sum_i R_{i,u}^{\text{HELP3}} \times A_{i,u}}{\sum_i A_{i,u}} \tag{14}$$

where $A_{i,u}$ is the area of subdivision *i* in hydrologic unit *u*.

To calculate groundwater recharge, the deep percolation is subtracted by the baseflow for each subdivision:

$$\bar{R}_{i,u}^{\text{HELP3}}(t) = R_{i,u}^{\text{HELP3}}(t) - BF_{i,u}\left(t + \tau_{i,u}^{\text{delay}}\right) \tag{15}$$

where $\bar{R}_{i,u}^{\text{HELP3}}$ is the recharge at time *t* for subdivision *i* in hydrologic unit *u* and $\tau_{i,u}^{\text{delay}}$ is the time delay between recharge and baseflow for subdivision *i* in hydrologic unit *u*. The time delay is determined by maximizing the cross correlation between monthly deep percolation time series $R_{i,u}^{\text{HELP3}}(t)$ and the monthly baseflow time series $BF_{i,u}(t)$ (Zhang and Abdulla 2005) as follows

$$\tau_{i,u}^{\text{delay}} = \arg\max_{\tau} \int_t R_{i,u}^{\text{HELP3}}(t) \times BF_{i,u}(t+\tau)\, dt \tag{16}$$

where τ is the delay time variable (month).

3.2.1. Parallel Computation for High-Resolution Hydrologic Estimation

Among the 286,355 subdivisions, 23,475 subdivisions in water areas are excluded from the hydrologic analysis. Therefore, 262,880 HELP3 model runs are needed for hydrologic estimation for the area of the Southern Hills aquifer system.

The aforementioned parallel procedure in chapter 2.1.2 is used to divide the required HELP3 model runs to multiple cores of a supercomputer, QueenBee of the Louisiana Optical Network Initiative (LONI), for simultaneous calculation. QueenBee has 680 compute nodes. Each node contains 8GB RAM and two Quad Core Xeon 64-bit processors operating at a core frequency of 2.33 GHz running the Red Hat Enterprise Linux 4 operating system. The

embarrassingly parallel method (Foster, 1995) is used because there are no communication or (dependencies) between those parallel HELP3 runs. The total run time of 262,880 subdivisions from 1950-2010 sequentially on a single processor is 2900 minutes. The parallel speedup and efficiency is used to evaluate parallel performance. The parallel speedup is the ratio of the runtime for one core to the runtime using a number of cores. The efficiency is the speedup over the total number of cores. Table 3.1 shows parallel speedup and efficiency using various numbers of cores. The speedup increases from 7.99 using 8 cores to 483.33 using 1024 cores. The efficiency decreases while using a large number of cores due to more distribution time to cores. In summary, the embarrassingly parallel method is able to perform HELP3 model calibration for a very large number of subdivisions in much less computation time.

Table 3.1: Runtimes (minutes), speedup and efficiency for embarrassingly parallel method.

Number of Cores	Runtimes (minutes)	Speedup	Efficiency
1	2900	1.00	1.00
8	363	7.99	1.00
16	189	15.32	0.96
32	97	29.82	0.93
64	58	50.00	0.78
128	37	78.38	0.61
256	26	111.54	0.44
512	14	207.14	0.40
1024	6	483.33	0.47

3.2.2. HELP3 Model Input Data

3.2.2.1. Weather Data

Historical daily precipitation and temperature data with a resolution of 12 km from 1950 to 2009 were obtained from Maurer et al. (2002) and Maurer (2013). The daily temperature and precipitation observations are obtained from the National Oceanic and Atmospheric Administration (NOAA) Cooperative Observer (COOP) stations and gridded to 12 km spatial

resolution. Average annual wind speed and average quarterly relative humidity were obtained from Southern Regional Climate Center (Robbins 2013). The downscaled solar radiation data was generated synthetically using the weather generator (WGEN) model of Richardson and Wright (1984). The generated values of solar radiation are computed as a function of the daily mean precipitation for each climate zone using the same statistical characteristics of the historical solar radiation at Baton Rouge (Louisiana) and Jackson (Mississippi) from the HELP3 model. Then, the statistical characteristics were adjusted for each climate zone's latitude.

3.2.2.2. Soil Data

HELP3 model requires soil texture and soil thickness for each soil layer. The detailed surficial soil symbols is obtained from the STATSGO2 soil database of Natural Resources Conservation Service (NRCS 2013), and then used the reports of soil surveys of each county/parish of the study area to convert soil symbols into USDA soil texture classes. A total of 514 unique surface soil symbols were identified in the area of the Southern Hills aquifer system and then converted into the USDA soil texture classes using the reports of soil surveys of each county/parish of the study area. The corresponding total porosity, field capacity, wilting point and saturated hydraulic conductivity for all soil texture classes were then determined using the table of default soil characteristics in the HELP3 user manual. The thickness for the surficial soil layer was considered up to 1.5 m in depth. For the soil texture and thickness beneath the surficial soil layer, 3,431 well logs and drillers' logs in the study area were compiled and analyzed to determine lithostratigraphy up to the top-most major sands. Lithology of the closest well logs is assigned to the corresponding subdivisions.

3.2.2.3. Land Use and Land Cover Data

Land use and land cover data was obtained from the USGS enhanced historical land use and land cover datasets. The USGS provides a vector-based 1:250000 land use/land cover map which showed the distribution of 25 different land use/land cover classes within the area of the Southern Hills aquifer system (Price et al. 2006).

3.2.2.4. Input Data for Runoff Calculation

3.2.2.4.1. Curve Number

The Soil Conservation Service (SCS) curve-number method (U.S. Department of Agriculture, 1985) was used in the HELP3 to compute surface runoff. To determine curve number, the soil surface map and land use/land cover map were used to derive a map of runoff-curve number (CN) by the SCS Technical Release 55 (NRCS 1986). Therefore, runoff curve number for 262,880 subdivisions in the study area was determined.

3.2.2.4.2. Topographic Slope and Slope Length

Topographic slope and slope length is needed to adjust the curve number for each subdivision. We derived DEM in 10-m resolution based on the DEM data from Mississippi Geospatial Clearinghouse and Atlas: Louisiana's Statewide GIS. Then, ArcGIS was used to calculate topographic slope and slope length for each subdivision in the study area.

3.2.2.5. Vegetation Data

3.2.2.5.1. Leaf Area Index

The yearly averaged LAI for each subdivision was calculated from the LAI dataset generated by reprocessing the MODIS (Yuan et al., 2011). The leaf area index of the study area ranges from 1 to 6 with the mean of 3.4. LAI has 1 km resolution, which is much higher than the

land use map. In other words, the same land use type may have different LAI values. The averaged standard deviation of the LAI for land use is 1.08, which shows fair consistency between the LAI and the land use.

3.2.2.5.2. Evaporative Zone Depth

The maximum rooting depth of vegetation for each subdivision was estimated based on its land use, soil and vegetation types according to the study of the maximum rooting depth on a global scale (Canadell et al. 1996). The minimum and maximum evaporative zone depth is 10.5 cm and 730.5 cm, respectively. The mean evaporative zone depth is 380.1 cm. The maximum rooting depths of vegetation was used as the evaporative zone depth in this study.

3.2.2.5.3. Growing Season

In this study, the growing season begins in earliest mid-January and ends in mid-December. The same growing season was assumed for all subdivisions in the study area.

3.2.3. HELP3 Calibration and Verification

3.2.3.1. Adjust Curve Number

The computed runoffs of individual hydrologic units from the USGS WaterWatch database (Brakebill et al., 2011) were used to calibrate the HELP3 model by adjusting runoff curve number for each subdivision. Derived from the comprehensive National Water Information System (NWIS) gauge observation, WaterWatch runoff is the assimilated time series of flow per unit of area calculated for each conterminous HUC8 subbasin. For each HUC8 subbasin, multiple NWIS gauge stations located within or downstream of the HUC8 were used to estimate the runoff generated locally at each HUC8 (Oubeidillah et al., 2014). Based on the regression equation (34) in HELP Engineering Documentation for Version 3 (Schroeder et al. 1994), we

propose an equation to adjust user-specified AMC-II curve number for different topographic slope and slope length conditions for each subdivision as follows

$$CN_{II} = 100 - \left(100 - CN_{II_0}\right)\left(\frac{L^{*2}}{S^{*}}\right)^{\left[CN_{II_0}\right]^{m}} \tag{17}$$

where CN_{II_0} is the AMC-II curve number computed for default soils and vegetation placed at mild slopes, L^{*} is the standardized dimensionless slope length (L/500), S^{*} is the standardized dimensionless slope (S/0.04), and m is the parameter for each hydrologic unit ($m = -0.81$ in HELP3). L is the slope length of each subdivision (ft) and S is the slope of each subdivision (ft/ft).

The optimal parameter m for each hydrologic unit is obtained by minimizing the sum of squared errors of the HELP3 calculated to USGS computed direct runoffs:

$$\min_{-1<m<0} \sum_{t}\left[\bar{Q}_u^{\text{HELP3}}(t) - \bar{Q}_u^{\text{WaterWatch}}(t)\right]^2 \tag{18}$$

where $\bar{Q}_u^{\text{HELP3}}(t)$ is the calculated direct runoff at time t for hydrologic unit u from the HELP3 model and $\bar{Q}_u^{\text{WaterWatch}}(t)$ is the computed direct runoff at time t for hydrologic unit u from the USGS WaterWatch database. Yearly USGS computed runoffs from 1950 to 2000 were used for model calibration. $\bar{Q}_u^{\text{HELP3}}(t)$ is calculated by the area-averaged HELP3 direct runoffs

$$\bar{Q}_u^{\text{HELP3}} = \frac{\sum_i \bar{Q}_{i,u}^{\text{HELP3}} \times A_{i,u}}{\sum_i A_{i,u}} \tag{19}$$

where $\bar{Q}_{i,u}^{\text{HELP3}}$ is the HELP3 direct runoff at subdivision i in hydrologic unit u. $\bar{Q}_u^{\text{WaterWatch}}$ is calculated by

$$\bar{Q}_u^{\text{WaterWatch}} = \left(1 - BFI_u\right) \times Q_u^{\text{WaterWatch}} \tag{20}$$

Since there is only one unknown parameter in the objective function (18) for each hydrologic unit, the minimization problem solved by the lattice search (Birkhoff 1967) with 10 lattices in each iteration of refinement is efficient. The iteration process continued until the error cannot be reduced. We calibrated 262,880 HELP3 models for 20 hydrologic units simultaneously using the aforementioned parallel computing technique in the LONI. Table 3.2 shows the optimized curve number parameter *m* ranging from -0.40 to -0.18 and the root mean square error (RMSE) ranging from 85.52 to 122.98 mm for individual hydrologic units.

Table 3.2: Estimated curve number parameter m for each hydrologic unit in the Southern Hills aquifer system.

Hydrologic Unit Name	Hydrologic Unit Code (HUC)	CN Parameter *m*	Root Mean Square Error (mm)
Amite	8070202	-0.29	85.52
Atchafalaya	8080101	-0.22	121.44
Bayou Pierre	8060203	-0.31	93.35
Bayou Sara-Thompson	8070201	-0.40	122.98
Bogue Chitto	3180005	-0.29	88.24
Buffalo	8060206	-0.28	118.87
Coles Creek	8060204	-0.39	97.26
Homochitto	8060205	-0.33	90.21
Lake Maurepas	8070204	-0.33	109.79
Liberty Bayou-Tchefuncta	8090201	-0.25	109.29
Lower Big Black	8060202	-0.29	119.84
Lower Grand	8070300	-0.18	108.72
Lower Mississippi-Baton Rouge	8070100	-0.22	104.51
Lower Mississippi-Natchez	8060100	-0.30	96.3
Lower Pearl-Mississippi	3180004	-0.35	121.43
Lower Yazoo	8030208	-0.32	119.81
Middle Pearl-Silver	3180003	-0.31	94.37
Middle Pearl-Strong	3180002	-0.30	103.2
Tangipahoa	8070205	-0.27	87.73
Tickfaw	8070203	-0.29	88.54

Considering all 20 hydrologic units, the RMSE is 111.25 mm, which is much smaller than the range of the WaterWatch yearly runoff data. As shown in Figure 3.1, the HELP3 calculated yearly runoffs show good agreement with the USGS WaterWatch yearly runoffs. 71.1% of the scatter points are inside one RMSE interval.

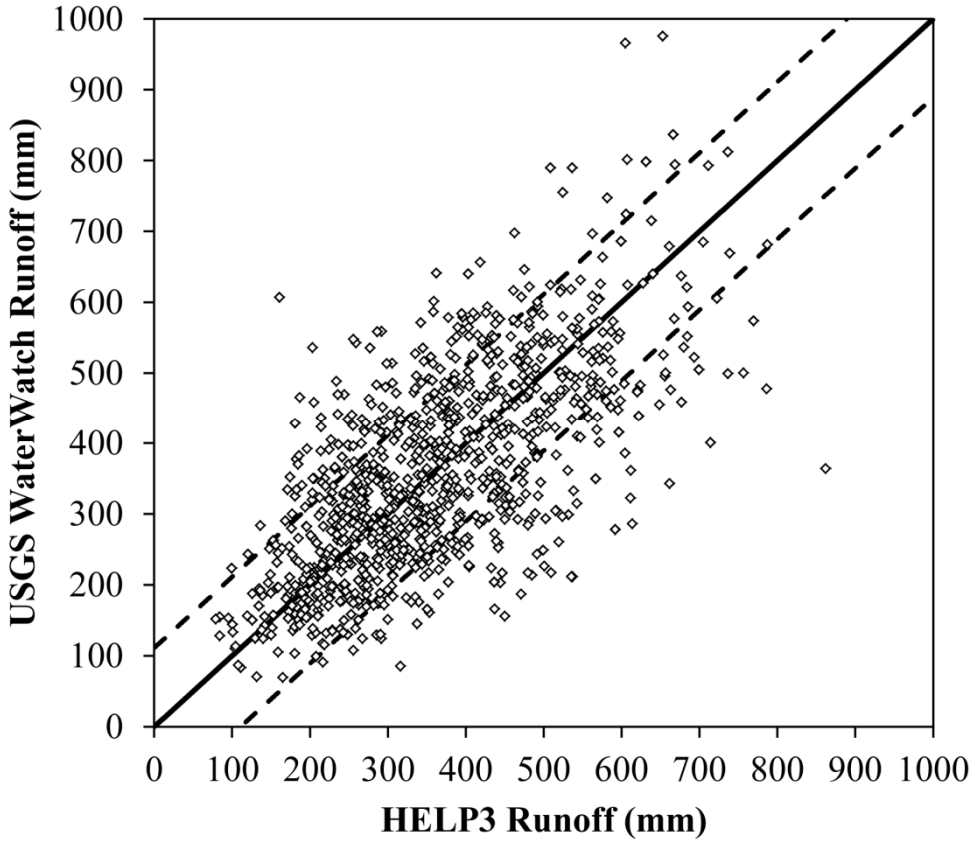

Figure 3.1: Comparison of HELP3 calculated yearly direct runoff with the USGS WaterWatch yearly direct runoff from 1950 to 2000. Dash lines show one RMSE=111.25 mm interval to the 45 degree line.

3.2.3.2. Evapotranspiration (ET) Verification

To verify the calibrated HELP3 models, the HELP3 computed evapotranspiration (ET) was compared with the estimated evapotranspiration obtained from MOD16 evapotranspiration dataset based on the MODIS remote sensing data (Mu et al. 2007; Mu et al. 2011). The MOD16 provides evapotranspiration data to 1,166 5-km square cells in the study area. 167 cells that have evapotranspiration higher than precipitation in MOD16 ET dataset were excluded from the ET comparison. The RMSE of the HELP3 yearly estimated ET to the MOD16 yearly estimated ET for the 999 cells from 2000 to 2010 is 93.52 mm, which is much smaller than the range of the

MOD16 ET estimates. As shown in Figure 3.2, HELP3 estimated ET reveals good agreement with MOD16 ET from 2000 to 2010. 80.2% of the scatter points are inside one RMSE interval.

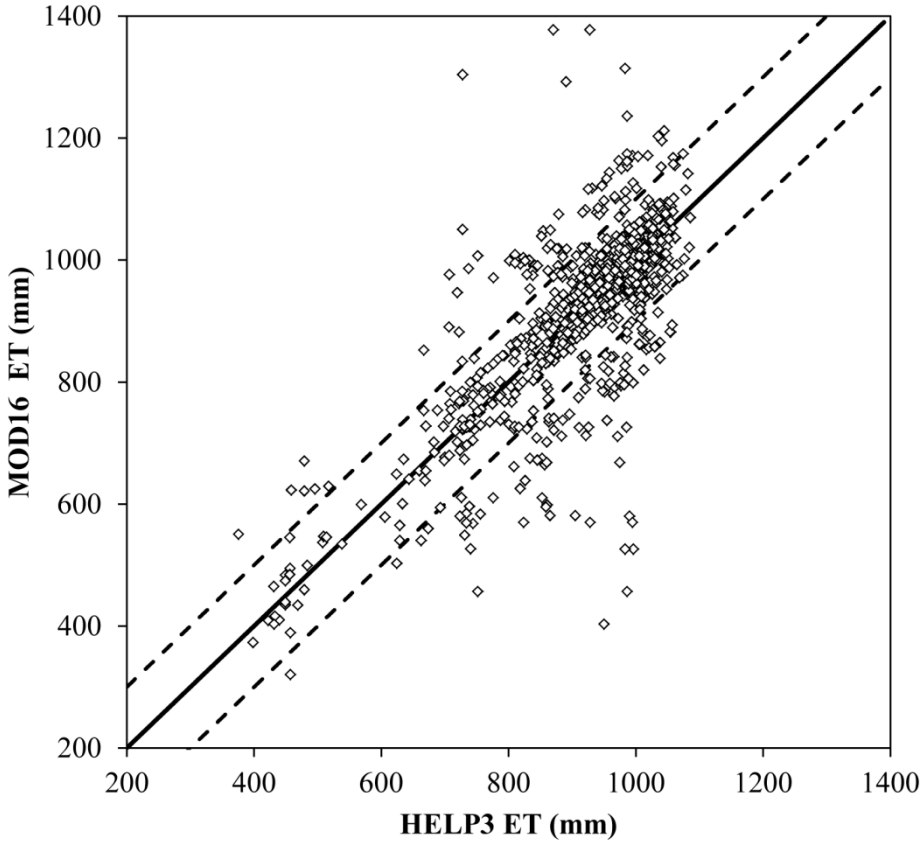

Figure 3.2: Comparison of HELP3 yearly calculated evapotranspiration with MOD16 ET from 2000 to 2010. Dash lines show one RMSE=93.52 mm interval to the 45 degree line.

Direct calibration of the HELP3 model using recharge data was not possible because field recharge data were not available in the study area. However, the accuracy of recharge estimation was improved by having better estimation on other water budget components such as runoff and evapotranspiration. The GIS-based water budget framework using HELP3 and GIS is shown in Figure 3.3 for estimation of high-resolution temporal and spatial groundwater recharge, surface runoff and evapotranspiration for the Southern Hills aquifer system.

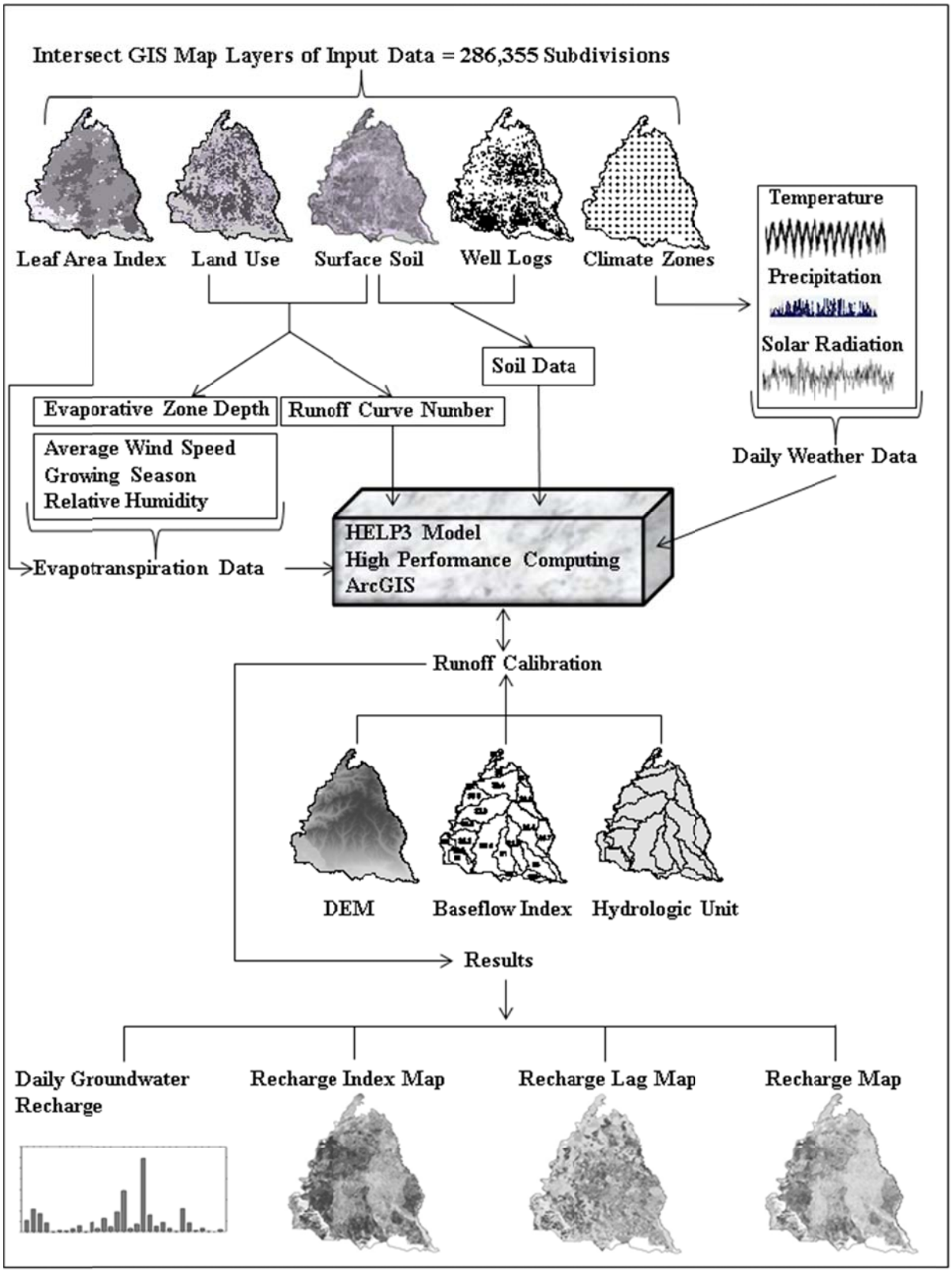

Figure 3.3: The GIS-based water budget framework for groundwater recharge, runoff and ET estimation.

286,355 subdivisions were resulted from the intersection of maps of weather data, soil data, land use/land cover data, and vegetation data. GIS is used to prepare, organize, and manipulate the input data for the HELP3 model and to visualize and analyze the model results. After the completion of model calibration, the daily groundwater recharge, the recharge time lag map, the recharge index map, and the spatial recharge map can be derived.

3.3. Temporal Analysis

After calibrating the HELP3 models, evapotranspiration, direct runoff, recharge, and water change in soil storage for each subdivision were estimated on a daily basis from 1950 to 2010. Daily values were then aggregated to provide monthly and annual estimates. Figure 3.4 shows the correlation between the annual recharge and the annual precipitation for the entire study area using area average on all subdivisions. The correlation coefficient is 0.76. The minimum and maximum annual precipitation is 1061.5 mm and 2068.6 mm, respectively. The mean annual precipitation is 1522.1 mm. The minimum and maximum annual recharge is 21.6 mm and 85.1 mm, respectively. The mean annual recharge is 45.3 mm. The ratio of annual recharge to annual precipitation ranges from 1.6% to 5.1%, with the mean 2.9%. Figure 3.5 shows the mean monthly recharge from 1950 to 2010. October has the lowest monthly recharge rate 3.1 mm while March has the highest recharge rate 4.55 mm.

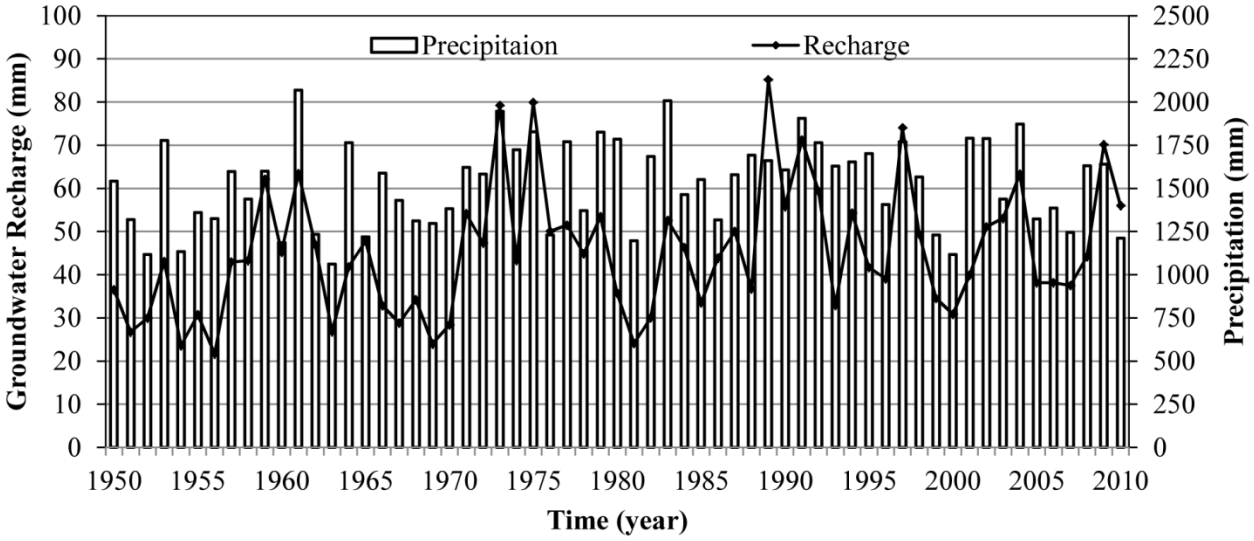

Figure 3.4: Annual groundwater recharge and annual precipitation for the Southern Hills aquifer system from 1950 to 2010.

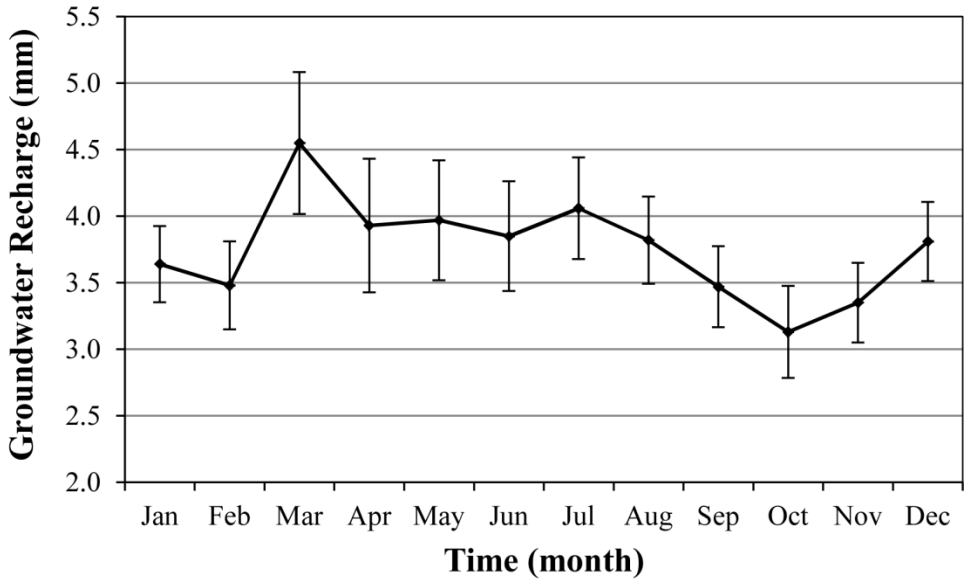

Figure 3.5: Mean monthly groundwater recharge for the Southern Hills aquifer system. The bars show the margin of error at 95% confidence level.

3.4. Spatial Analysis

3.4.1. Recharge Time Lag and Index

To best understand the relationship between precipitation and estimated groundwater recharge for each subdivision, a recharge time lag map and a recharge index map for the area of the Southern Hills aquifer system were created. The recharge time lag is to understand the travel time of infiltrated precipitation reaching the last soil layer. The recharge time lag τ_i^{lag} for each subdivision i is determined by maximizing the cross correlation between the monthly precipitation time series $P_i(t)$ and the monthly recharge time series $\overline{R}_{i,u}^{\text{HELP3}}(t)$ as follows

$$\tau_i^{\text{lag}} = \arg\max_{\tau} \int_t P_i(t) \times \overline{R}_{i,u}^{\text{HELP3}}(t+\tau)\, dt \tag{21}$$

where τ is the lag time variable (month).

Figure 3.6 shows the map of recharge time lag, where 36% of the study area has time lag less than one month. Half of the study area has time lag less than 4 months. 19% of the study area has a time lag higher than 10 months. Figure 3.7 shows that the magnitude of recharge time lag directly relates to hydraulic conductivity of the soil layers. The time lag decreases with increasing equivalent vertical hydraulic conductivity of soil layers.

Ratios of the time-lagged recharge to precipitation for a 12-month interval were calculated for each subdivision. Then, the recharge index (RI) is defined as the mean ratio, which represents the annual mean percentage of precipitation that becomes recharge to aquifers. Figure 3.8 shows the RI map for the area of the Southern Hills aquifer system. The west of the area has high RI, which includes the hydrologic units Coles Creek, Homochitto, Buffalo Bayou, and Sara-Thompson. These hydrologic units received higher precipitation and generated less runoff and

baseflow, which resulted in higher recharge to the aquifer system. Low RI is estimated in the north and east of the study area.

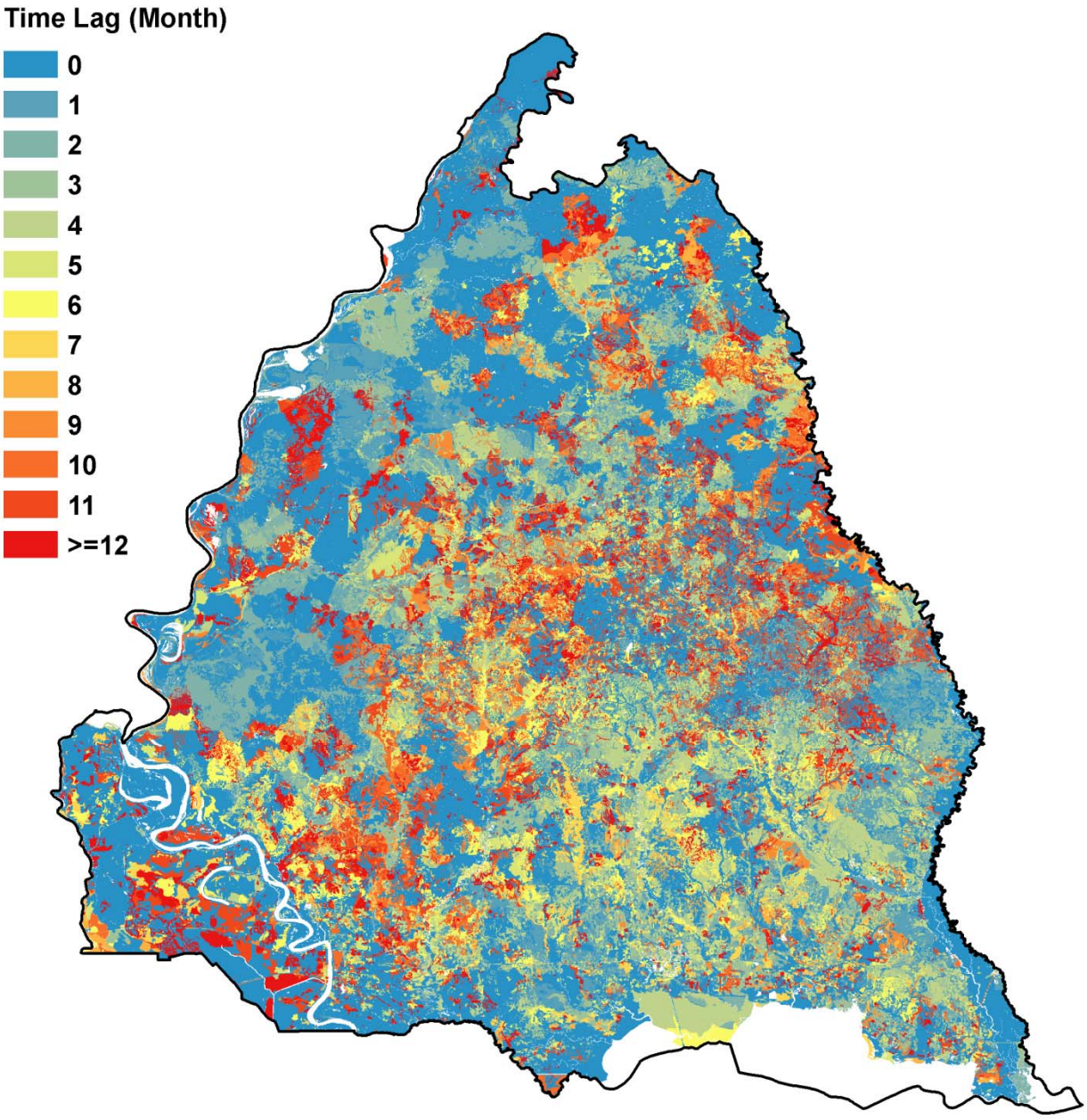

Figure 3.6: Map of the recharge time lag (months) for the Southern Hills aquifer system.

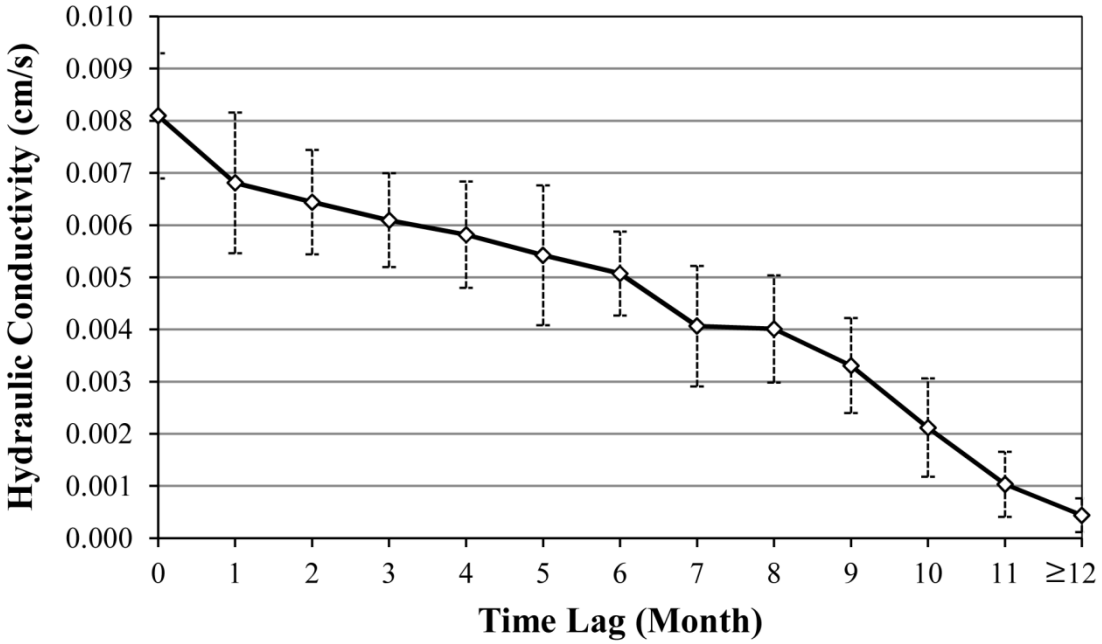

Figure 3.7: Time lag (months) versus equivalent vertical hydraulic conductivity (cm/s) for each subdivision. The error bars show one standard deviation around the mean.

3.4.2. Groundwater Recharge Rate

The map of mean annual recharge rate for the area of the Southern Hills aquifer system is shown in Figure 3.9. Comparing to the recharge index map (Figure 3.8), areas of high recharge rate have high recharge index, and vice versa. The recharge map shows high recharge rate at outcrops of Miocene deposits and low recharge rate at outcrops of Pleistocene deposits. This result is opposite to the studies of Buono (1983) and Hanson and Boniol (1985), which defined potential recharge zones through investigating the surficial geologic formations of the Southern Hills aquifer system. They characterized Miocene outcrop as poor recharge potential zones due to low permeability of surface materials and Pleistocene deposits as high recharge zones because of high permeability of Citronelle formation. The discrepancy highlights the fact that precipitation, temperature, solar radiation, land use, land cover, and underlying soil types can influence recharge significantly in addition to the surficial geologic formations.

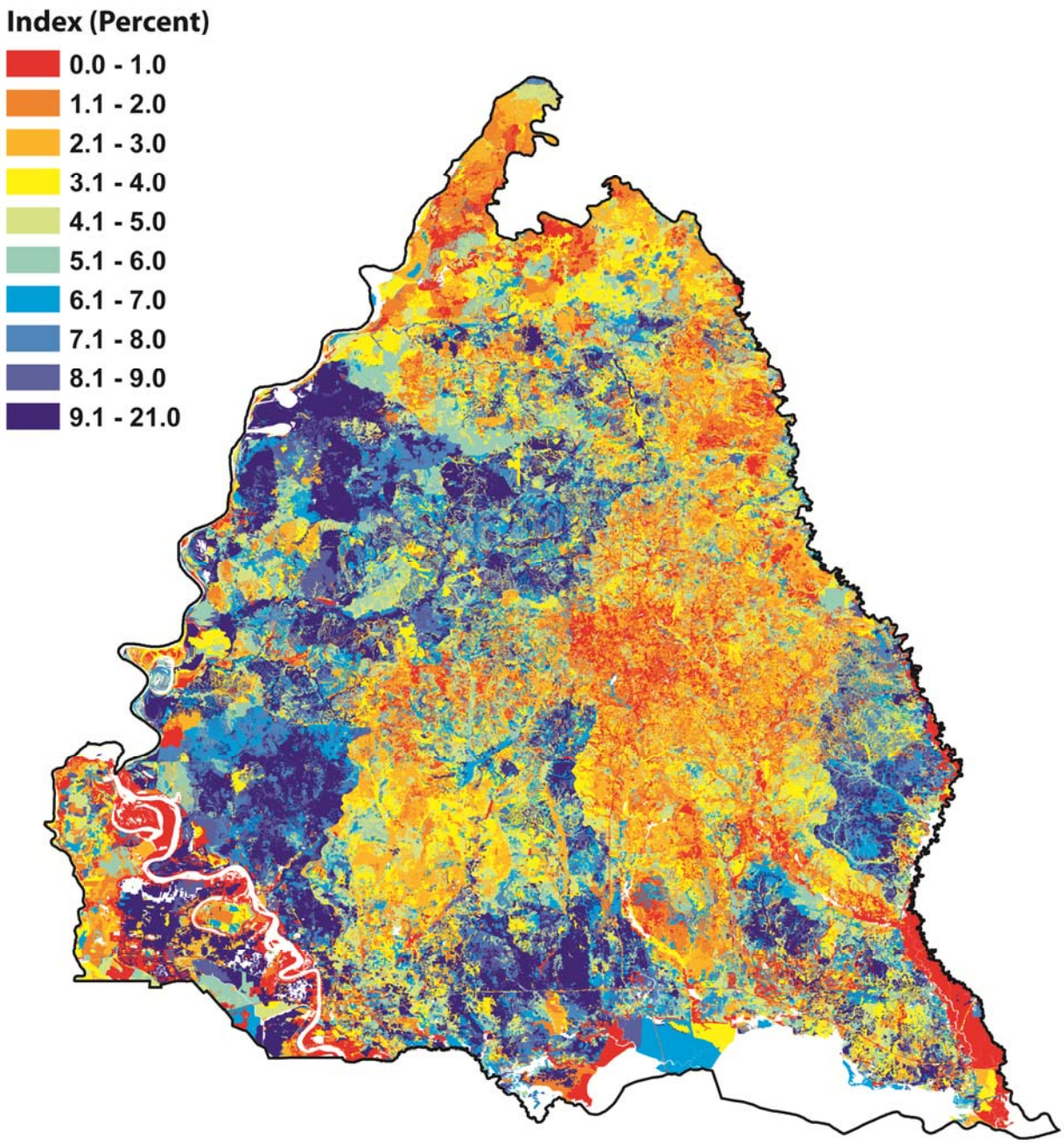

Figure 3.8: Map of the recharge index (%) for the Southern Hills aquifer system.

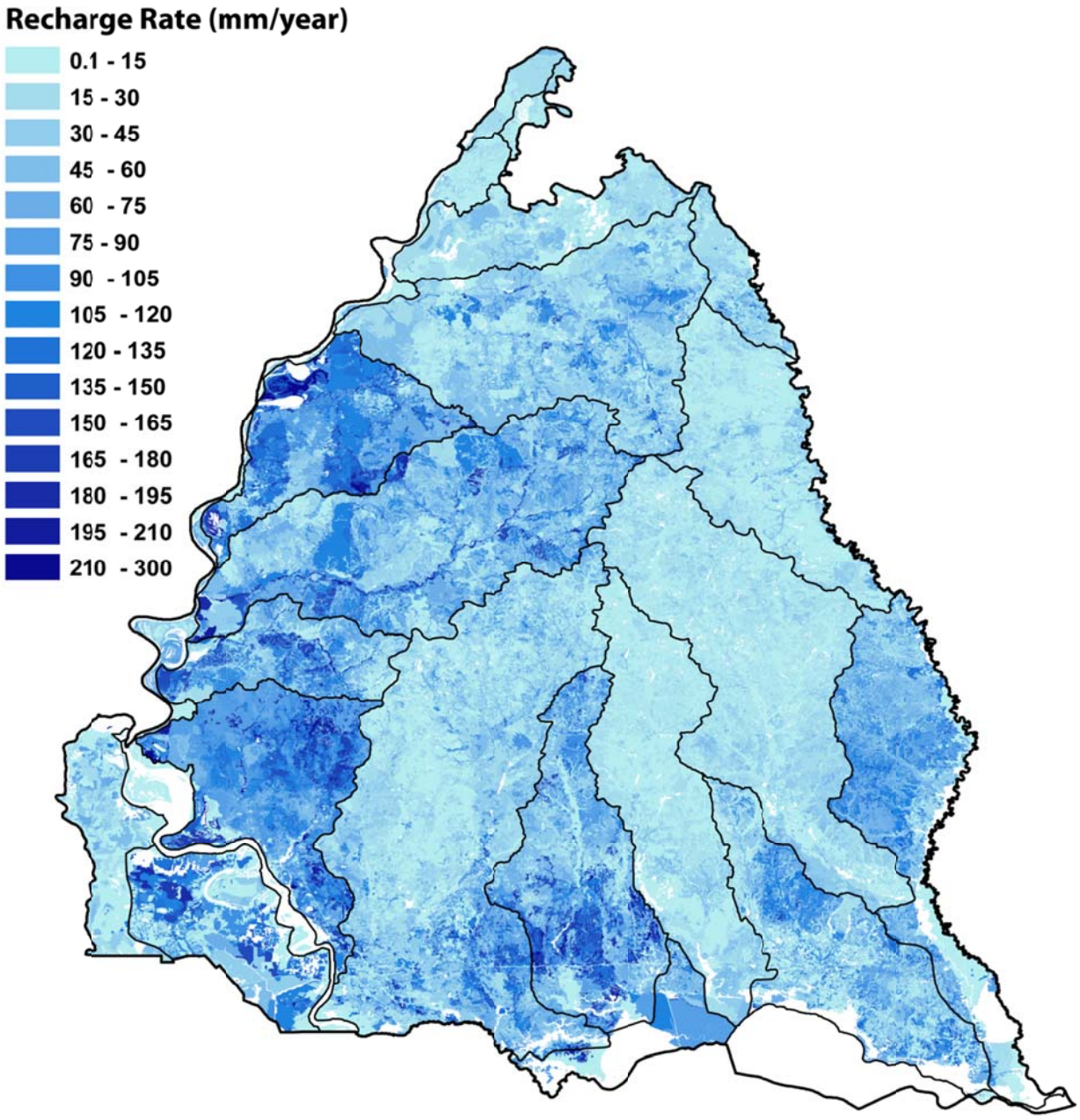

Figure 3.9: Mean annual recharge rate (mm/year) from 1950-2010 for the Southern Hills aquifer system.

Table 3.3 shows the mean annual recharge rate (1950-2010) for each hydrologic unit ranging from 97.59 mm/year for Coles Creek to 0.32 mm/year for Lower Mississippi-Baton Rouge. Coles Creek, Bayou Sara-Thompson, Tickfaw, Buffalo, Homochitto, Lower Grand, Lake Maurepas and Lower Pearl-Mississippi were estimated more than 50 mm/year mean annual

recharge rate. Table 3.3 also lists the anomaly of every 10-year mean annual recharge rate with respect to the 61-year mean annual recharge rate for each hydrologic unit.

Table 3.3: Change in 10-year mean annual recharge rate with respect to the mean annual recharge rate of 61 years for each hydrologic unit.

Hydrologic Unit Name	Mean recharge rate (mm/year)	Recharge anamoly (mm/year)					
	1950-2010	1950-1959	1960-1969	1970-1979	1980-1989	1990-1999	2000-2010
Amite	36.87	-2.03	1.49	4.4	-5.59	6.18	-4.04
Atchafalaya	21.67	2.89	-1.74	-4.01	-2.61	6.29	-1.39
Bayou Pierre	37.20	-24.05	-4.65	3.76	7.97	12.54	9.24
Bayou Sara-Thompson	95.33	-24.84	-19.85	9.83	-8.84	25.15	23.52
Bogue Chitto	18.52	1.69	-4.09	11.65	-3.6	-2.4	-3.59
Buffalo	69.08	-16.82	-4	0	0.65	7.3	16.23
Coles Creek	97.59	-5.94	-19.62	7.71	-10.31	-4.9	34.26
Homochitto	63.64	-9.83	-18.49	17.6	2.43	4.29	5.96
Lake Maurepas	55.38	-13.05	11.45	11.38	-1.48	-1.28	-4.4
Liberty Bayou-Tchefuncta	45.84	-5.62	-5.99	12.9	-9.93	6.5	3.26
Lower Big Black	19.83	-13.71	-0.19	3.03	5.81	4.86	2.95
Lower Grand	57.73	-18.3	-3.67	1.1	4.14	17.16	3.23
Lower Mississippi-Baton Rouge	0.32	-0.09	-0.3	-0.13	-0.16	0.05	0.65
Lower Mississippi-Natchez	21.32	-5.71	-2.76	0.74	-0.09	2.77	6.19
Lower Pearl-Mississippi	51.26	6.3	-9.91	2.8	3.07	12.26	-15.79
Lower Yazoo	21.18	-12.42	-11.08	4.93	11.28	2.67	7.12
Middle Pearl-Silver	16.81	0.96	-2.37	-1.74	-0.17	4.61	-1.47
Middle Pearl-Strong	26.21	-19.6	-8.86	-7.3	8.64	25.33	5.72
Tangipahoa	15.50	-0.75	1.74	16.94	-6.46	-3.71	-7.61
Tickfaw	70.40	-6.2	-1.92	21.52	4.12	2.4	-18.67

The maximum positive recharge anomaly was estimated 34.26 mm/year in 2000-2010 in Coles Creek. The maximum negative recharge anomaly was estimated -24.84 mm/year in 1950-1959 in Bayou Sara-Thompson. The spatially-distributed anomalies of the 10-year mean annual recharge rate with respect to the 61-year mean annual recharge rate are shown in Figure 3.10. High negative anomalies are seen in the first two decades (1950-1959 and 1960-1969) while high positive anomalies are seen in 1970-1979 and 1990-1999. In the recent decade 2000-2010, high positive anomalies in the west of the study area indicate high groundwater recharge to Miocene deposits. The magnitude of the anomaly relates to the amount of precipitation in the 10-year

period. For instance, precipitation was observed lower in the west of the study area in 1960-1969, which shows high negative recharge anomalies in this area. On the contrary, in 2000-2010, high precipitation was observed in the west of the study area, which results in high positive recharge anomalies.

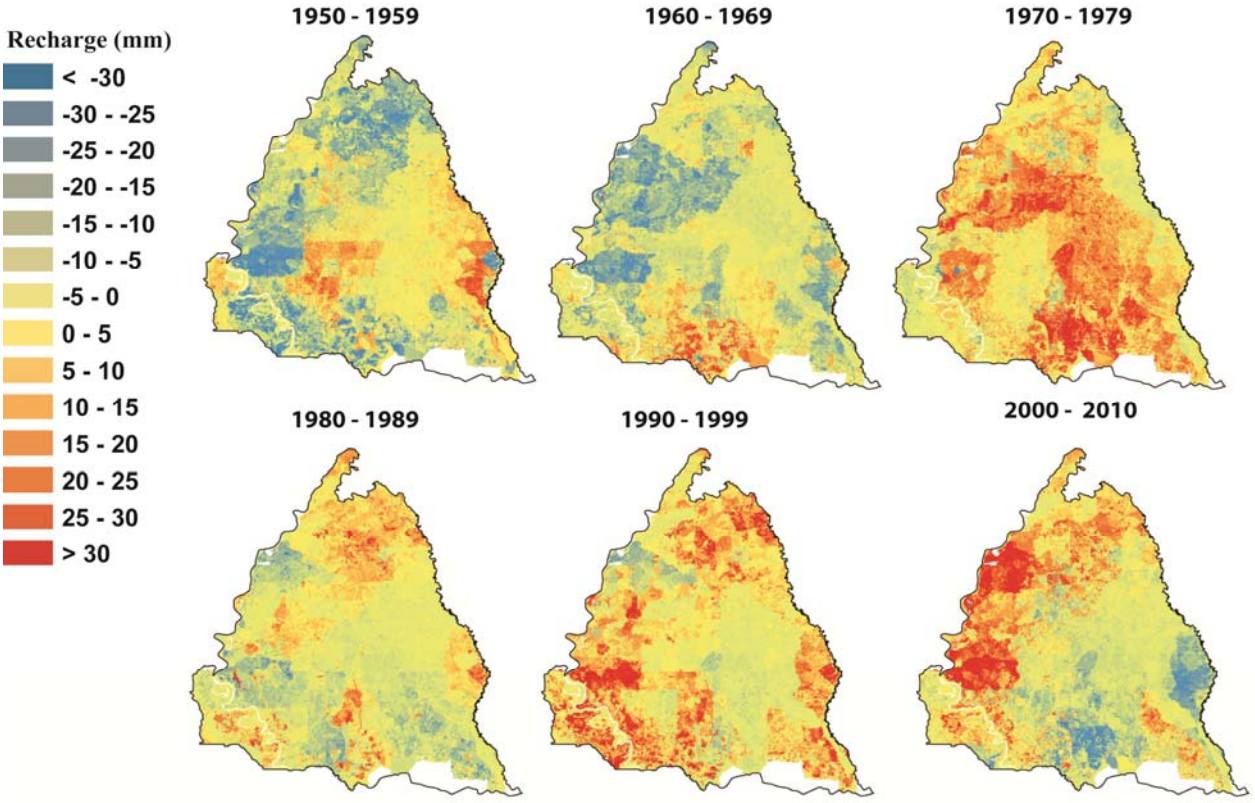

Figure 3.10: Recharge anomaly map for 10-year mean annual recharge with respect to the mean annual recharge rate (1950-2010) for the Southern Hills aquifer system.

The results of groundwater recharge estimation in this study provide important information for delineation of recharge zones (high recharge index or high recharge rate) as well as region-scale groundwater modeling for the Southern Hills aquifer system. Identifying recharge zones is greatly important in the context of groundwater resource protection as well as in the scope of development and land use management (Jyrkama and Sykes 2007). A potential risk assessment map can be produced to assess the vulnerability of the recharge zones to sources of

groundwater contamination by overlaying the map of recharge zones with locations of pollution sites (Hanson and Boniol 1985).

3.5. Conclusions

High-resolution groundwater recharge estimation for humid areas can be achieved by the proposed GIS-based water budget framework. The framework involves the USGS WaterWatch runoff database to calibrate HELP3 models and uses the MODIS evapotranspiration database to verify HELP3 models. By intersecting various datasets through GIS easily creates a great number of subdivisions, which makes recharge estimation virtually infeasible on a single computer. The framework includes parallel programming to distribute required HELP3 model runs over a cluster of supercomputers to significantly reduce computing time, which allows the methodology to be applied to groundwater recharge estimation of large-scale humid areas.

The framework was successfully applied to recharge estimation for the Southern Hills aquifer system. The mean annual recharge rate was estimated 47.5 mm/year which was 3.1% of the mean annual precipitation on the area of the Southern Hills aquifer system. The mean annual recharge showed moderate correlation (correlation coefficient of 0.76) to the mean annual precipitation. The recharge time lag map was obtained to understand the travel time of infiltrated precipitation reaching the last soil layer. The recharge index map quantifies percentage of precipitation becoming groundwater recharge. The map of mean annual recharge rate shows high groundwater recharge in the outcrops of the Miocene deposits. The hydrologic units, Coles Creek, Homochitto, and Buffalo may be considered as recharge zones to the deep sands in the Baton Rouge area because they showed higher average recharge rates from 1950 to 2010. These hydrologic units revealed greater changes of recharge for each 10-year from 1950 to 2010, due to greater sensitivity to precipitation change.

4. Comparative Study of CMIP3 Climate Projections

To investigate the impact of climate change on hydrologic projections for a large-scale humid region, in this chapter a water budget framework developed in chapter 3 is linked to climate model scenarios (Beigi and Tsai, 2015). Figure 4.1 shows the GIS-based water budget framework that creates subdivisions and links the HELP3 model with the three different emission scenarios of two CMIP3 GCMs to estimate potential recharge, surface runoff and ET under high performance computing. The framework is applied to the area of the Southern Hills aquifer system, southwestern Mississippi and southeastern Louisiana, USA, shown in Figure 4.2. The historical condition in 1950-2009 is used as a baseline and is compared to the results of six climate change scenarios for three future periods: 2010-2039, 2040-2069 and 2070-2099. The status quo of land use/land cover and soil type is assumed as input to HELP3 for 2010-2099.

In chapter 3, recharge was estimated by subtracting the baseflow from potential recharge (deep percolation), as it was considered that some part of potential recharge eventually can return to surface water bodies such as stream channels as baseflow. In this chapter, potential recharge is estimated since there is no projected baseflow available for the future. The same HELP3 input data, number of subdivisions (286,355) of study area mentioned in chapter 3 is used in this chapter.

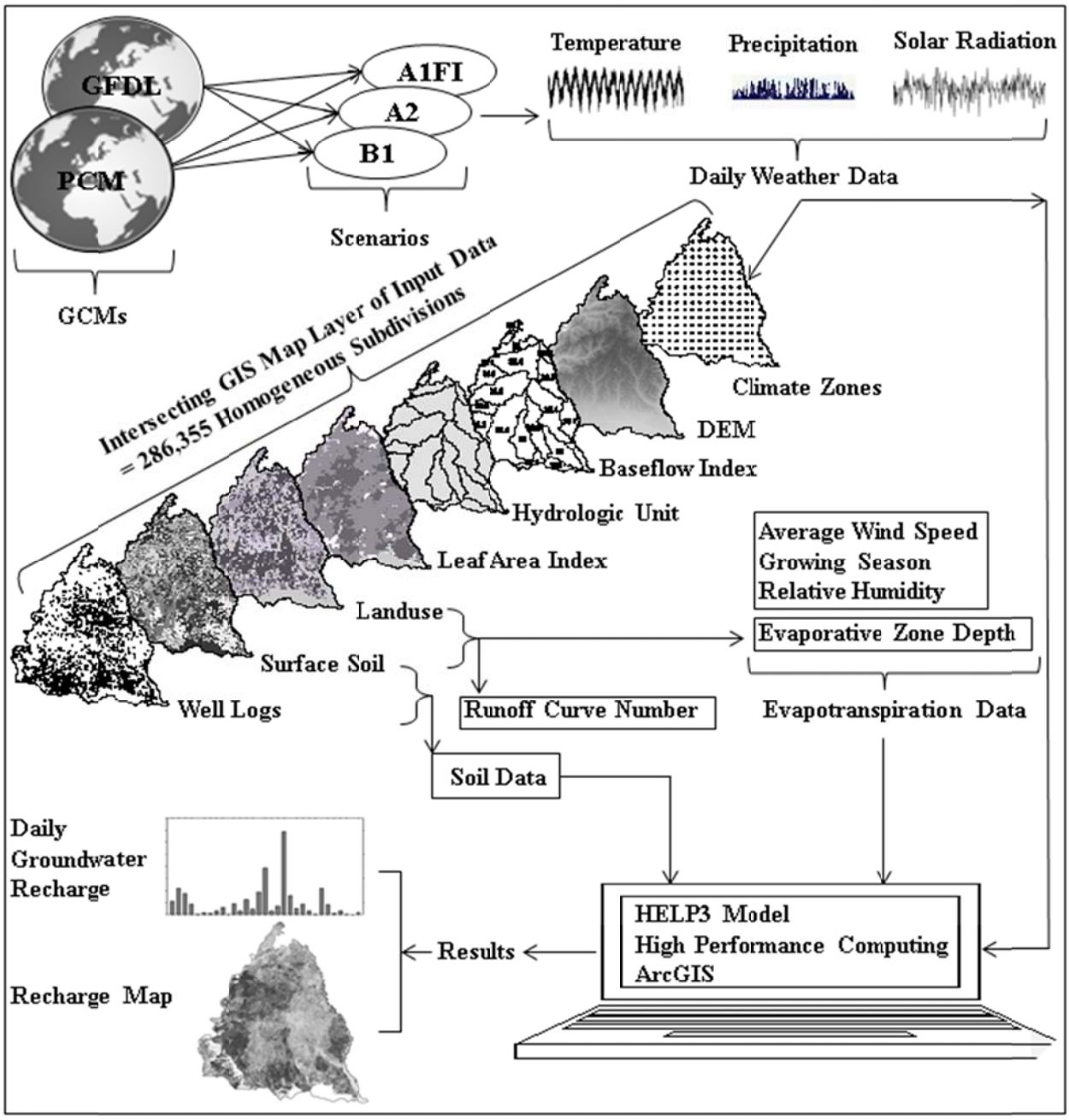

Figure 4.1: The geographic information system (GIS)-based water budget framework for estimating potential groundwater recharge, surface runoff and ET in the Southern Hills aquifer system

Figure 4.2: Location of the Southern Hills aquifer system (bounded by a thick black line). The parish boundaries are in thin black lines.

4.1. CMIP3 Climate Projections

After calibrating the HELP3 model using the baseline historical data from 1950 to 2009, six downscaled future climate time series of precipitation, temperature and solar radiation were

run through the HELP3 model to estimate future potential recharge, direct runoff, evapotranspiration, and water change in soil storage on a daily basis from 2010 to 2099. Daily values were then aggregated to provide monthly and annual estimates.

All GCM data used in this study were obtained from the USGS CASCaDE Project Climate Data. The downscaled daily precipitation and temperature data at a resolution of 12 km were generated by the constructed analogs method (Hidalgo et al. 2008) and were used as the input to the HELP3 model. The greenhouse gas emission scenarios used in this study are A2, B1 and A1FI, which were selected from the IPCC 4th climate assessment. The global climate model simulations are from the National Center for Atmospheric Research's Parallel Climate Model 1 (PCM) and the National Oceanic and Atmospheric Administration Geophysical Fluid Dynamics Lab's (GFDL) CM2.1 model. Each scenario produces different atmospheric concentrations of future greenhouse gases. A1FI is the fossil-fuel-intensive scenario, distinguished by rapid economic growth, and focuses on local and regional economic and social development, and thus represents the highest CO_2 emissions scenario. On the other hand, B1 represents the lowest CO_2 emissions scenario due to the emphasis on clean and resource-efficient technology, lower population growth, and global solutions to economic, social and environmental sustainability. A2 represents the middle-of-the-road emission scenario of climate change projections which has CO_2 concentration higher than B1 and lower than A1FI scenario. The emission scenarios A2, B1 and A1FI are described in detail by Nakicenovic et al. (2000).

In order to consider a wide range of possible futures, the downscaled emission scenarios used in this study are ranging from an optimistic scenario (B1) to a relatively resigned one (A2, emissions continuing to grow throughout the 21st Century), and to a more pessimistic scenario (A1FI) that results in higher climatic change responses than other scenarios. In addition, the

reason for selecting two different GCMs is that PCM is near the most benevolent end of the spectrum of projections of most IPCC climate models, which means that PCM warms nearly the least and has approximately the least climate change responses to a given amount of greenhouse gas inputs, compared to other GCMs. On the other hand, GFDL has the greatest warming and climate change feedback per unit of greenhouse gas added to the atmosphere (Dettinger 2013). Therefore, the most pessimistic case was viewed as the highly responsive GFDL model forced by the high-emission A1FI scenario and the most optimistic case is the relatively low sensitivity PCM model run under the low-emission B1 scenario. As a result, considering both GCMs, along with high and low emission scenarios in this study, will allow us to include a wide range of future possible projections presented by the IPCC 4th Assessment projection.

4.2. Results and Discussion

4.2.1. Historical and Projected Climate Forcing

Historical daily precipitation and temperature data with a resolution of 12 km from 1950 to 2009 were obtained from Maurer et al. (2002) and Maurer (2013). The daily temperature and precipitation observations are obtained from the National Oceanic and Atmospheric Administration (NOAA) Cooperative Observer (COOP) stations and gridded to 12 km spatial resolution. Daily values then aggregated to provide monthly averages of precipitation and temperature. The trend of annual precipitation and temperature for the entire study area for 1950-2010 are respectively shown in Figure 4.3 and Figure 4.4. Precipitation shows slightly increasing trend for 1950-2010. Figure 4.4 shows increasing trend in temperature for 1950-2010.

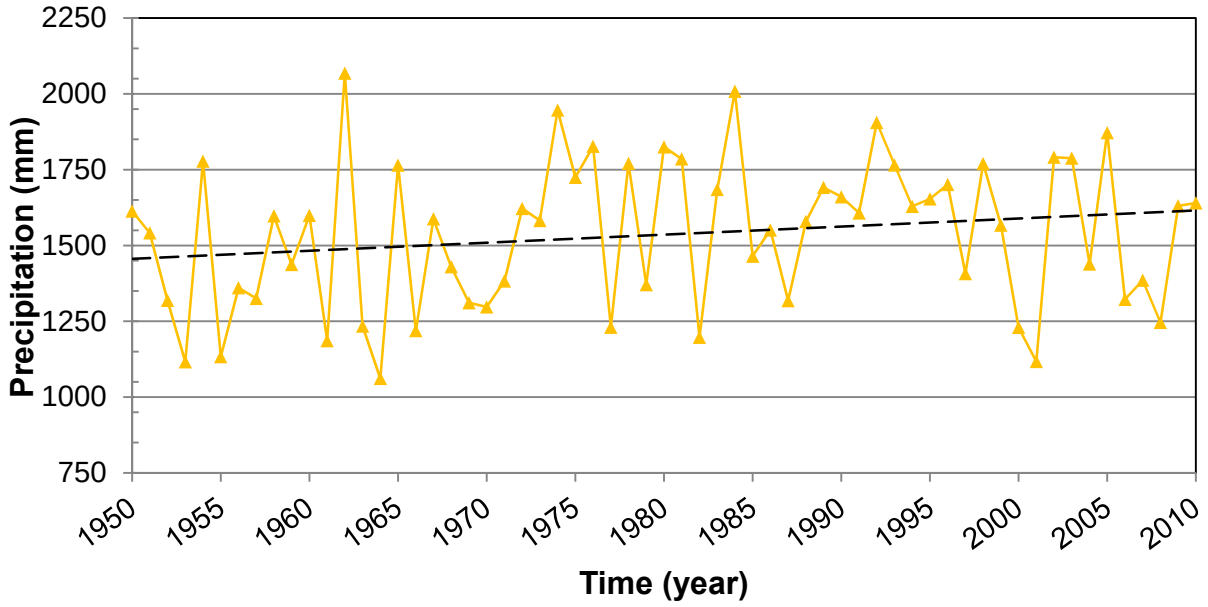

Figure 4.3: Mean annual precipitation from 1950-2010 for southeastern Louisiana and southwestern Mississippi.

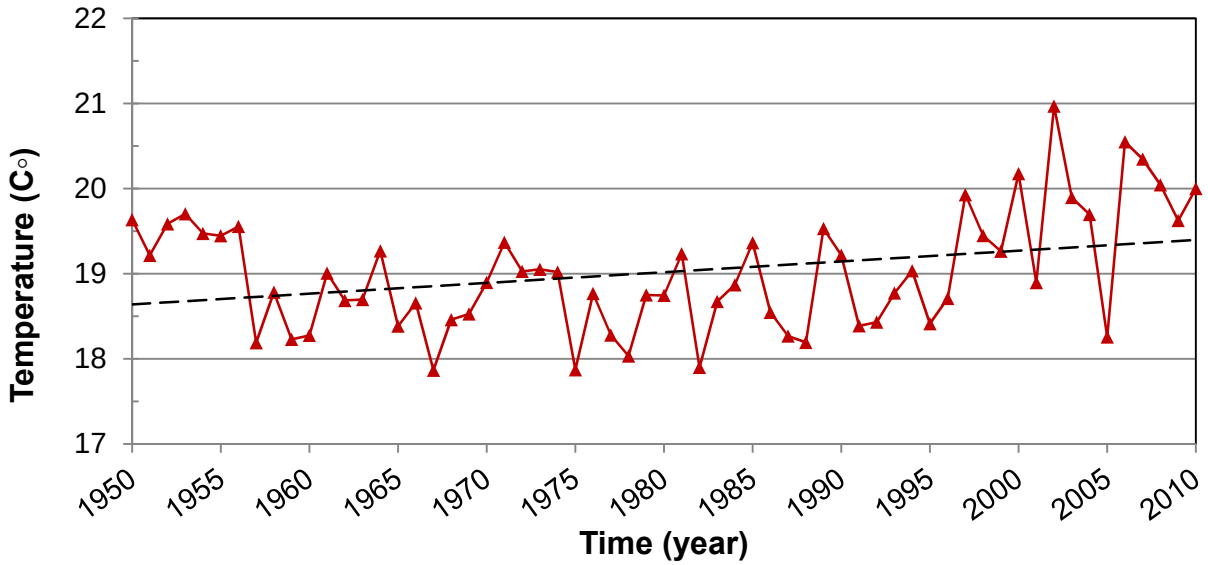

Figure 4.4: Mean annual precipitation from 1950-2010 for southeastern Louisiana and southwestern Mississippi.

Table 4.1 lists the baseline information from 1950 to 2009 and the projected changes in the 30-year mean annual precipitation, temperature, and solar radiation for 2010-2039, 2040-

2069, 2070-2099 with respect to the baseline information for the area of the Southern Hills aquifer system. The mean annual precipitation, temperature and solar radiation in 1950-2009 are 1522.1 mm, 18.9 °C and 15.65 MJ/m^2, respectively. All the scenarios show increasing trend in temperature in 2010-2099; however, precipitation and solar radiation may decrease or increase. The temperature is projected to increase between 0.90 °C and 5.31 °C for the 21st century. A1FI scenario projects the highest temperature increase, followed by A2, and then B1 scenarios. This order follows the trend of global averaged radiative forcing (greenhouse gases minus sulfate aerosols) imposed on various recent projections of the historical and 21st Century climate change (Cubasch et al. 2001).

The study area has dramatic precipitation projections for the 21st century in some cases. As shown in Table 4.1, according to the PCM model, the study area may have precipitation increase as high as 4.36 % and may have precipitation decrease as low as −8.75 %. GFDL projects as high as 3.04 % increase in precipitation. However, significant precipitation decrease 18.94 % is projected in 2070-2099. Precipitation is more likely to increase in 2010-2039, but more likely to decrease in 2070-2099. The PCM model generally projects more precipitation than that of the GFDL model.

Table 4.1: Projected changes in mean annual precipitation, temperature, and solar radiation with respect to the mean annual for 1950-2009.

Climate model	Scenario	Precipitation (%) Mean annual =1522.1 mm			Temperature (ºC/year) Mean annual =18.9 ºC			Solar radiation (%) Mean annual=15.6 MJ/m^2		
		2010-2039	2040-2069	2070-2099	2010-2039	2040-2069	2070-2099	2010-2039	2040-2069	2070-2099
PCM	B1	+2.60	+4.36	−5.30	+0.036	+0.039	+0.055	−1.37	−1.28	−0.03
	A2	+3.46	+2.20	−0.43	+0.032	+0.055	+0.081	−1.15	−0.66	−0.64
	A1FI	+3.78	−1.38	−8.75	+0.043	+0.071	+0.121	−1.48	−0.56	−0.11
GFDL	B1	−0.24	+2.73	+3.04	+0.040	+0.051	+0.072	+1.17	+0.56	+0.46
	A2	+0.76	−3.54	−14.17	+0.037	+0.076	+0.137	+0.47	+1.36	+2.64
	A1FI	+3.00	−7.99	−18.94	+0.030	+0.098	+0.177	−0.11	+1.64	+3.49

The PCM model projects decrease in solar radiation ranging from −0.03 % to −1.48 % for the 21st century. In contrast, the GFDL model projects increase in solar radiation ranging

from +0.46 % to +3.49 % for the 21st century except for the A1FI scenario, which projects 0.11% decrease in solar radiation in 2010-2039.

4.2.2. Baseline Historical Potential Recharge

The mean annual potential recharge shown in Figure 4.5 for the area of the Southern Hills aquifer system is considered as the baseline historical recharge for climate change comparisons. The mean annual potential recharge ranges from 0 to 857 mm. The average of the mean annual potential recharges (1950-2009) for the entire area is 227.5 mm. 45.6 % of the subdivisions have mean annual potential recharge above the average. 48.8 % of the subdivisions have mean annual potential recharge lower than 205 mm while 40.7 % have mean annual potential recharge between 205 mm and 410 mm, and 10.45 % have mean annual potential recharge higher than 410 mm. The west of the study area (including the parishes of Adams County, Claiborne County, Jefferson County, Wilkinson County, and West Feliciana) is the recharge zone of the Baton Rouge aquifer system (Buono 1983) and shows high potential recharge historically. High potential recharge is also demonstrated in the east and central Florida parishes. Low potential recharge is demonstrated in the north and northeast of the study area.

4.2.3. Temporal Results

The changes in temperature and the cumulative changes in precipitation and solar radiation for individual scenarios with respect to the historical baseline (1950-2009) are shown in Figure 4.6. To calculate the changes for the Southern Hills aquifer system, the area-averaged values of the climate variables of all subdivisions were calculated and subtracted from the mean annual for 1950-2009. Sums of the changes over years show the cumulative changes. If changes in climate variables are negative over time, their cumulative changes will amplify this

phenomenon by showing large negative values. For example, a fall of almost 10 m cumulative change in 2099 for GFDLA1F1 shows that the yearly precipitation continuously decreases from 2040 to 2099 with respect to the baseline precipitation.

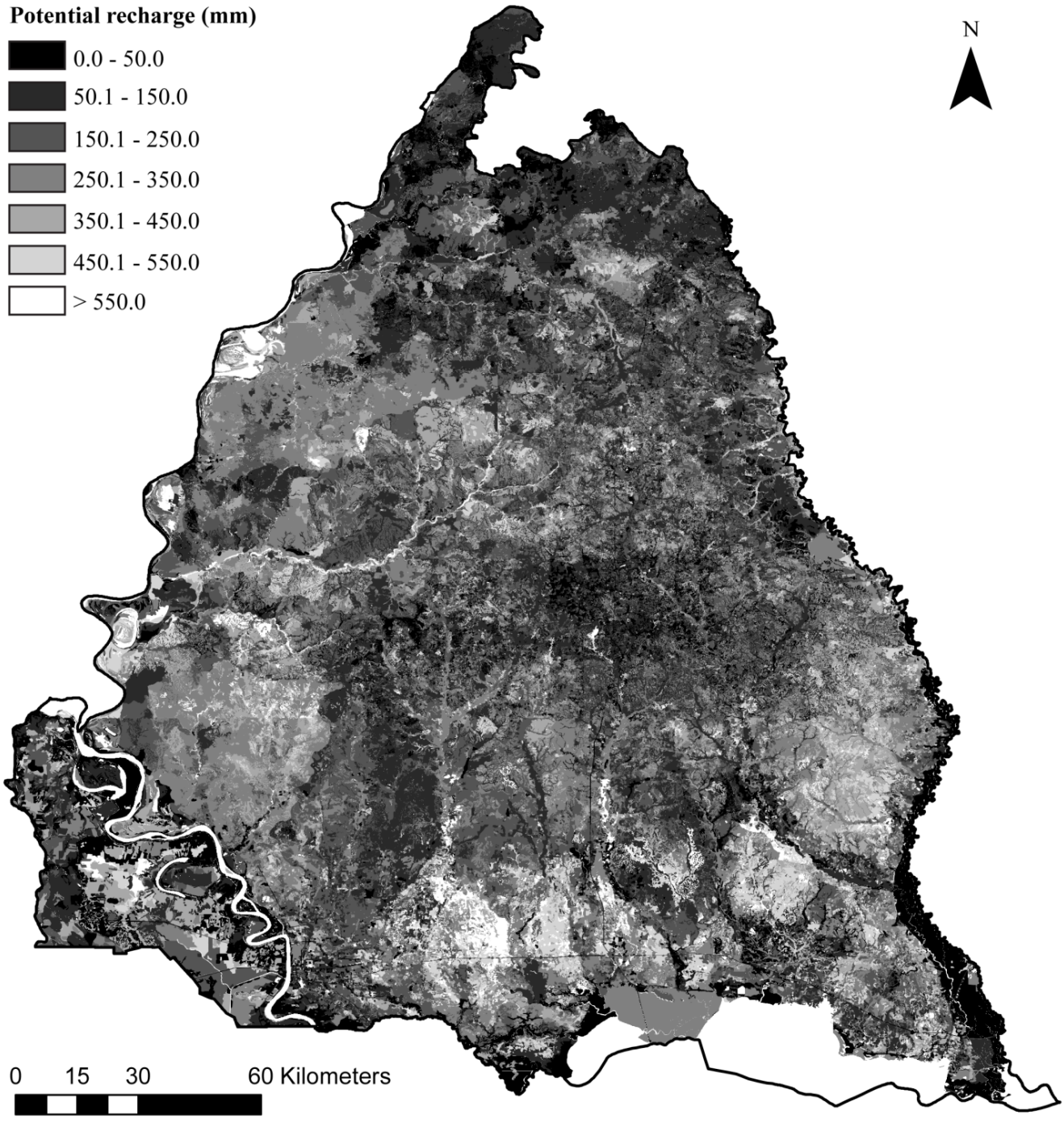

Figure 4.5: Mean annual potential recharge (mm) for 1950-2009 for the Southern Hills aquifer system.

The differences of the cumulative changes between the scenarios become more evident over time. The cumulative changes of solar radiation projected by the PCM and GFDL models are opposite and distinguishable from the beginning of projection. After the mid-century, the cumulative changes of precipitation and the changes of temperature between emission scenarios are distinguishable, which is consistent with the global projections (Cubasch et al. 2001). Scenarios PCMB1, PCMA2, and GFDLB1 project overall precipitation increase while the other three scenarios project overall precipitation decrease for the 21st century. Moreover, scenarios PCMB1, PCMA2, and GFDLB1 project relatively less temperature change than the other three scenarios for the 21st century.

In general, the projections of the PCM and the GFDL models begin to diverge greatly after the mid-century for the study area. This divergence is in harmony with greenhouse forcing associated with the various scenarios and starts at the point at which substantial differences between the projections by these two models begin. These differences stem from the two models' parameterizations, sensitivities and responses to greenhouse gases and other forcings (Cayan et al. 2007).

Figure 4.7 presents the cumulative changes in potential recharge, runoff and evapotranspiration with respect to the historical baseline scenario for each climate change scenario. It is observed that potential recharge cumulative changes follow the same trend as precipitation cumulative changes, which highlights the fact that the potential recharge in the study area is more sensitive to precipitation than temperature and solar radiation. Scenarios GFDLA2 and GFDLA1FI project significant potential recharge decrease towards the end of the 21st century. On the other hand, scenarios PCMB1 and PCMA2 project the most potential recharge increase for the 21st century. Almost all of the climate change scenarios project runoff

decreases for the 21st century except for the GFDLB1. PCMA1FI projects the highest runoff reduction, followed by PCMB1. Although projecting precipitation increase for the 21st century, scenarios PCMB1 and PCMA2 show runoff decrease due to projected high evapotranspiration shown in Figure 4.7(c). The PCM model projects continuous evapotranspiration increase for the 21st century. However, the GFDL model does not show significant change of evapotranspiration before 2069, but has a wide-ranging evapotranspiration projection in 2070-2099.

4.2.4. Spatial Results

Future mean annual potential recharge, runoff, and evapotranspiration with respect to the mean annual from 1950 to 2009 are listed in Table 4.2. The mean annual potential recharge, runoff, and evapotranspiration in 1950-2009 are 227.5 mm, 362.7 mm and 943.2 mm, respectively. The PCM model projects recharge change from −33.7 % to +19.1 % and the GFDL model projects recharge change from −58.1 % to +7.1 % for the 21st century. In general, the PCM projects more recharge than the GFDL. The potential recharge is likely to increase in 2010-2039 and is likely to decrease in 2070-2099. The mean annual potential recharge in 2070-2099 is projected to decrease from 227.5 to 95.4 mm/year under the most pessimistic scenario (GFDLA1FI), and decrease to 192.5 mm/year under the most optimistic scenario (PCMB1). As a result, the potential recharge to the Southern Hills aquifer system is projected to be reduced in 2070-2099 as the climate change studies have projected for other places (e.g., Serrat-Capdevila et al. 2007; Wegehenkel and Kersebaum 2009; Ali et al. 2012).

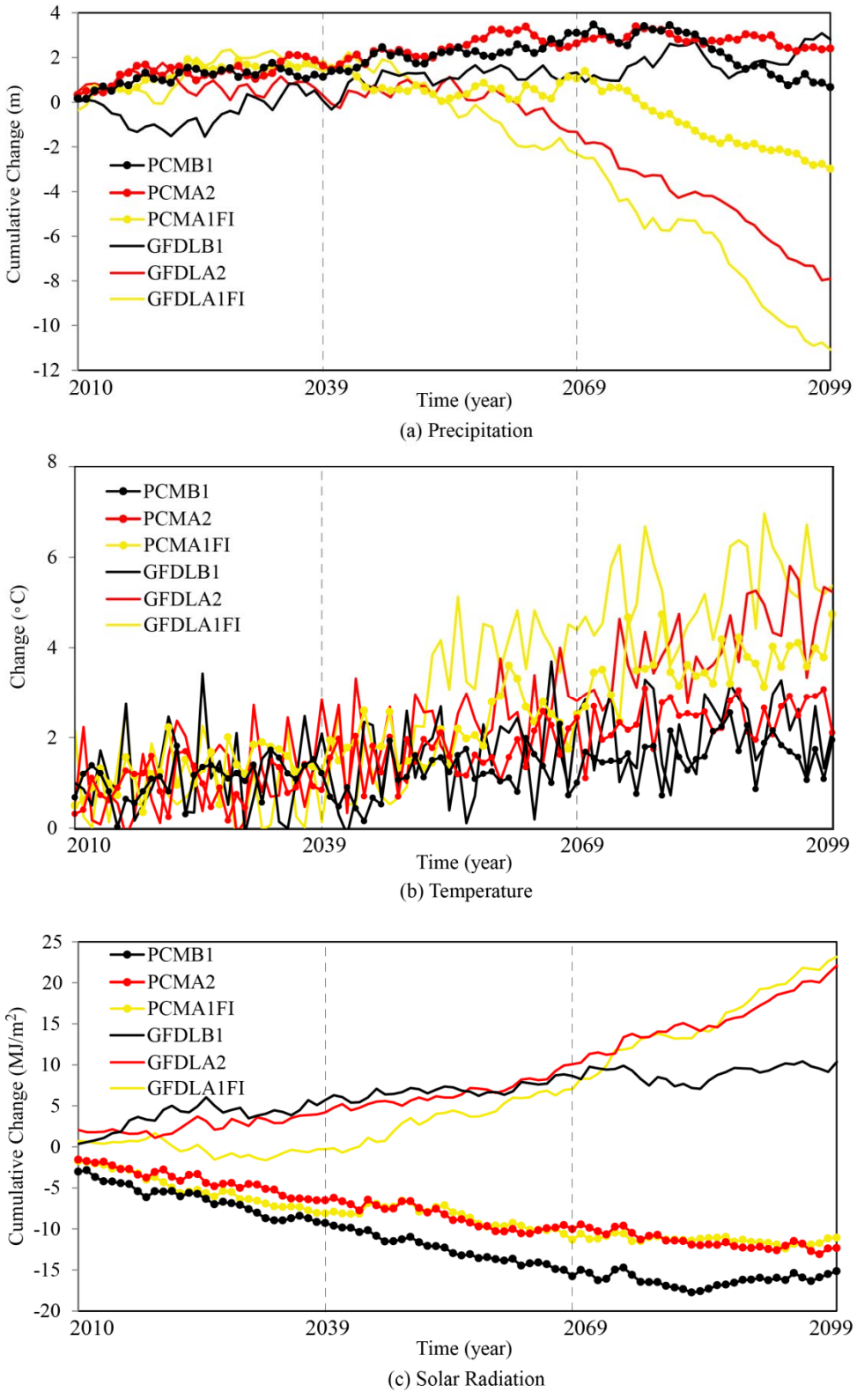

Figure 4.6: Cumulative changes of (a) precipitation, (b) changes of temperature, and (c) cumulative changes of solar radiation with respect to the historical baseline

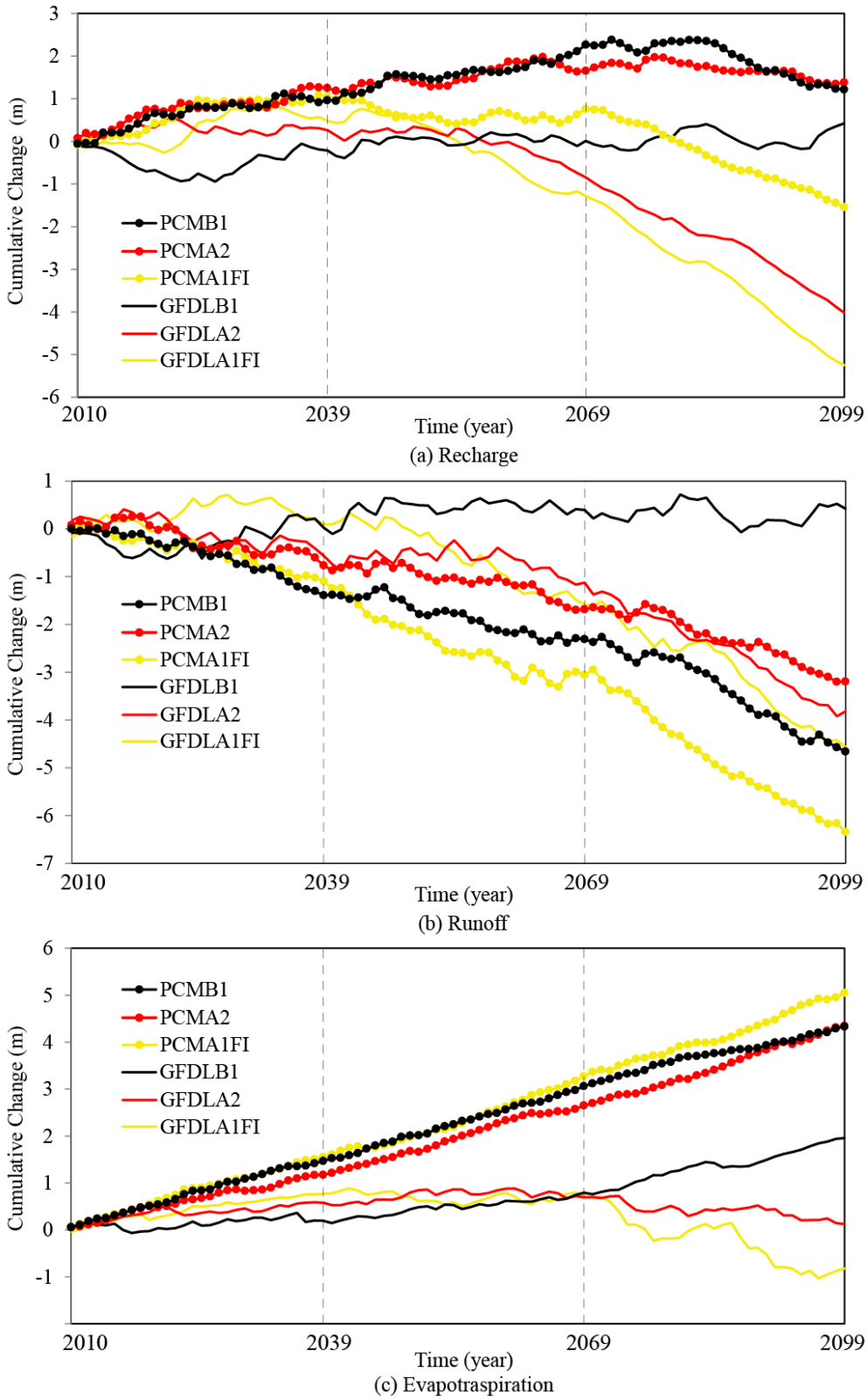

Figure 4.7: Cumulative changes of (a) potential groundwater recharge, (b) surface runoff, and (c) evapotranspiration with respect to the historical baseline.

Table 4.2: Projected changes in mean annual potential recharge, runoff and evapotranspiration with respect to the mean annual for 1950-2009.

Climate model	Scenario	Potential recharge (%) Mean annual = 227.5 mm			Runoff (%) Mean annual = 362.7 mm			Evapotranspiration (%) Mean annual = 943.2 mm		
		2010-2039	2040-2069	2070-2099	2010-2039	2040-2069	2070-2099	2010-2039	2040-2069	2070-2099
PCM	B1	+14.1	+19.1	−15.4	−12.8	−8.4	−21.6	+5.2	+5.6	+4.5
	A2	+18.4	+5.9	−4.0	−7.0	−8.4	−13.9	+4.1	+5.2	+6.0
	A1FI	+15.4	−4.2	−33.7	−10.1	−18.0	−30.2	+5.5	+6.1	+6.3
GFDL	B1	−3.1	+3.3	+6.0	+0.2	+3.4	+0.2	+0.7	+2.1	+4.1
	A2	+3.9	−16.3	−46.5	−5.1	−5.2	−24.8	+2.1	+0.4	−2.0
	A1FI	+7.1	−25.8	−58.1	+0.9	−15.5	−27.4	+2.7	−0.2	−5.4

Runoff is likely to decrease for the 21st century as projected by the GCMs (Table 4.2). PCM projects runoff decrease from −7.0 % to −30.2 % while GFDL projects runoff change from +3.4 % to −27.4 %. In general, PCM projects less runoff than GFDL for the 21st century. Evapotranspiration is likely to increase for the 21st century. The PCM projects evapotranspiration increase from 4.1 % to 6.3 % and the GFDL projects evapotranspiration change from −5.4 % to +4.1 %.

In order to understand the range of possible future changes in potential recharge, results from the most optimistic scenario (PCMB1) and the most pessimistic scenario (GFDLA1FI) are investigated. Figure 4.8 shows the changes in 30-year mean annual potential recharge with respect to the mean annual potential recharge (1950-2009). The PCMB1 projects relatively higher potential recharge increase in southeastern Louisiana than southwestern Mississippi in 2010-2039 and 2040-2069. Recharge is projected to decrease in 2070-2099. The GFDLA1FI also projects more potential recharge in southeastern Louisiana in 2010-2039. Potential recharge is projected to decrease in 2040-2069 by the GFDLA1FI and more severely in 2070-2099. In general, the PCM model projects more potential recharge than that of the GFDL model.

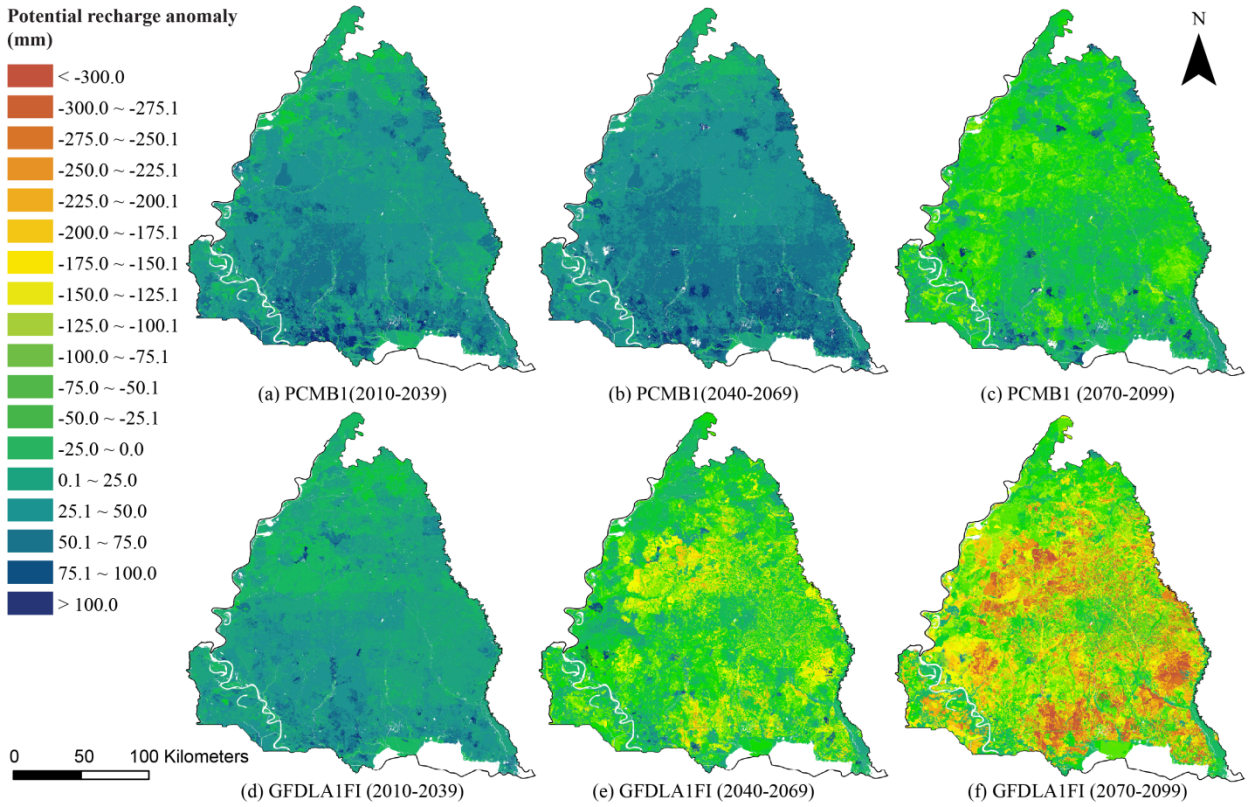

Figure 4.8: Potential recharge anomaly map for three future periods (2010-2039, 2040-2069, and 2070-2099) for the most optimistic scenario (PCMB1) and the most pessimistic scenario (GFDLA1FI), Each map shows the changes in 30-year mean annual potential recharge with respect to the mean annual potential recharge (1950-2009) in Figure 4.5.

4.2.5. Sensitivity Analyses of Recharge to Climate Change

The sensitivity of potential recharge to climate change was evaluated by using the linear regression method to analyze the relationship between the change in potential recharge and the change in individual climate variables such as precipitation, temperature and solar radiation under different climate change scenarios (Crosbie et al. 2013). To calculate the sensitivities, the mean annual precipitation, temperature and solar radiation are varied by $\pm 5\%, \pm 10\%, \pm 15\%$ $\pm 20\%, \pm 25\%$, and $\pm 30\%$. The 5 % increment accounts for approximately ΔP=61.82 mm, ΔT=1.21 °C, and ΔS=0.77 MJ/m^2 for the precipitation, temperature and solar radiation

respectively. The annual variations are translated to the daily precipitation, temperature and solar radiation variations for running the HELP3 model. The time period 2070-2099 was chosen for analysis because this period has wide projected cumulative changes between emission scenarios and between the climate models shown in Figure 4.5. The mean annual potential recharge changes are computed for each subdivision. Then, the area-averaged method is used to derive the overall potential recharge changes from all subdivisions for the Southern Hills aquifer system.

The relationship between a change in mean annual potential recharge relative to a change in mean annual precipitation, temperature and solar radiation for the six scenarios is illustrated in Figure 4.9. The relationship between the change in climate variables and change in recharge is not quite linear (McCallum et al 2010). Nevertheless, using linear regression, Crosbie et al. (2013) suggests that the slope of a line represents the sensitivity of the potential recharge to a climate variable given a climate change scenario; and the intercept to the y axis represents the sensitivity of the potential recharge to all other variables. From Figure 4.9, it is clear that the potential recharge increases as precipitation increases, temperature decreases, or solar radiation decreases, regardless of the considered climate change scenarios. Moreover, the potential recharge change is most sensitive to precipitation change, followed by solar radiation change, and then temperature change. Table 4.3 lists the numerical values of the slope and intercept for Figure 4.9. Potential recharge sensitivity to precipitation, temperature and solar radiation is intensified from B1, to A2, and to A1FI as a result of the increment of the degree of global warming. In general, the GFDL model shows higher potential recharge sensitivity than the PCM model.

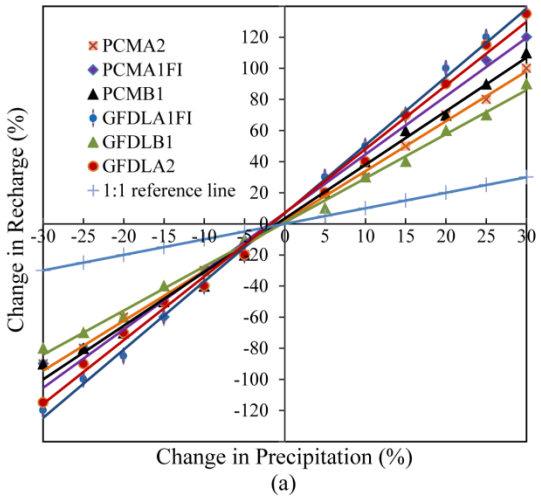

Figure 4.9: Relationship between changes in mean annual potential recharge and changes in mean annual (a) precipitation, (b) temperature, and (c) solar radiation for different scenarios

Table 4.3: Slopes and intercepts of the relationships between changes in mean annual potential recharge and changes in mean annual precipitation, temperature, and solar radiation.

Scenario	Precipitation		Temperature		Solar Radiation	
	Slope	Intercept	Slope	Intercept	Slope	Intercept
PCMB1	3.21	3.33	-1.18	-6.25	-1.87	2.92
PCMA2	3.45	1.67	-1.58	-7.50	-2.14	5.83
PCMA1FI	3.75	7.08	-2.07	-4.17	-2.19	9.17
GFDLB1	2.84	0.83	-1.45	-6.67	-2.34	7.50
GFDLA2	4.09	6.67	-1.71	-0.83	-2.52	7.92
GFDLA1FI	4.38	7.08	-2.10	8.33	-2.67	9.17

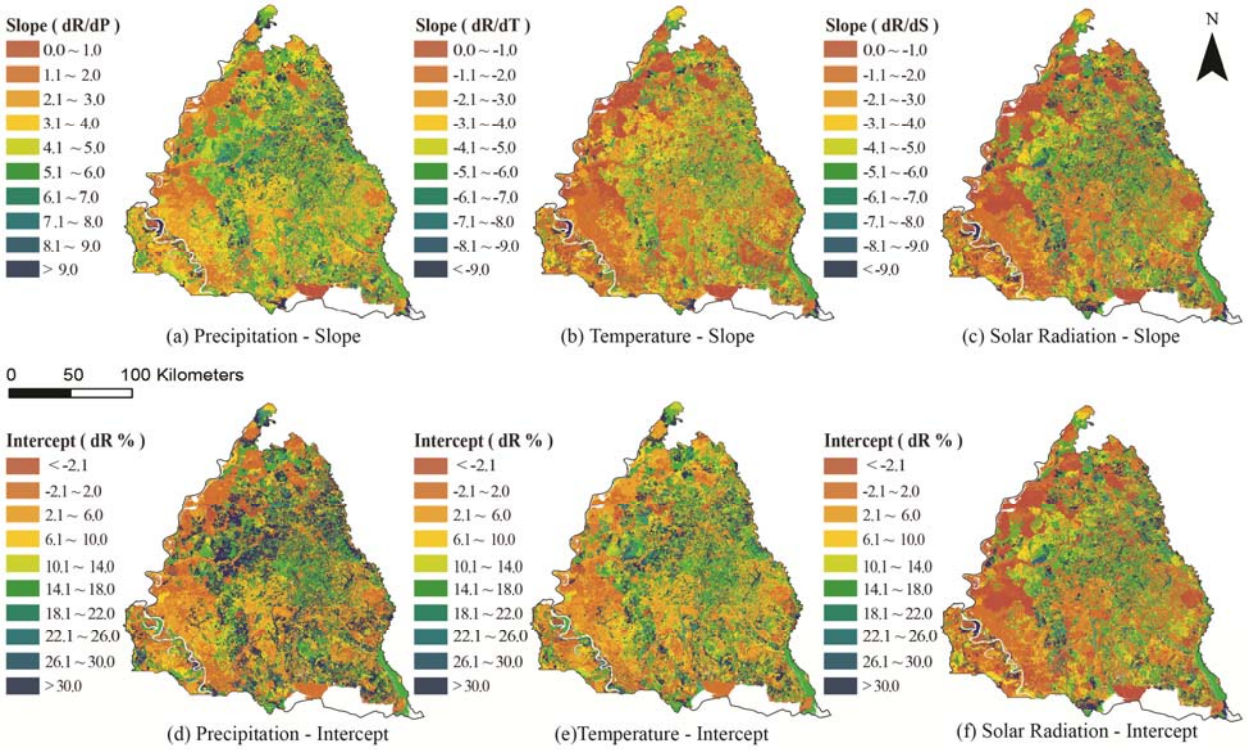

Figure 4.10: Slopes and intercepts of the relationship between changes in mean annual potential recharge and changes in mean annual precipitation, temperature and solar radiation for GFDLA1FI for 2070-2099.

A sensitivity analysis was conducted for each subdivision to assess sensitivity variation in space. This study selected GFDLA1FI scenario for the period 2070-2099 since it shows the highest potential recharge change for the study area. As shown in Figure 4.10, subdivisions with high potential recharge have the lowest slope and intercept while subdivisions with low potential

recharge have the highest slope and intercept. As a result, subdivisions with high potential recharge show lower potential recharge sensitivity to precipitation, temperature and solar radiation and vice versa.

4.2.6. Error and Uncertainty Analyses

Uncertainties in climate modeling, greenhouse gas emission, and internal variability of the climate system are the three major sources of uncertainty in climate change projections (Yip et al. 2011). This study focuses on the climate modeling uncertainty and greenhouse gas emission uncertainty that result in uncertain future precipitation and temperature, and ultimately impact on future potential recharge. As stated previously, the chosen six climate change scenarios include a wide range of future possible projections, which suggests the need to conduct uncertainty analysis on climate change. Uncertainty in the HELP3 model was not studied.

The variation of projected annual potential recharge for 2010-2099 under six scenarios for the Southern Hills aquifer system is shown in Figure 4.11. While the variation across scenarios is large, the general trend shows decreasing potential recharge toward 2099. The annual potential recharges of the six scenarios have mean annual potential recharge 213.3 mm and standard deviation 48.68 mm.

The uncertainties due to errors in estimation of daily observed precipitation and temperature data for 1950-2009 are also analyzed. For each climate zone, the daily observed precipitation and temperature are compared to the downscaled data of the PCM and the GFDL. The downscaled data are different from observed data. The downscaled data contains the results from aggregating the gridded observations up to the coarseness of the roughly 2.5x2.5 degree latitude longitude grid and then downscaling them back onto the original 12-km resolution grid, for use in checking the downscaling method.

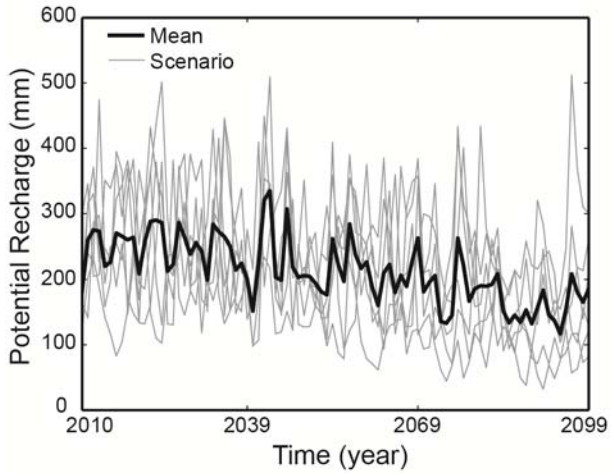

Figure 4.11: Annual potential recharge from 2010 to 2099 for the area of the Southern Hills aquifer system. The gray lines represent the six scenarios. The black line represents the average of the six scenarios.

Figure 4.12 shows the daily estimation errors versus GFDL downscaled data for a specific climate zone centered at latitude 31.4375 and longitude -91.4375, where the precipitation error is $E_{\mathrm{P}} = P_{\mathrm{downscaled}} - P_{\mathrm{observed}}$ and the temperature error is $E_{\mathrm{T}} = T_{\mathrm{downscaled}} - T_{\mathrm{observed}}$. The errors account for the performance of GCMs and the performance of the downscaling technique. The distribution features of daily estimation errors with respect to the downscaled data for the other 234 climate zones are similar to Figure 4.12.

The daily precipitation errors and daily temperature errors have quite different distribution features and are not normally distributed. Daily downscaled precipitation data contain large errors and are significantly biased. The 25th percentile shows that precipitation data errors increase as the downscaled precipitation increases. Nevertheless, most downscaled precipitation data are between 0 and 1 mm, and the strong skewness of low downscaled precipitation data shows significant underestimation with respect to high observed precipitation. The errors of the daily downscaled temperature data show relatively less bias and the distribution is less skewed than the downscaled precipitation data.

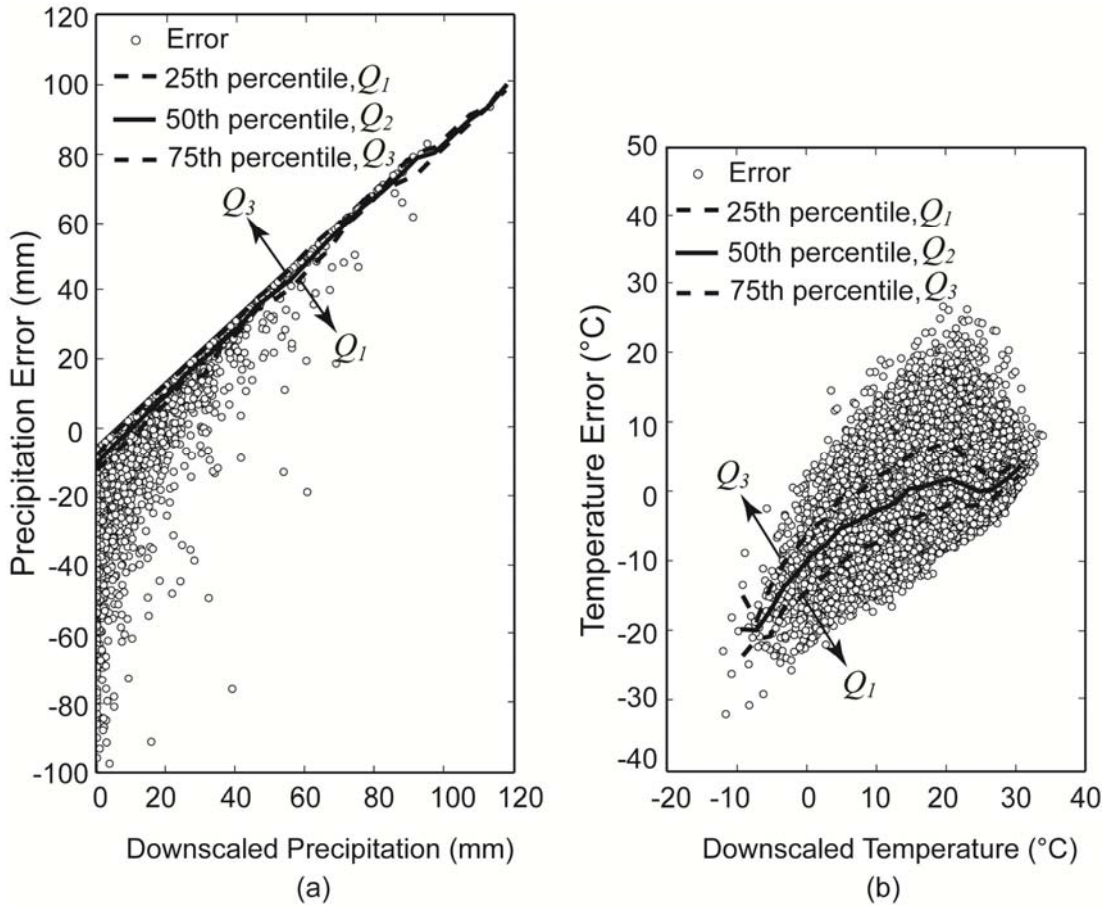

Figure 4.12: Estimation errors of (a) projected daily precipitation and (b) projected daily temperature from 1950 to 2009 for a climate zone centered at latitude 31.4375 and longitude -91.4375 using the GFDL model.

The error propagation from the daily projected precipitation and temperature, through the hydrologic model HELP3, to future potential recharge is quantified. The projected downscaled data for 2010-2099 were adjusted according to the 25th percentile (the first quartile, Q_1), the 50th percentile (the second quartile, Q_2), and the 75th percentile (the third quartile, Q_3) of the errors shown in Figure 4.12. That is

$$\begin{aligned} P_{\mathrm{Q_i}} &= P_{\mathrm{downscaled}} - E_{\mathrm{P,Q_i}} \\ T_{\mathrm{Q_i}} &= T_{\mathrm{downscaled}} - E_{\mathrm{T,Q_i}} \end{aligned} \tag{22}$$

where P_{Q_i} is the adjusted downscaled precipitation data, T_{Q_i} is the adjusted downscaled temperature data, E_{P,Q_i} is the i^{th} quartile precipitation error, E_{T,Q_i} is the i^{th} quartile temperature error, and i=1, 2, and 3. Eq. (22) shows $P_{Q_1} > P_{Q_2} > P_{Q_3}$ and $T_{Q_1} > T_{Q_2} > T_{Q_3}$. Consequently, a total of 54 different realizations result from the combinations of the three quartiles of projected daily precipitation, the three quartiles of projected daily temperature, and the six climate change scenarios.

The realizations of projected annual potential recharge for 2010-2099 for the Southern Hills aquifer system, shown in Figure 4.13, are categorized into 9 groups based on the three quartiles of projected daily precipitation and the three quartiles of projected daily temperature. Similar to Figure 4.11, the potential recharge variation across the six climate change scenarios is large for all groups. The potential recharge variation under the projected high precipitation (P_{Q_1}) is smaller than that under projected median and low precipitations (P_{Q_2} and P_{Q_3}). Given the same projected precipitation, increasing temperature results in less potential recharge. Given the same projected temperature, increasing precipitation results in more potential recharge. As shown in Figure 4.13, the changes in potential recharge highlight the fact that precipitation influences more than temperature on potential recharge. Given the projected high precipitation (P_{Q_1}), the average of the annual potential recharges of the six scenarios shows the general trend of decreasing potential recharge toward 2099. The projected median and low precipitations (P_{Q_2} and P_{Q_3}) result in no or slightly increasing trend in potential recharge. The mean of the annual potential recharge varies from 152.9 mm (the P_{Q_3}-T_{Q_1} combination) to 365.2 mm (the P_{Q_1}-T_{Q_3} combination).

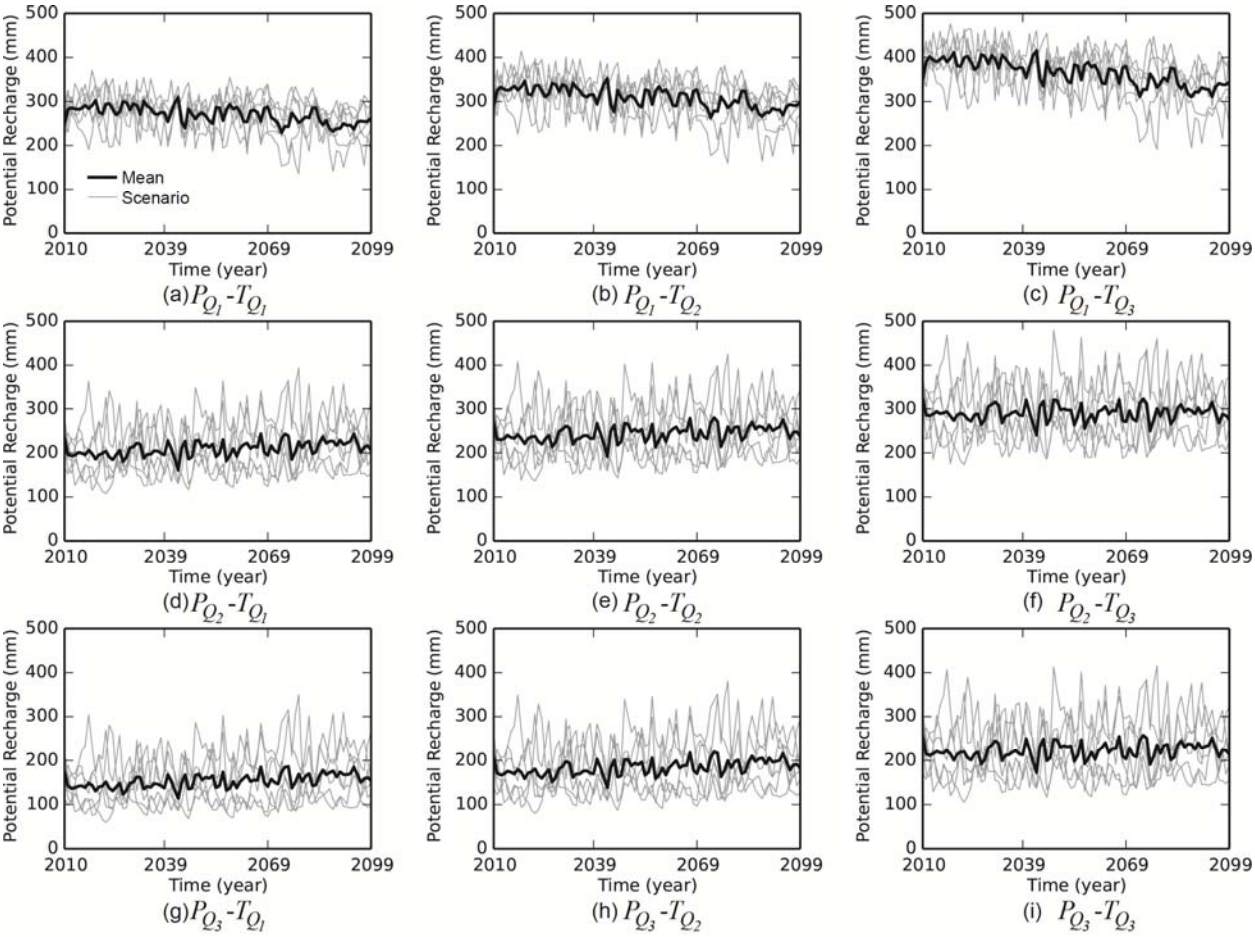

Figure 4.13: Projected annual potential recharge for 2010-2099 for the Southern Hills aquifer system using 25th (Q_1), 50th (Q_2), and 75th (Q_3) percentiles of errors in the projected daily precipitation and temperature. The gray lines represent the six scenarios. The black line represents the average of the six scenarios.

4.3. Conclusions

Assessing the impact of climate change on potential groundwater recharge for humid areas can be achieved by the proposed HELP3 model in a GIS-based water budget framework. Intersecting various datasets through the GIS can easily create a great number of subdivisions, which makes the potential recharge estimation virtually infeasible on a single-core computer. The framework includes parallel programming to divide required HELP3 model runs to multiple cores of a supercomputer to significantly reduce computing time. The parallel programming

allows the methodology to be applied to century-long potential groundwater recharge, surface runoff and evapotranspiration estimation for the area of the Southern Hills aquifer system, southwestern Mississippi and southeastern Louisiana, under a large number of emission scenarios and GCMs.

Under a wide range of climate change scenarios, it was found that the GFDL climate model projects more intense changes in future precipitation, temperature and solar radiation in the study area than the PCM model for the 21st century. Given these projected climate forcings, potential recharge is likely to increase in 2010-2039 and likely to decrease in 2070-2099 with respect to the estimated historical potential recharge (1950-2009). The study area is projected to have a wide range of future potential recharge. The potential recharge is projected to decrease in 2070-2099 by much as 58.1 % (GFDLA1FI) and to increase by as much as 19.1 % (PCMB1 scenario). Runoff is likely to decrease for the 21st century as projected by the GCMs (Table 4.2). PCM projects runoff decrease from -7.0 % to -30.2 % while GFDL projects runoff change from +3.4 % to -27.4 %. The PCM projects evapotranspiration increase from 4.1 % to 6.3 % and the GFDL projects evapotranspiration change from −5.4 % to +4.1 %.

It was found that the future potential recharge variation has strong correlation with the precipitation projections. Potential recharge was found to be most sensitive to the changes in future precipitation, followed by solar radiation, and then temperature. Moreover, both GCMs show a consistent result that the A1FI scenario projects the highest recharge sensitivity to the precipitation, temperature and solar radiation, followed by the A2 scenario, and then the B1 scenario. This order follows the increment of the degree of global warming in the emission scenarios. Subdivisions with high potential recharge show lower recharge sensitivity to precipitation, temperature and solar radiation.

The impact of climate change on groundwater recharge in the study area is unclear as it highly depends on selected climate models and scenarios. Using high-responsive and low-responsive climate models in conjunction with low, medium, and high emission scenarios exhibits a broad extent of uncertain future potential recharge projections. The precipitation and temperature uncertainty analyses show that precipitation influences potential recharge more than temperature. For future study, it would be desirable to repeat the analysis with the latest version of climate models and new emission scenarios, and to include the uncertainty in the hydrologic model.

5. Uncertainty Analysis of Hydrologic Projections under CMIP5 Climate Projections

In this chapter, the hierarchical Bayesian model averaging (HBMA) method is adopted to analyze climate modeling uncertainty and emission scenario uncertainty in projecting future precipitation and temperature, their impacts on future hydrologic projections, and their uncertainty contributions to total uncertainty. This chapter conducts uncertainty analysis on future region-scale hydrologic projections under the uncertain climate change projections of the IPCC Fifth Assessment Report. The aforementioned hierarchical Bayesian model averaging (HBMA) method is adopted to segregate and prioritize sources of climate projection uncertainty, obtain ensemble mean of hydrologic projection, and quantify the hydrologic projection uncertainty arising from individual uncertainty sources (see chapter 2.2). The choices of greenhouse gas (GHG) concentration trajectories, global climate models (GCMs), and GCM initial conditions as three major uncertainty sources in downscaled precipitation and temperature projections. The method is applied to investigate future hydrologic projections in southwestern Mississippi and southeastern Louisiana.

Climate modeling uncertainty includes the use of different GCMs and GCM initial conditions. The emission path uncertainty arises from the assumption of future GHG emissions, atmospheric GHG concentrations and other climate drivers. For the illustration purpose, this study utilizes the precipitation and temperature projections derived by 21 GCMs with different initial conditions and four representative concentration pathways (RCPs) of the Coupled Model Intercomparison Project phase 5 (CMIP5) (Maurer et. al, 2013; USBR 2013). The precipitation and temperature projections are input to a hydrological model, HELP3 (Schroeder et al. 1994), to project future surface runoff, evapotranspiration and potential groundwater recharge of

southwestern Mississippi and southeastern Louisiana. Figure 5.1 shows how hydrologic projection framework incorporated in HBMA to provide mean and variance of projections and to quantify and segregate sources of uncertainties. Also, Figure 5.1 shows the GIS-based water budget framework that creates subdivisions and links the HELP3 model with the CMIP5 climate models and RCP emission paths to predict potential recharge, runoff and evapotranspiration under high performance computing.

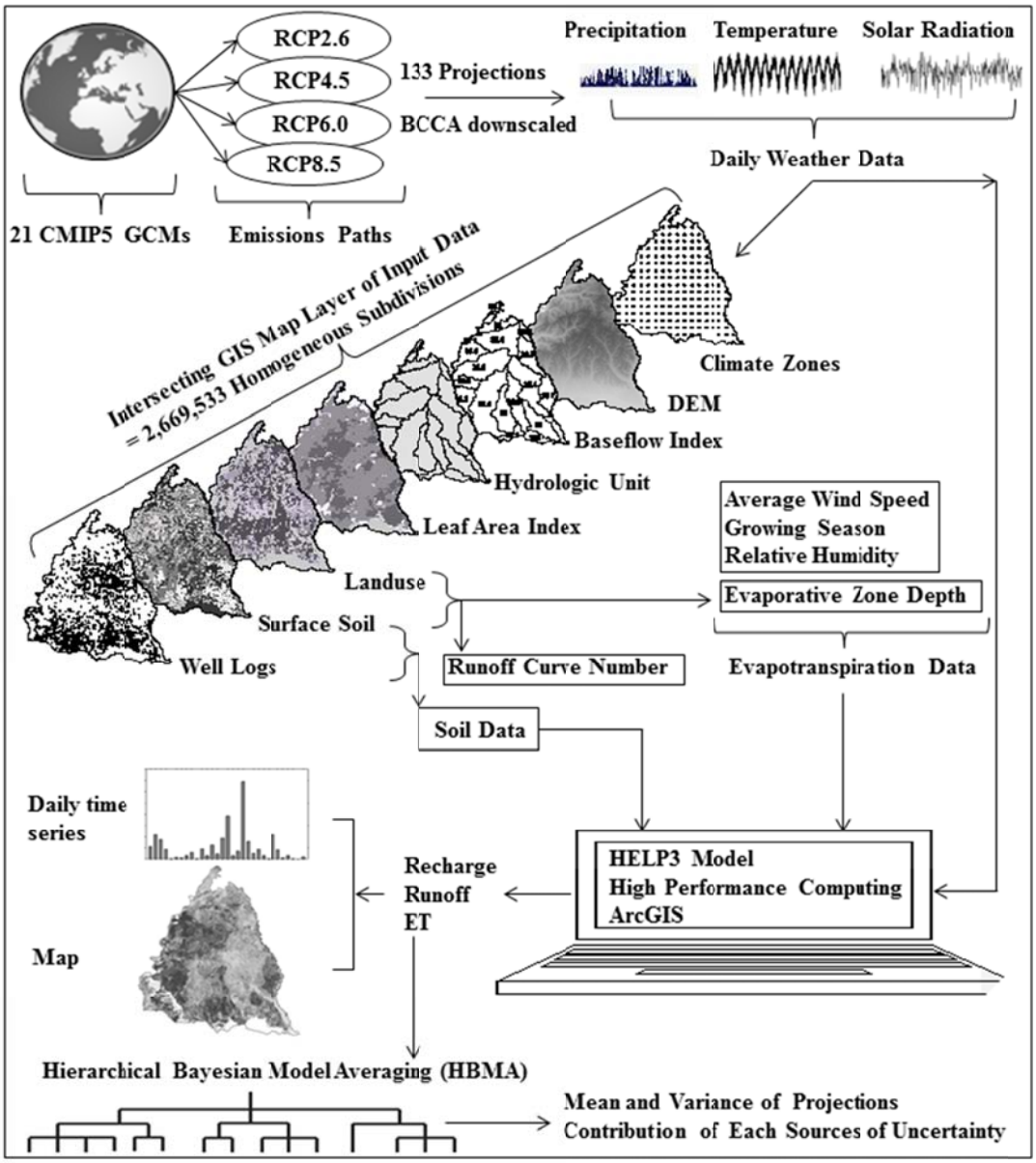

Figure 5.1: Methodology for uncertainty analysis of hydrologic projections under CMIP5 climate projections

Figure 5.2: The study area of southwestern Mississippi (MS) and southeastern Louisiana (LA) bounded by thick black line. Dark gray lines represent the boundaries of 8-digit hydrologic units (HUC8) and light gray lines represent the boundaries of 12-digit hydrologic units (HUC12).

5.1. Hydrologic Study of Southwestern Mississippi and Southeastern Louisiana

This chapter selected southeastern Louisiana and southwestern Mississippi shown in Figure 5.2 as the study area. The area lies between latitude 28.93 to 33.06 degree and longitude from -91.98 to -88.81 degree and covers 79,126 km^2. It includes 28 parishes of Louisiana and 20 counties of Mississippi. The area contains 26 8-digit hydrologic units (HUC8) and 728 12-digit hydrologic units (HUC12). The U.S. Geological Survey (USGS) defined a hierarchical system of hydrologic units in which HUC8 and HUC12 delineates a subbasin and a subwatershed, respectively, with average size of 588 and 33 km^2. The study area encompasses the Southern Hills regional aquifer system (Buono 1983), which was designated as a sole source aquifer by the U.S. Environmental Protection Agency. To obtain high spatial resolution hydrologic predictions, the study area was divided into 2,669,533 subdivisions using GIS by intersecting the vector-based maps of surficial soil type, land use/land cover, leaf area index, topographic slope, lithology, base flow index, HUC8, and climate zones. Each subdivision has homogeneous model parameters for HELP3. The status quo of land use/land cover and soil type is assumed as input to HELP3 for 2010-2099.

5.2. CMIP5 Climate Projections

This study extracts downscaled daily precipitation and temperature data of 21 GCMs from 16 modeling centers and groups listed in Table 5.1 for southwestern Mississippi and southeastern Louisiana. Each GCM may have different initial conditions and may be used for different representative concentration pathways (RCPs). Each climate model for this study is defined as a combination of a GCM and an initial condition. There are 36, 42, 13, and 42 climate models under emission paths RCP2.6, RCP4.5, RCP6.0 and RCP8.5, respectively, which result in 133 climate projections.

The downscaled data are archived in the website of the Downscaled CMIP3 and CMIP5 Climate and Hydrology Projections (Maurer et. al, 2007; Maurer et. al, 2013; USBR, 2013). The 21 GCMs are from the Coupled Model Intercomparison Project phase 5 (CMIP5), developed by the World Climate Research Programme (WCRP), and have been considered in the IPCC Fifth Assessment Report (AR5). The GCM outputs were downscaled to 1/8° spatial resolution using Bias Corrected Constructed Analogs (BCCA) method. The archive integrates the state-of-the-art climate models and the most recent emission scenarios (Rogelj et el., 2012). The CMIP5 contains greater spatial resolution models, enhanced model physics, and a richer set of output fields compared to CMIP3 (Taylor et al., 2012). The CMIP5 projects a broader range of potential increases in global average temperature comparing to the CMIP3.

This CMIP5 multi-model ensemble dataset is driven by the four representative concentration pathways (RCPs) of atmospheric GHG concentrations and other climate drivers. The four RCPs, RCP2.6, RCP4.5, RCP6.0 and RCP8.5, simulate global mean radiant forcing 2.6, 4.5, 6.0 and 8.5 W/m^2, respectively. The global annual GHG emissions of RCP2.6, RCP4.5 and RCP6.0 are assumed to peak around 2020, 2040, 2080, respectively, and then decline substantially. RCP8.5 assumes emissions continue to increase throughout the 21st century (Van Vuuren et al., 2011). In other words, RCP2.6, RCP4.5, RCP6.0 and RCP8.5 represent the lowest, lower, midrange and the highest emission paths, respectively. RCP2.6 considers strong mitigation, the lowest GHG concentration, and the least warming (0.3-1.7 °C) and represents the most optimistic scenario, while RCP8.5 considers no mitigation, the highest GHG concentration, and the greatest warming (2.6-4.8 °C) across the 21st century and portrays the most pessimistic scenario (Meinshausen et al., 2011).

Table 5.1: Modeling centers/groups providing downscaled data of 21 GCMs and their corresponding initial conditions (IC) under each representative concentration pathway (RCP) used in this study (Maurer et. al, 2013; USBR, 2013).

No.	Modeling Center/Group	GCM	No. of IC			
			RCP 2.6	RCP 4.5	RCP 6.0	RCP 8.5
1	Commonwealth Scientific and Industrial Research Organization (CSIRO) and Bureau of Meteorology (BOM), Australia	ACCESS1.0	0	1	0	1
2	Beijing Climate Center, China Meteorological Administration, China	BCC-CSM1.1	1	1	0	1
3	College of Global Change and Earth System Science, Beijing Normal University, China	BNU-ESM	0	1	0	1
4	Canadian Centre for Climate Modelling and Analysis, Canada	CanESM2	5	5	0	5
5	National Center for Atmospheric Research, USA	CCSM4	2	2	2	2
6	Community Earth System Model Contributors, USA	CESM1(BGC)	0	1	0	1
7	Centre National de Recherches Météorologiques / Centre Européen de Recherche et Formation Avancée en Calcul Scientifique, France	CNRM-CM5	0	1	0	1
8	Commonwealth Scientific and Industrial Research Organization in collaboration with Queensland Climate Change Centre of Excellence, Australia	CSIRO-Mk3.6.0	10	10	0	10
9	NOAA Geophysical Fluid Dynamics Laboratory, USA	GFDL-CM3 GFDL-ESM2G GFDL-ESM2M	1 1 1	0 1 1	1 1 1	1 1 1
10	Institute for Numerical Mathematics, Russia	INM-CM4	0	1	0	1
11	Institut Pierre-Simon Laplace, France	IPSL-CM5A-LR IPSL-CM5A-MR	3 1	4 1	1 1	4 1
12	Japan Agency for Marine-Earth Science and Technology, Atmosphere and Ocean Research Institute (The University of Tokyo), and National Institute for Environmental Studies, Japan	MIROC-ESM MIROC-ESM-CHEM	1 1	1 1	1 1	1 1
13	Atmosphere and Ocean Research Institute (The University of Tokyo), National Institute for Environmental Studies, and Japan Agency for Marine-Earth Science and Technology	MIROC5	3	3	1	3
14	Max-Planck-Institut für Meteorologie (Max Planck Institute for Meteorology), Germany	MPI-ESM-MR MPI-ESM-LR	1 3	3 3	0 0	1 3
15	Meteorological Research Institute, Japan	MRI-CGCM3	1	1	1	1
16	Norwegian Climate Centre, Norway	NorESM1-M	1	1	1	1

For each RCP, a rich dataset of information regarding emissions, concentrations and associated land use change scenarios has been generated based on simulations from a set of integrated assessment models (IAMs). The emission scenarios from the IPCC Special Report on

Emission Scenarios (SRES) assumed that there were no policy actions to mitigate climate change (Nakicenovic et al., 2000). In contrast to the SRES scenarios, the newly developed RCPs provide comprehensive and more detailed information needed for climate modeling, climate change mitigation analysis and impact assessment of different climate policies. Moreover, the RCPs include a wider range of future conditions and emissions scenarios than the SRES scenarios. The RCPs are consistent with a wide range of possible changes in future anthropogenic GHG emissions (Moss et al., 2010). Thus, combinations of CMIP5 and RCPs cover a full range of future possible climate change projections.

As shown in Table 5.1, the Downscaled CMIP3 and CMIP5 Climate and Hydrology Projections intuitively reveal the sources of uncertainty for precipitation and temperature projections from the choices of the emission path, the GCM, and the GCM initial condition. The propositions for the choice of the emission path are RCP2.6, RCP4.5, RCP6.0 and RCP8.5. The proposition for the choice of the GCM is the 21 GCM. The propositions for the choice of the GCM initial condition varies from 1 to 10.

5.3. Posterior Model Probabilities of Climate Models

5.3.1. Historical Climate Simulations

This study uses monthly precipitation and temperature data from 1950 to 2006 to calculate posterior model probabilities for the climate models listed in Table 5.1. The historical monthly precipitation and temperate data were obtained from Maurer et al. (2002) and Maurer (2013). Historical simulations of precipitation and temperature given a GCM and an initial condition are identical for different emission paths. Therefore, among the 133 climate models, 44 climate models have different historical simulations. The study assumed that the 44 climate models are equally important before their output were compared to historical monthly

precipitation and temperature data from 1950-2006. The statistically daily downscaled data may not be reliable for comparison, but monthly or yearly intermodal comparison are reasonable. The daily temperature and precipitation observations are obtained from the National Oceanic and Atmospheric Administration (NOAA) Cooperative Observer (COOP) stations and gridded to 12 km spatial resolution. Daily values then aggregated to provide monthly averages of precipitation and temperature.

By adopting the Bayesian information criterion (BIC), the variance window and equal prior model probabilities (Tsai and Li 2008a), the posterior model probabilities of the climate models are approximated as follows

$$\Pr\left(\mathbf{M}_p^{(m)} \mid \mathbf{D}\right) \approx \frac{\exp\left(-\frac{1}{2}\alpha \Delta \mathrm{BIC}_p^{(m)}\right)}{\sum_q \exp\left(-\frac{1}{2}\alpha \Delta \mathrm{BIC}_p^{(q)}\right)} \tag{23}$$

where $\Delta \mathrm{BIC}_p^{(m)} = \mathrm{BIC}_p^{(m)} - \mathrm{BIC}_{\min}$ and α is the scaling factor that defines the size of the variance window. $\mathrm{BIC}_p^{(m)}$ is the BIC value of climate model $\mathbf{M}_p^{(m)}$ and $\mathrm{BIC}_{\min}$ is the minimum BIC value among the climate models. The BIC can be written as

$$\mathrm{BIC}_p^{(m)} = \sum_i \frac{(P_{p,i}^{(m)} - P_i^{obs})^2}{\sigma_{P,i}^2} + \sum_j \frac{(T_{p,j}^{(m)} - T_j^{obs})^2}{\sigma_{T,j}^2} + N \ln 2\pi + k_p^{(m)} \ln(N) \tag{24}$$

where $P_p^{(m)}$ and $T_p^{(m)}$ are the simulated monthly precipitation and temperature, respectively, by climate model $\mathbf{M}_p^{(m)}$. P^{obs} and T^{obs} are the observed monthly precipitation and temperature data, respectively. σ_P^2 and σ_T^2 are the error variances of precipitation and temperature. N is the number of observed data, and $k_p^{(m)}$ is the number of unknown model parameters that are estimated during model calibration. The first two terms in the right-hand side of Eq. (24) are the weighted fitting residuals. The term $N \ln 2\pi + k_p^{(m)} \ln(N)$ represents the complexity of climate

model $\mathbf{M}_p^{(m)}$. Due to the lack of information on the complexity term in Eq. (24), this study assumed equal model complexity.

Table 5.2: Posterior model probabilities of 22 models. Posterior model probabilities less than 1.5 % are not shown.

Number	Climate Model	$\sum_i \frac{(P_{p,i}^{(m)} - P_i^{obs})^2}{\sigma_{P,i}^2}$	$\sum_j \frac{(T_{p,j}^{(m)} - T_j^{obs})^2}{\sigma_{T,j}^2}$	$\Delta\text{BIC}_p^{(m)}$	$\Pr\left(\mathbf{M}_p^{(m)} \mid \mathbf{D}\right)$
1	ipsl-cm5a-lr.4	578.7	219.1	0.0	10.8 %
2	cnrm-cm5.1	572.5	249.7	24.4	9.1 %
3	gfdl-esm2g.1	545.1	308.6	56.0	7.3 %
4	csiro-mk3-6-0.10	573.7	294.1	70.1	6.6 %
5	miroc-esm-chem.1	569.7	322.5	94.5	5.6 %
6	csiro-mk3-6-0.1	643.9	253.0	99.2	5.4 %
7	canesm2.5	607.7	321.0	131.0	4.3 %
8	canesm2.3	670.0	269.0	141.2	4.0 %
9	csiro-mk3-6-0.6	691.0	254.6	147.9	3.9 %
10	ipsl-cm5a-lr.2	653.5	300.2	155.9	3.6 %
11	miroc5.1	566.7	387.0	155.9	3.6 %
12	miroc5.2	484.6	477.1	164.0	3.4 %
13	ipsl-cm5a-mr.1	626.5	351.9	180.6	3.1 %
14	bcc-csm1-1.1	542.7	439.9	184.8	3.0 %
15	gfdl-esm2m.1	586.6	404.7	193.6	2.8 %
16	inmcm4.1	730.0	273.7	206.0	2.6 %
17	csiro-mk3-6-0.2	651.8	353.4	207.4	2.5 %
18	gfdl-cm3.1	527.4	491.2	220.8	2.3 %
19	miroc5.3	581.3	447.9	231.5	2.2 %
20	csiro-mk3-6-0.8	618.7	414.6	235.6	2.1 %
21	mri-cgcm3.1	423.4	645.2	270.9	1.6 %
22	access1-0.1	643.2	428.4	273.9	1.6 %

A large window size, $\alpha = 1.06/\sqrt{N}$ (Tsai and Li 2008a), is considered in Eq. (23), to intentionally accept more climate models in this study. Table 5.2 lists the weighted fitting residuals and the ΔBIC values and ranks the top 22 climate models by the posterior model probability higher than 1.5%. If Occam's window were used, there would be only 1 climate model left with posterior model probability 100%. The climate model, ipsl-cm5a-lr.4 (GCM ipsl-cm5a-lr with initial condition 4) has the highest posterior model probability 10.8%, followed by the climate model cnrm-cm5.1 with posterior model probability 9.1%, and the climate model

csiro-mk3-6-0.10 with posterior model probability 7.3%. For the historical climate period, Table 5.1 shows two sources of uncertainty, the choices of the GCM and the GCM initial condition.

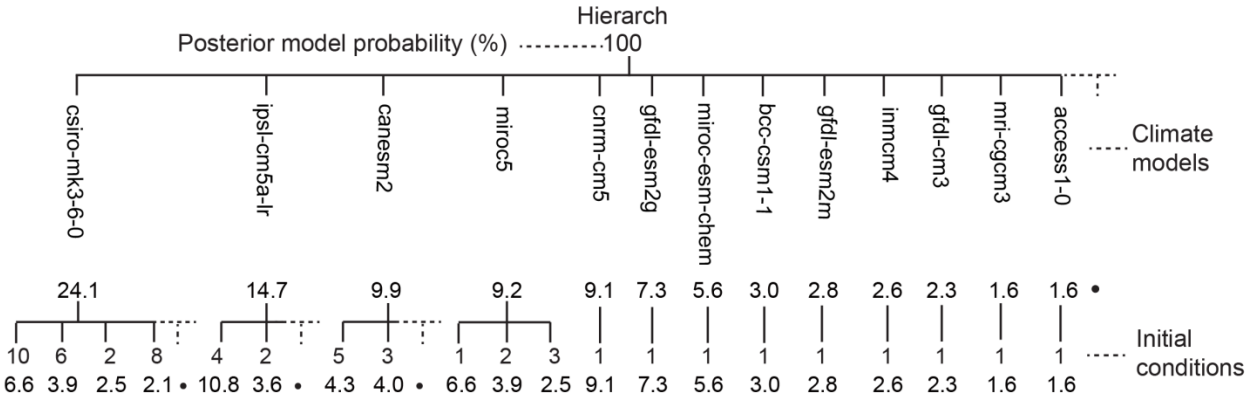

Figure 5.3: BMA tree of posterior model probability. The first level considers different climate models. The second level considers different initial conditions given a climate model. Climate models at the base level that have posterior model probability less than 1.5 % are not shown.

The BMA tree of posterior model probabilities of the GCMs and their corresponding initial conditions in a hierarchical order is shown in Figure 5.3. There are 44 climate models at the base level (or the 2nd level in this figure) and 21 climate models at the 1st level that their outputs consider all corresponding initial conditions under them through Bayesian model averaging. The best, the 2nd best and the 3rd best climate models at the 1st level is csiro-mk3-6-0, ipsl-cm5a-lr, and canesm2 with posterior model probability 24.1%, 14.7% and 9.9%, respectively. The best climate model at the 2nd level might not be the best climate model at the 1st level due to posterior model probabilities and different number of initial conditions under each GCM.

5.3.2. Future Climate Projections

Since there are different numbers of climate models under each emission path (see Table 5.1), posterior model probabilities and conditional posterior model probabilities of the climate

models under individual emission paths are calculated and shown in the BMA trees in Figure 5.4. The GCM, csiro-mk3-6-0 is the best model under the given emission paths, except for RCP6.0 which does not consider this GCM. Other GCMs shown in Figure 5.4 are generally good models although their ranks may vary for different emission paths.

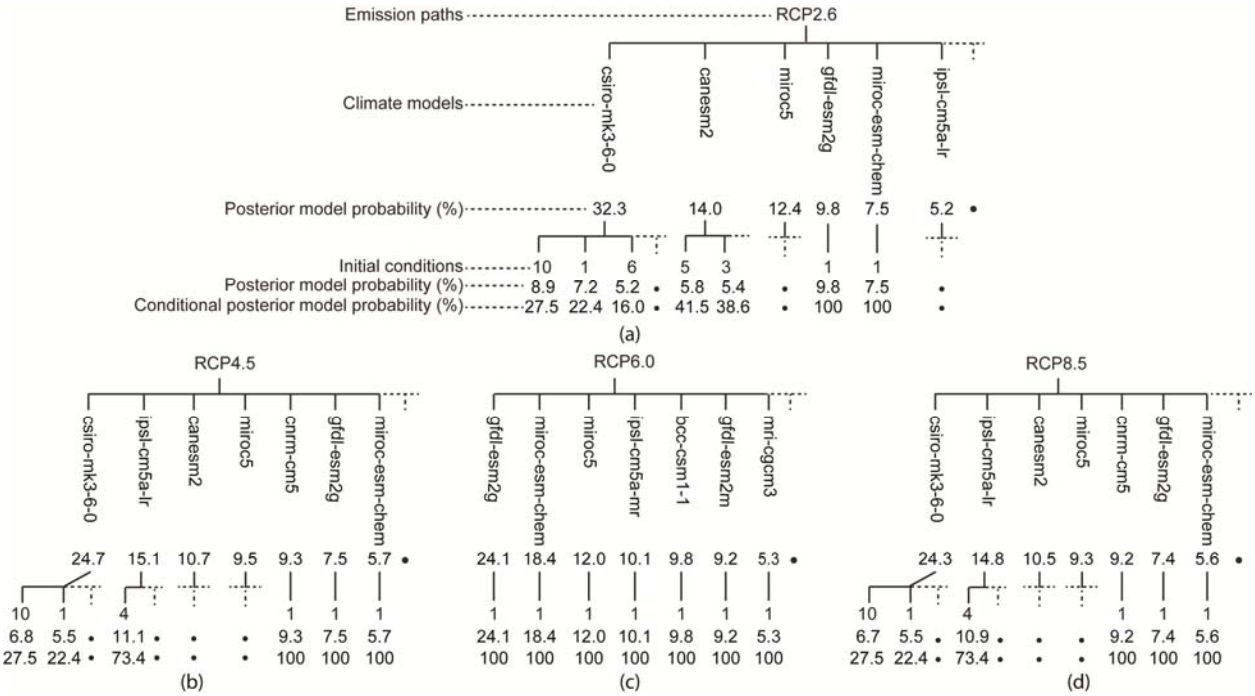

Figure 5.4: BMA trees of posterior model probability and conditional posterior model probability for different emission paths. Climate models at the base level that have posterior model probability less than 5 % are not shown.

By integrating all 133 climate models for climate projections through the HBMA, this study develops a BMA tree of the posterior model probabilities shown in Figure 5.5 based on Figure 2.1 and Figure 5.4 to take into account the three sources of uncertainty in a hierarchical order for climate projections. The 1st level of uncertainty is the uncertain future emission path, under which, the 2nd level of uncertainty is the GCM. The 3rd level of uncertainty is the initial condition. The posterior model probabilities at the 1st level were calculated by rescaling the sums of probabilities of climate models in Table 5.2 or Figure 5.3 under individual emission paths. For the study area, climate projections under emission paths RCP4.5 and RCP8.5 are equally

important (32.4% and 32.8%, respectively), followed by RCP2.6 and RCP6.0. The importance of emission paths for climate projections is the reflection of the number of climate models considered in individual emission paths.

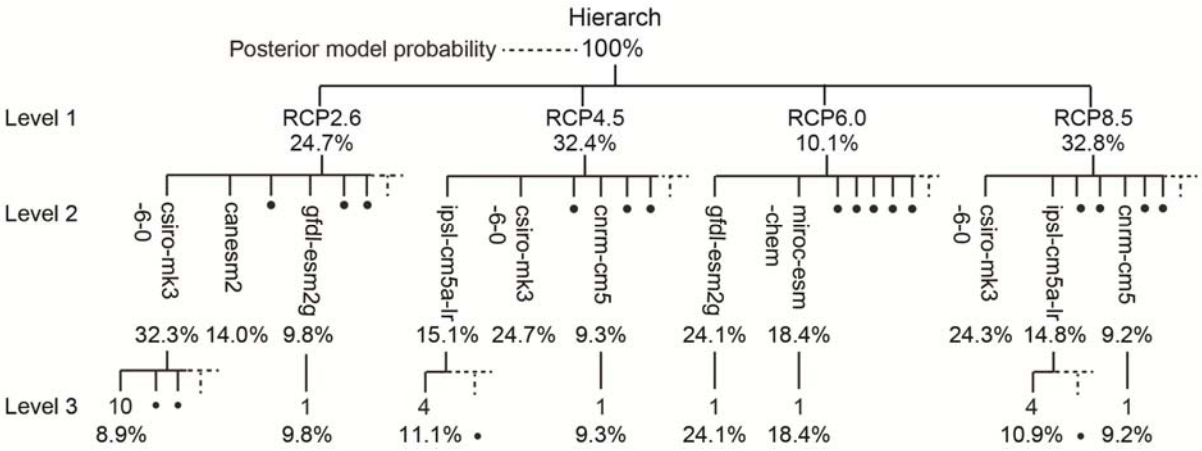

Figure 5.5: BMA tree of posterior model probability for climate model projections. Level 2 and level 3 show the best and the second best models.

5.4. CMIP5 Precipitation and Temperature Projections

5.4.1. Future CMIP5 Projections

The cumulative changes in precipitation and changes in temperature for individual emission path under corresponding climate models (Table 5.1) with respect to the historical baseline (1950-2009) are shown in Figure 5.6 and Figure 5.7, respectively. The mean annual precipitation and temperature in 1950-2009 are respectively 1522.1 mm and 18.9 °C for the area of southeastern Louisiana and southwestern Mississippi. To calculate the changes for the study area, the area-averaged values of the climate variables of all subdivisions were calculated and subtracted from the mean annual for 1950-2009. Sums of the changes over years show the cumulative changes. If changes the climate variables are negative over time, their cumulative changes will amplify this phenomenon by showing large negative values and vice versa. For example, a fall of almost 22 m cumulative change in 2099 for the lowest precipitation projection

under RCP85 (Figure 5.6(d)), shows that the yearly precipitation continuously decreases from 2040 to 2099 with respect to the baseline precipitation. Conversely, an increase of almost 19 m cumulative change in 2099 for highest precipitation projection under RCP26 (Figure 5.6(a)), shows that the yearly precipitation continuously increase from 2040 to 2099 with respect to the baseline precipitation. Precipitation projected to increase slightly under all emission paths for 2010-2039. All emission paths show diverse precipitation projections for 2040-2099. As shown in Figure 5.7, all emission paths project increasing trend in temperature for 2010-2099, which the differences between projections become evident after 2050. Similar to CMIP3 climate projections in chapter 4 (Figure 4.6), the differences of the cumulative changes between the emission paths grows continuously over time. After the mid-century, the cumulative changes of precipitation and the changes of temperature between emission paths are distinguishable, which are consistent with the global projections (Cubasch et al. 2001). Moreover, the projections of the climate models under individual emission path for the study area start to diverge significantly after the mid-century. This is the point at which substantial differences between the projections by climate models begin. These differences results from the differences among climate models parameterizations, sensitivities and responses to greenhouse gases and other forcings (Cayan et al. 2007).

Table 5.3: Projected changes in mean annual precipitation and temperature of individual emission path (based on simple averaging) under their corresponding climate models with respect to the mean annual for 1950-2009.

Emission path	Number of climate models	Precipitation (%) Mean annual =1522.1 mm			Temperature (ºC/year) Mean annual =18.9 ºC		
		2010-2039	2040-2069	2070-2099	2010-2039	2040-2069	2070-2099
RCP26	36	+1.44	+3.23	+3.90	+0.048	+0.063	+0.061
RCP45	42	+0.95	+1.28	+2.18	+0.048	+0.076	+0.089
RCP60	13	+1.02	−0.10	−2.12	+0.042	+0.066	+0.099
RCP85	42	+0.88	+0.24	−2.54	+0.051	+0.098	+0.157

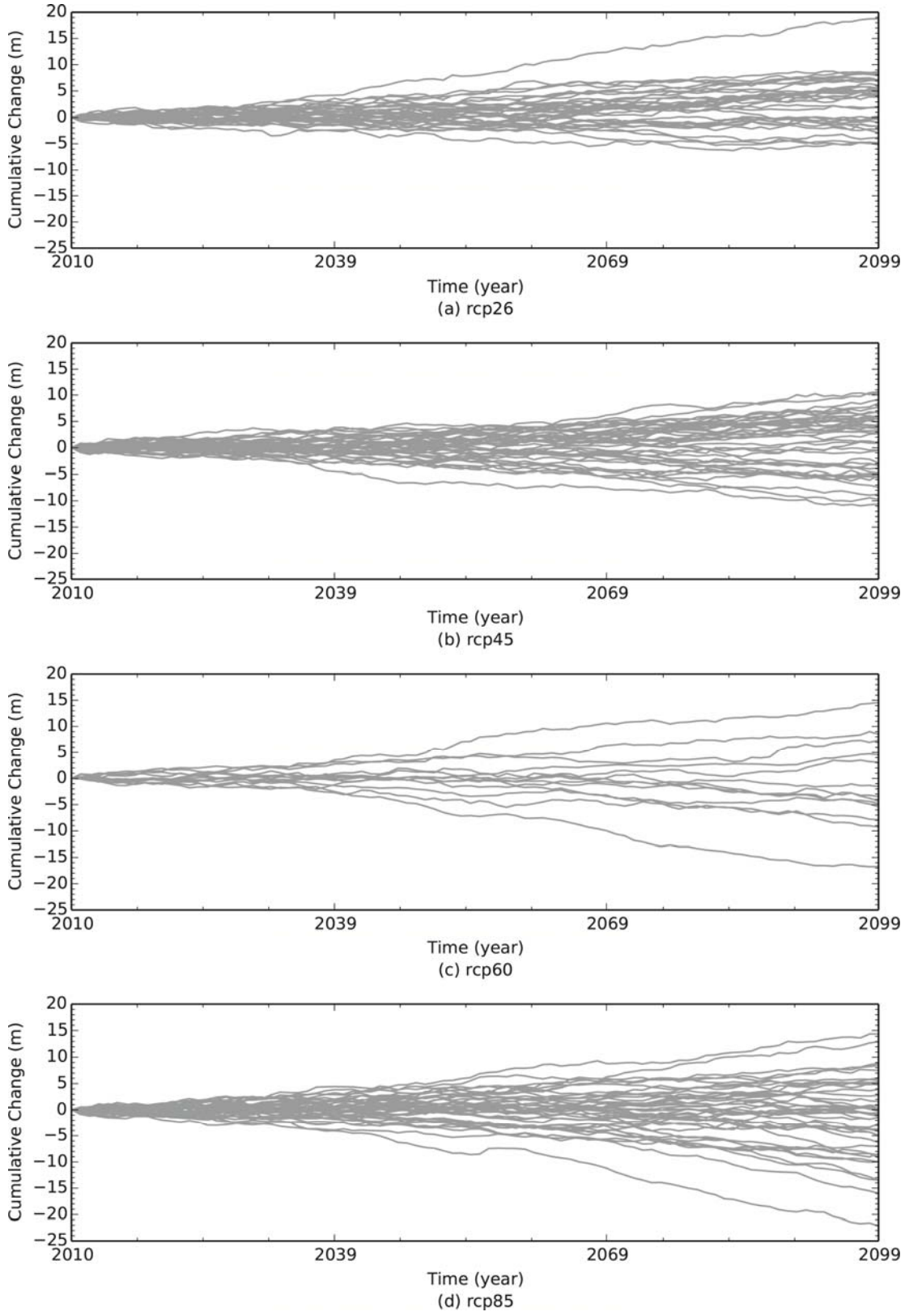

Figure 5.6: Cumulative changes of precipitation for individual emission path under climate models in Table 5.1 with respect to the historical baseline.

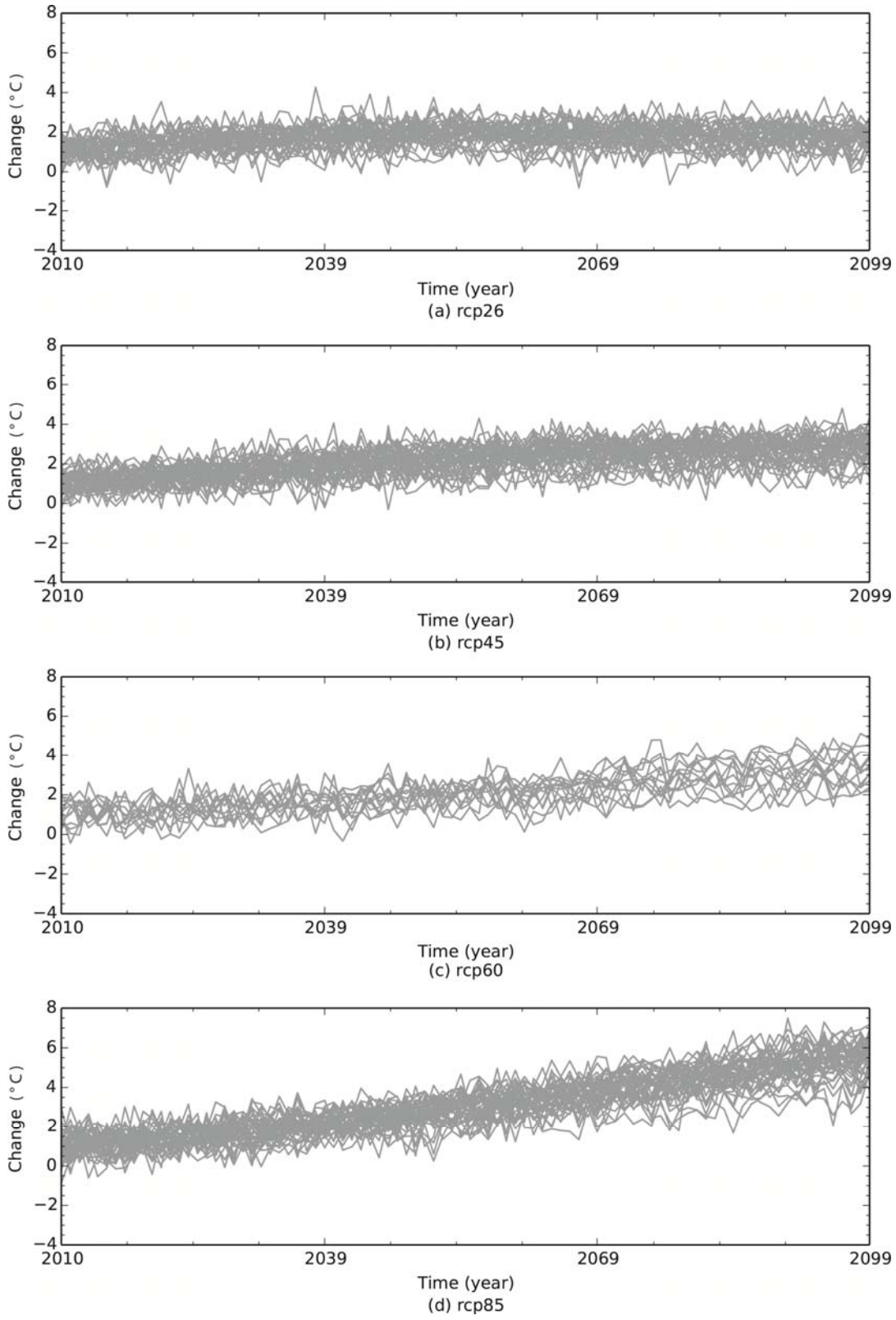

Figure 5.7: Changes of temperature for individual emission path under climate models in Table 5.1 with respect to the historical baseline.

Table 5.3 shows the projected changes in mean annual precipitation and temperature of individual emission path based on simple averaging of their corresponding climate models with respect to the mean annual for 1950-2009. The simple average of all climate models under each emission path is used in Table 5.3, and then subtracted from the mean annual for 1950-2009. The RCP26 and RCP45 project overall precipitation increase (+3.90 % and +2.18 %, respectively,) while RCP60 and RCP85 project decrease of precipitation (−2.12 % and −2.54 %, respectively,) for 2070-2099. The RCP26, which is the most optimistic emission path, projects slight increase in temperature, and highest precipitation. On the other hand, the RCP85, which is the most pessimistic emission path, projects largest temperature increase and lowest precipitation toward the end of the 21st century. The order of increasing temperature in emission paths under climate models compared to historical baseline is as follows: RCP26, RCP45, RCP60 and RCP85, which respectively projects increase of 1.83 °C, 2.68 °C, 2.97 °C and 4.7 °C in 2070-2099 for the study area. This order follows the increment of the degree of global warming in the emission paths.

5.4.2. HBMA Analysis of CMIP5 Precipitation and Temperature Projections

In order to improve precipitation and temperature projections for the study area, the hierarchical Bayesian model averaging (HBMA) method is implemented to quantify means and variances of precipitation and temperature projections. Instead of simple averaging, the posterior model probabilities (defined in section 5.3.2) is assigned to climate models to enhance the effect of climate models with greater performance in terms of simulating monthly precipitation and temperature from 1950-2009. Precipitation and temperature projections of southwestern Mississippi and southeastern Louisiana for 2010-2099 using the best and second best climate models at level 3 for four emission paths are shown in Figure 5.8. Projected precipitation shows

much larger variability compared to temperature projections. Different climate models projects quite different precipitation. However, precipitation is likely to increases under RCP26 and decreases under RCP85. RCP26 projects lowest increase in temperature while RCP85 projects largest temperature increase regardless of climate models.

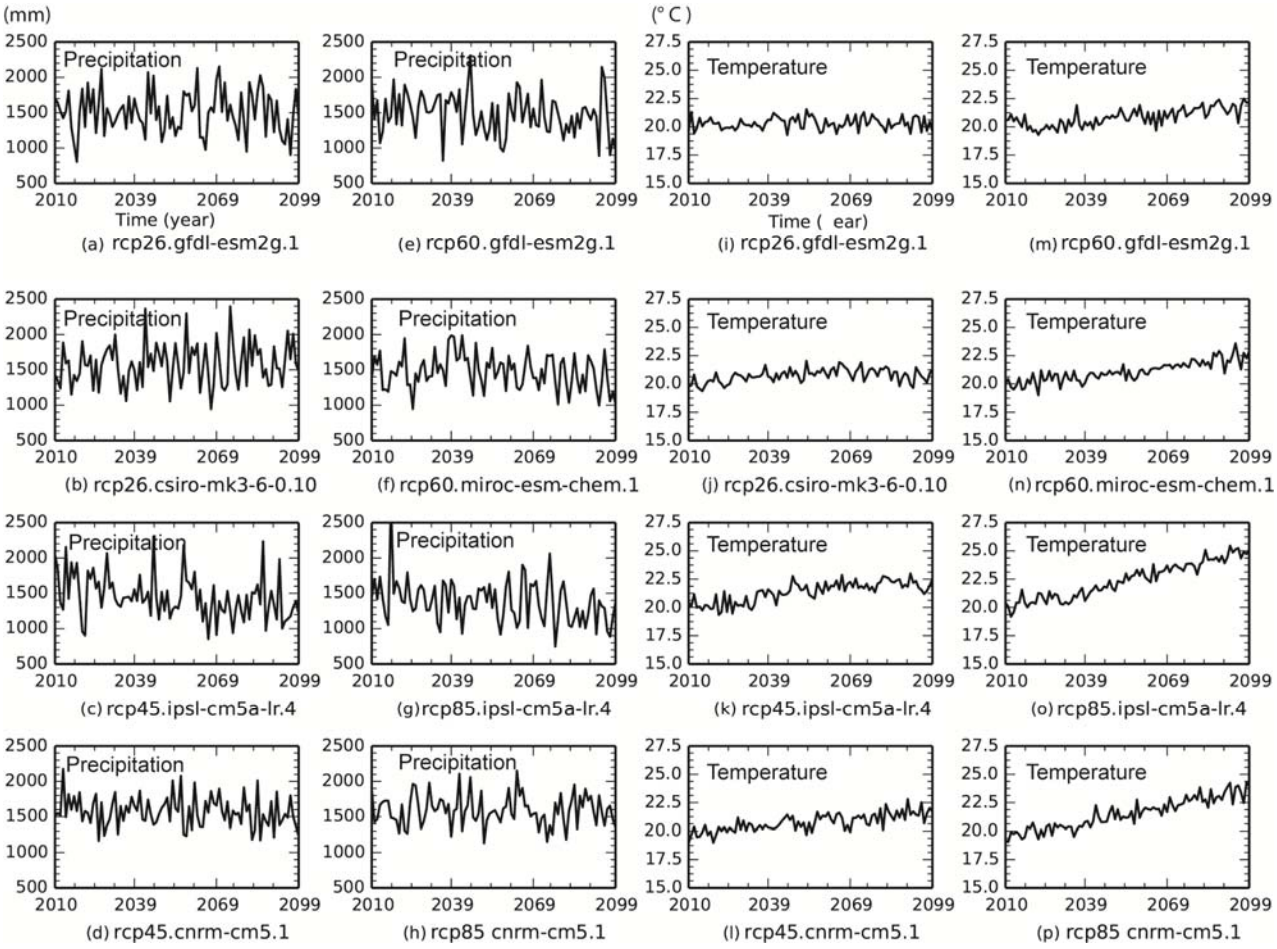

Figure 5.8: Precipitation and temperature projections for 2010-2099 using the best and the second best climate models at level 3.

Using BMA at level 2, the mean projection and uncertainty of precipitation and temperature due to uncertain GCM initial conditions are shown in Figure 5.9. The csiro-mk3.6.0, ipsl-cm5a-lr, and canesm2 show higher projection uncertainty due to including many initial conditions. The csiro-mk3-6-0 model uses largest number of initial conditions, which results in

higher uncertain projections than other GCMs. Projected precipitation shows higher uncertainty than projected temperature.

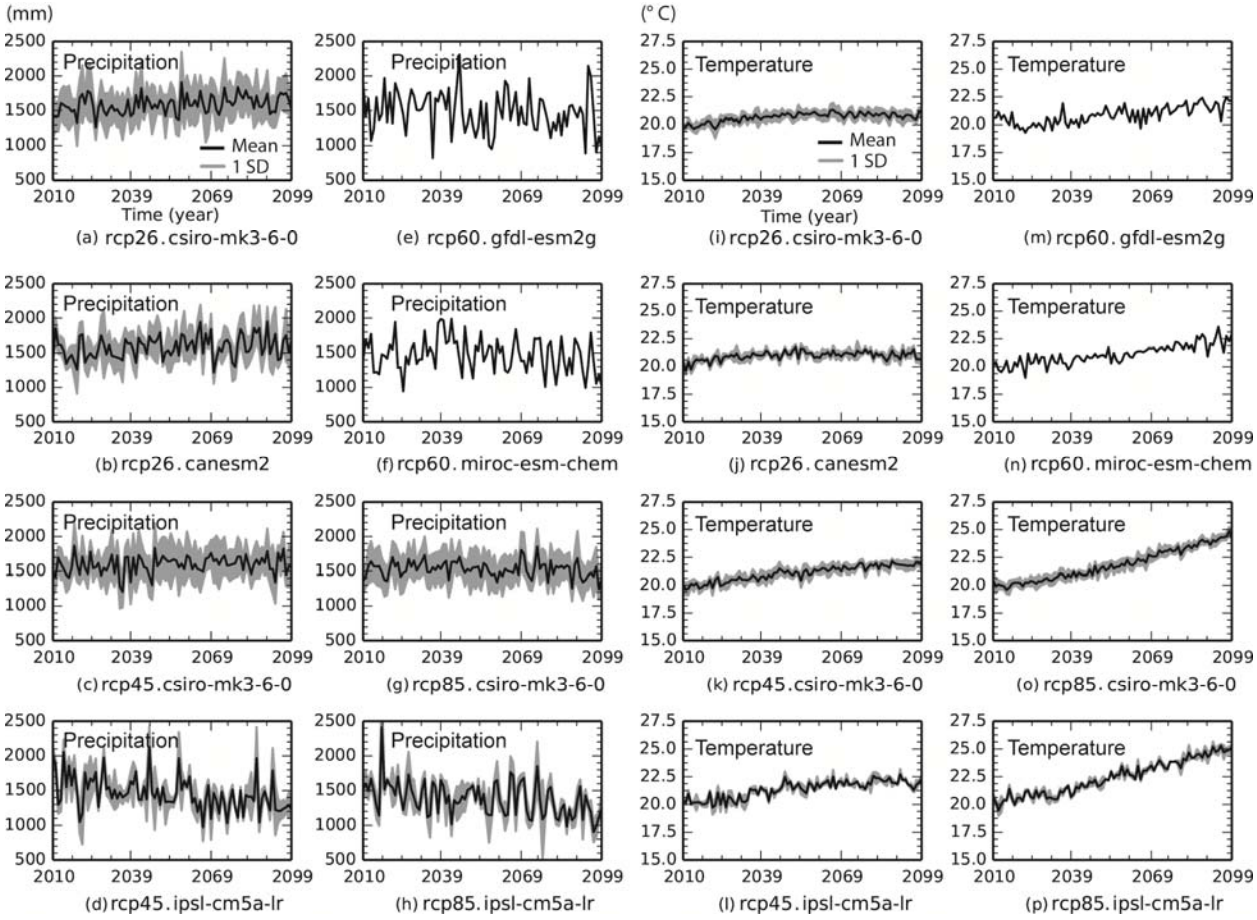

Figure 5.9: BMA mean and one standard deviation (SD) interval for precipitation and temperature projections for 2010-2099 using the best and the second best GCMs at level 2.

Likewise, using BMA at level 1, the mean projection and uncertainty of precipitation and temperature due to uncertain GCMs and GCM initial conditions are shown in Figure 5.10. Potential recharge projection shows the higher uncertainty than temperature projection. For precipitation and temperature projection, RCP2.6 projects an increasing trend, RCP4.5 shows a constant trend, and RCP6.0 shows a slightly decreasing trend, and RCP8.5 shows a decreasing trend.

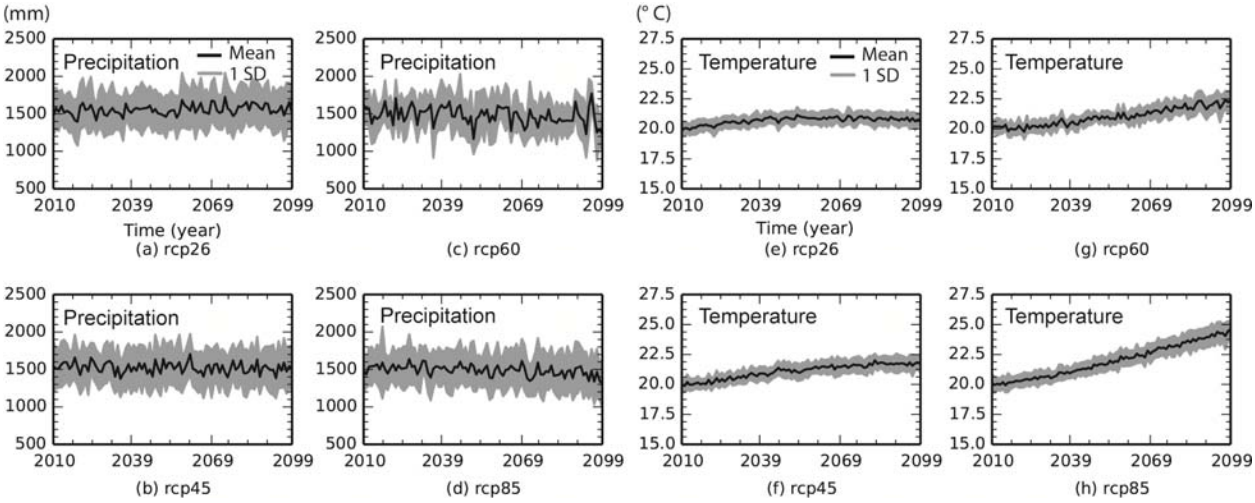

Figure 5.10: BMA mean and one standard deviation (SD) interval of for precipitation and temperature projections for 2010-2099 using all climate models under corresponding emission paths at level 1

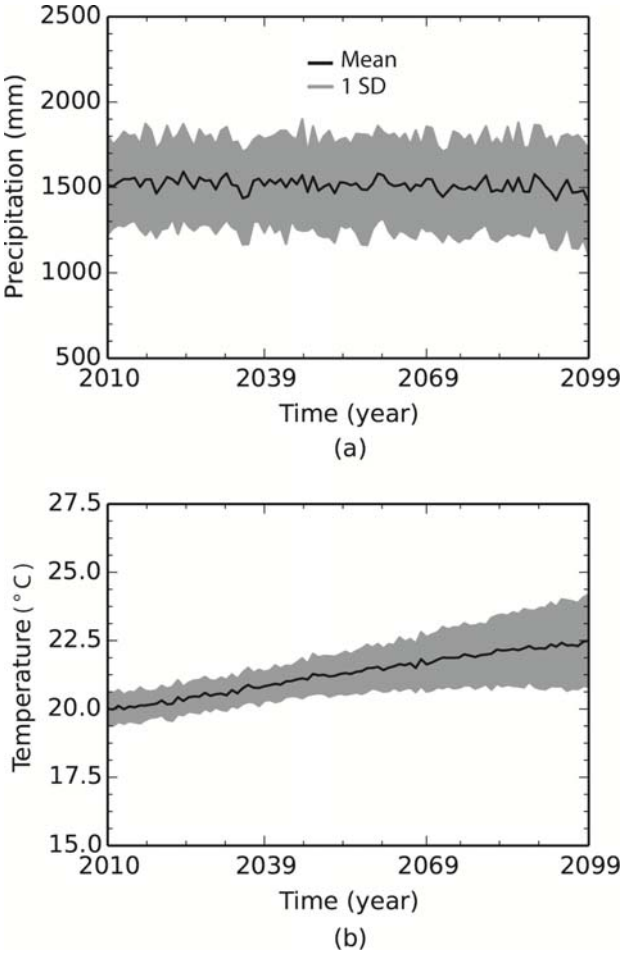

Figure 5.11: BMA mean and one standard deviation (SD) interval of precipitation and temperature projections for 2010-2099 at the hierarch level using 133 climate models.

The BMA mean and one standard deviation interval of annual precipitation and temperature predictions from 2010 to 2099 for the study area using the entire 133 climate projections is shown in Figure 5.11. The predictions are the results of the hierarch model in Figure 5.5, which take into account uncertainties arising from different GCMs, GCM initial conditions, and emission paths. As shown in Figure 5.11, the projected mean precipitation indicates a slightly decreasing trend while the projected mean temperature indicate increasing trends throughout 2099. Precipitation projections show higher uncertainty than temperature projections. The projection uncertainty in precipitation shows a constant trend while uncertainty in temperature projection grows continuously after midcentury through the end of the 21 century.

Table 5.4 shows projection anomalies in mean annual precipitation and temperature for three 30-year periods (2010-2039, 2040-2069, and 2070-2099) with respect to mean annuals of 1950-2009 at different levels of the BAM tree in Figure 5.5. Projection anomalies using the best and the second best climate models under each emission path (level 3 of Table 5.4) show that precipitation has diverse projections with no clear trend. The rcp26.csiro-mk3-6-0.10 model projects highest precipitation increase (+5.8 %) while rcp85.ipsl-cm5a-lr.4 model projects highest precipitation decrease (−16.7 %) in 2070-2099. Temperature is projected to increase continuously for 2010-2099 under all climate models. Similar to projection anomalies at level 3, climate models at level 2 produce wide range of precipitation projections. Projection anomalies at level 1 follow the degree of global warming in the development of future emissions. RCP2.6 is optimistic for precipitation and projects continuous precipitation increase for the next century due to the assumption of strong mitigation, the lowest GHG concentration, and the least warming. RCP4.5 also shows positive for precipitation, but with a decreasing trend over time. RCP6.0 and RCP8.5 project precipitation decrease in 2040-2099. Again, RCP8.5 shows most

pessimistic emission path with the least precipitation increase and the highest temperature increase. Conversely, RCP2.6 demonstrates the most optimistic emission path due to projecting highest precipitation increase and the least temperature increase. Using all 133 climate models, the BMA mean precipitation in southwestern Mississippi and southeastern Louisiana is projected to decrease from 1522.1 mm to 1496.1 mm for the next century. Temperature is projected to increase from 18.9 ºC to 22.1 ºC through the end of the next century.

Table 5.4: Projected changes in mean annual precipitation and temperature with respect to mean annuals of 1950-2009. Level 3 lists the best and the second best climate models under each emission path. Level 2 lists the best and the second best GCMs under each emission path.

Level	Climate model	Precipitation (%) Mean annual = 1522.1 mm			Temperature (ºC/year) Mean annual = 18.9 ºC		
		2010-2039	2040-2069	2070-2099	2010-2039	2040-2069	2070-2099
3	rcp26.gfdl-esm2g.1	−1.0	−1.6	−0.8	+0.042	+0.050	+0.048
	rcp26.csiro-mk3-6-0.10	−0.3	+5.1	+5.8	+0.048	+0.068	+0.064
	rcp45.ipsl-cm5a-lr.4	+3.2	−5.7	−12.2	+0.049	+0.090	+0.104
	rcp45.cnrm-cm5.1	+4.8	+4.9	+0.3	+0.039	+0.062	+0.083
	rcp60.gfdl-esm2g.1	+2.5	−2.8	−7.6	+0.043	+0.062	+0.088
	rcp60.miroc-esm-chem.1	−2.1	+0.8	−8.9	+0.045	+0.069	+0.104
	rcp85.ipsl-cm5a-lr.4	−2.6	−8.7	−16.7	+0.056	+0.116	+0.175
	rcp85.cnrm-cm5.1	+5.0	+6.9	+2.0	+0.037	+0.085	+0.136
2	rcp26.csiro-mk3-6-0	+0.5	+5.0	+7.6	+0.044	+0.065	+0.064
	rcp26.canesm2	+0.1	+6.7	+5.1	+0.059	+0.074	+0.072
	rcp45.csiro-mk3-6-0	+1.9	+5.9	+6.5	+0.045	+0.075	+0.094
	rcp45.ipsl-cm5a-lr	+3.1	−4.1	−12.0	+0.052	+0.089	+0.102
	rcp60.gfdl-esm2g	+2.5	−2.8	−7.6	+0.043	+0.062	+0.088
	rcp60.miroc-esm-chem	−2.1	+0.8	−8.9	+0.045	+0.069	+0.104
	rcp85.csiro-mk3-6-0	+1.4	+1.0	−0.9	+0.047	+0.090	+0.155
	rcp85.ipsl-cm5a-lr	−2.1	−8.4	−17.6	+0.059	+0.114	+0.177
1	rcp26	+0.5	+2.3	+3.7	+0.049	+0.065	+0.063
	rcp45	+0.6	+0.1	−0.7	+0.048	+0.076	+0.091
	rcp60	−0.3	−2.1	−6.2	+0.043	+0.067	+0.098
	rcp85	+0.0	−1.4	−5.3	+0.051	+0.098	+0.157
Hierarch	Hierarch	+0.3	−0.1	−1.7	+0.048	+0.080	+0.107

5.5. Hydrologic Modeling

The Hydrological Evaluation of Landfill Performance model version 3.07 (HELP3) (Schroeder et al. 1994) is used in this study to estimate regional potential groundwater recharge, surface runoff and evapotranspiration (ET) in southeastern Louisiana and southwestern Mississippi given aforementioned climate projections. HELP3 is a quasi-two-dimensional physically-based, deterministic, water-routing model, which simulates hydrologic processes, including surface runoff, evapotranspiration, vegetative growth, soil moisture storage, and vertical unsaturated drainage, for each discrete layered soil column. The HELP3 model has been used in many hydrological studies to estimate potential groundwater recharge, runoff and evapotranspiration (e.g. Khire et al., 1997; Jyrkama et al., 2007; Scibek et al., 2007; Toews and Allen, 2009; Calderhead et al., 2012), and has been extensively tested and was found to be an proper tool for hydrologic studies (Peyton and Schroeder, 1988; Schroeder et al. 1994; Schroeder and Peyton, 1987). The HELP3 model has been compared with HELP/VS2DT model that solves the Richard's equation, and it is found that while both models showed similar mean annual recharge, the HELP3 model is much faster and more computationally efficient than HELP/VS2DT (Gogolev, 2002). Also, Risser et al. (2005) compared HELP3 to the recession-curve displacement method (RORA) and the hydrograph separation method (PART) for estimating groundwater recharge and found that HELP3 showed the best agreement with direct recharge measurements of an Agricultural Research Service (ARS) research site in a small watershed in the eastern United States.

5.5.1. HELP3 Input Data

For this study, historical daily precipitation and temperature data with a resolution of 12 km from 1950 to 2009 were obtained from Maurer et al. (2002) and Maurer (2013). Average

annual wind speed and average quarterly relative humidity were obtained from the Southern Regional Climate Center (Robbins, 2013). The downscaled solar radiation data was generated synthetically using the weather generator (WGEN) model of Richardson and Wright (1984). The generated values of solar radiation are computed as a function of the daily mean precipitation for each climate zone using the same statistical characteristics of the historical solar radiation at New Orleans and Baton Rouge (Louisiana) and Jackson (Mississippi) from the HELP3 model. Then, the statistical characteristics were adjusted for each climate zone's latitude.

The detailed surficial soil texture classes were obtained from the Natural Resources Conservation Service (NRCS, 2014). The corresponding total porosity, field capacity, wilting point and saturated hydraulic conductivity for all soil texture classes were then determined using the table of default soil characteristics in the HELP3 user manual. The thickness for the surficial soil layer was considered up to 1.5 m in depth. For the soil texture and thickness beneath the surficial soil layer, 3,431 well logs and drillers' logs in the study area were compiled and analyzed to determine lithostratigraphy up to the top-most major sands. The lithology of the closest well logs is assigned to the corresponding subdivisions. Land use and land cover data at high spatial resolution (30 m) was obtained from the National Land Cover Dataset 2011 (NLCD 2011), which is the most recent national land cover product created by the Multi-Resolution Land Characteristics (MRLC) Consortium (Jin et al., 2014). To determine curve number for each subdivisions in the study area, the surficial soil map and the land use/land cover map were joined to derive a map of runoff-curve number (CN) based on the SCS Technical Release 55 (NRCS 1986). The topographic slope and the slope length were used to adjust the curve number for each subdivision. The topographic slope and the slope length were derived using ArcGIS and the

DEM map in 10-m resolution obtained from Mississippi Geospatial Clearinghouse and Atlas: Louisiana's Statewide GIS.

HELP3 requires the leaf area index (LAI) to calculate transpiration rates for vegetation. The yearly averaged LAI for each subdivision was calculated from the LAI dataset generated by reprocessing the MODIS (Yuan et al., 2011). The leaf area index of the study area ranges from 1 to 6 with the mean of 3.4. LAI has 1 km resolution, which is much higher than the land use map. In other words, the same land use type may have different LAI values. The averaged standard deviation of the LAI for land use is 1.08, which shows fair consistency between the LAI and the land use. The maximum rooting depth of vegetation for each subdivision was estimated based on its land use, soil and vegetation types according to the study of the maximum rooting depth on a global scale (Canadell et al., 1996). The minimum and maximum evaporative zone depth is 10.5 cm and 730.5 cm, respectively. The mean evaporative zone depth is 380.1 cm. HELP3 requires the beginning and the end of a growing season to compute seasonal variation in the LAI through a general vegetative growth model. In this study, the growing season begins in earliest mid-January and ends in mid-December, which represents successive frost free days or days with temperatures above 0 (Lavalle et al., 2009). The growing season is assumed constant in the HELP3 model.

5.5.2. Parallel Computation for High-Resolution Hydrologic Prediction

For each of 133 climate models, a large number (2,669,533) of HELP3 model runs are needed for hydrologic prediction for the study area. Hydrologic predictions become computationally impractical when running HELP3 sequentially in a single-core processor. This study used the aforementioned parallel procedure in chapter 3 to divide 2,669,533 HELP3 model runs to multiple cores of a supercomputer, SuperMike-II at Louisiana State University, for

parallel computation. SuperMike-II is a 146 TFlops Peak Performance 440 compute node cluster running the Red Hat Enterprise Linux 6 operating system. Each node contains two 8-Core Sandy Bridge Xeon 64-bit processors operating at a core frequency of 2.6 GHz. The runtime, speedup and efficiency using a large number of cores for the study area were discussed in chapter 3. The parallel computation significantly reduced total computation time.

This study calibrated the HELP3 model using the USGS WaterWatch runoff database for the 26 hydrologic units (see Figure 5.2) using the aforementioned parallel computing technique in the SuperMike-II. The root mean square error (RMSE) between WaterWatch yearly runoff and HELP3 yearly runoff ranges from 90.32 to 137.45 mm for individual hydrologic units. The mean RMSE of all 26 hydrologic units is 116.54 mm, which is much smaller than the range of the WaterWatch yearly runoff data. The calibrated HELP3 model was verified by the estimated ET obtained from MOD16 evapotranspiration dataset based on the MODIS remote sensing data (Mu et al., 2007; Mu et al., 2011). The RMSE of the HELP3 yearly estimated ET versus the MOD16 yearly computed ET from 2000 to 2010 is 93.52 mm, which is much smaller than the range of the MOD16 ET estimates.

5.6. Results and Discussion

5.6.1. HBMA Temporal Analysis

Potential recharge, runoff and ET projections of southwestern Mississippi and southeastern Louisiana for 2010-2099 using the best and second best climate models at level 3 for four emission paths are shown in Figure 5.12. Projected potential recharge shows much larger variability compared to runoff and ET projections. Potential recharge quantities projected by different climate models are quite different. ET projection for the 21 century is consistently high regardless of climate models and emission paths.

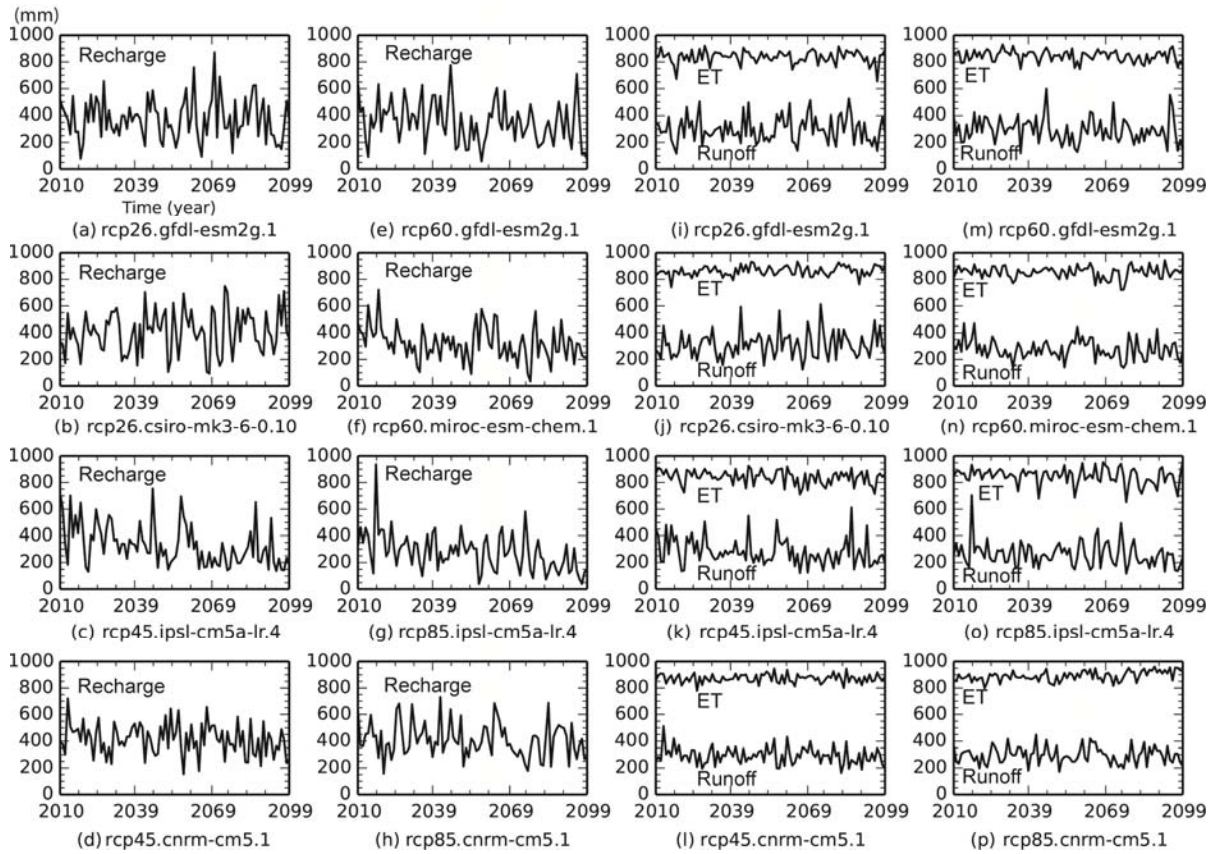

Figure 5.12: Potential recharge, runoff and ET projections for 2010-2099 using the best and the second best climate models at level 3.

Using BMA at level 2, the mean projection and uncertainty of potential recharge, runoff, and ET due to uncertain GCM initial conditions are shown in Figure 5.13. Since many initial conditions are used in CSIRO-Mk3.6.0, IPSL-CM5A-LR, and CanESM2, these GCMs show noticeable projection uncertainty. Uncertainty in potential recharge projection is much higher than that in runoff and ET. ET has relatively less projection uncertainty. The csiro-mk3-6-0 model generally shows higher uncertain projections than other GCMs due to using the largest number of initial conditions. Because of using the largest number of initial conditions, the csiro-mk3-6-0 model is more important than other GCMs as shown in Figure 5.3 and Figure 5.4.

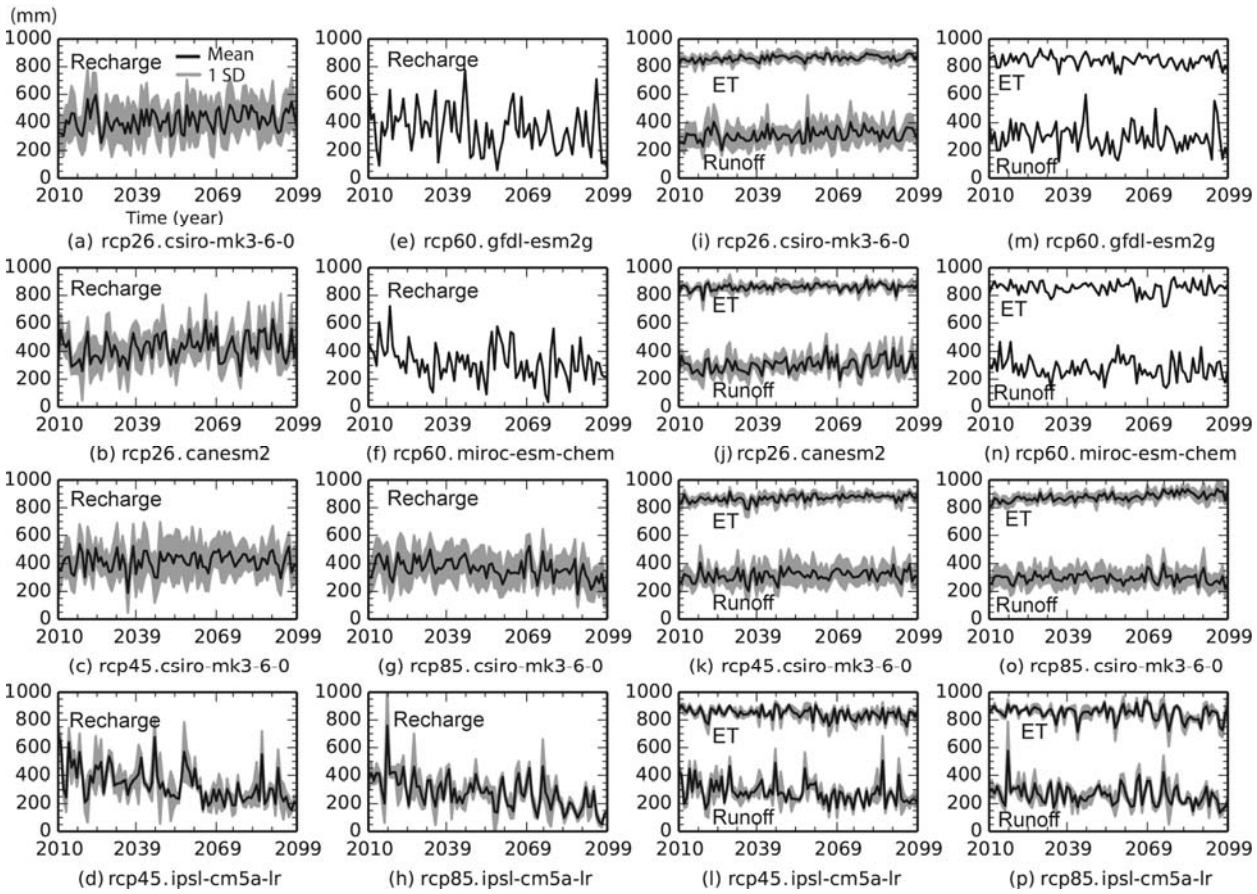

Figure 5.13: BMA mean and one standard deviation (SD) interval for potential recharge, runoff and ET projections for 2010-2099 using the best and the second best GCMs at level 2.

Similarly, using BMA at level 1, the mean projection and uncertainty of potential recharge, runoff, and ET due to uncertain GCMs and GCM initial conditions are shown in Figure 5.14. Potential recharge projection shows the highest uncertainty while ET projection shows the lowest uncertainty. For potential recharge projection, RCP2.6 projects an increasing trend, RCP4.5 and RCP6.0 shows a constant trend, and RCP8.5 shows a decreasing trend. All emission paths show a constant trend in runoff and ET projections.

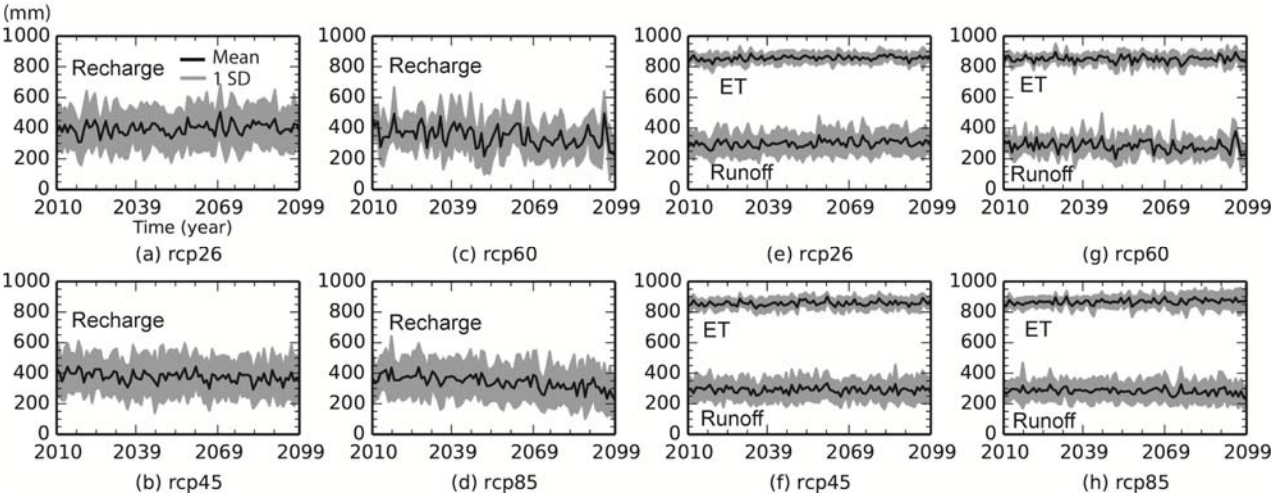

Figure 5.14: BMA mean and one standard deviation (SD) interval of potential recharge, runoff and ET projections for 2010-2099 using all climate models under corresponding emission paths at level 1.

Using the entire 133 climate projections, the BMA mean and one standard deviation interval of annual potential recharge, runoff and ET predictions from 2010 to 2099 for the study area is shown in Figure 5.15. These predictions take into account uncertainties arising from different GCMs, GCM initial conditions, and emission paths. The projections are the results of the hierarch model in Figure 5.5. The projected mean potential recharge plot indicates a slightly decreasing trend while the projected mean runoff and ET plots indicate constant trends throughout 2099. The coefficient of variation (CV) of projections for each year was calculated by dividing the standard deviation to the mean in Figure 5.15. The ranges of CV for potential recharge, runoff and ET projections are 31.5 %-54.1 %, 23.3 %-35.6 % and 3.6 %-8.9 %, respectively. The temporal average CV for potential recharge, runoff and ET projections are 40.1 %, 28.6 % and 5.4%, respectively. Again, projected recharge has much higher uncertainty than runoff and ET. High uncertainty in potential recharge projection indicates that potential recharge prediction is more sensitive to climate projections than runoff and ET predictions.

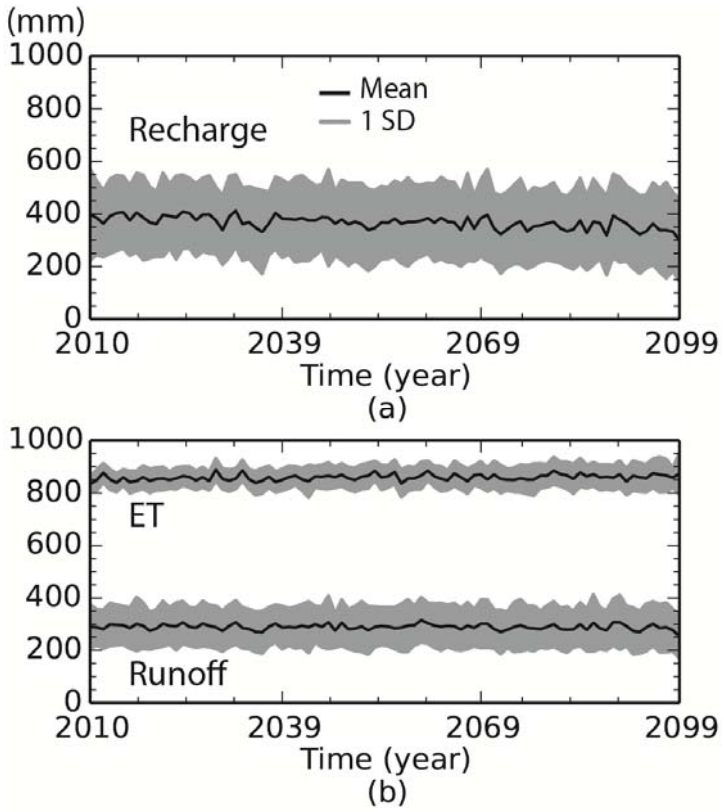

Figure 5.15: BMA mean and one standard deviation (SD) interval of potential recharge, runoff and ET projections for 2010-2099 at the hierarch level using 133 climate models.

5.6.2. Projection Anomalies

Table 5.5 shows projection anomalies in mean annual potential recharge, runoff and ET for three 30-year periods (2010-2039, 2040-2069, and 2070-2099) with respect to mean annuals of 1950-2009 at different levels of the BAM tree in Figure 5.5. The estimated mean annual potential recharge, runoff and ET for the study area in 1950-2009 are 337.4 mm, 352.8 mm and 832.9 mm, respectively, which accounts for 22.1 %, 23.1 %, and 54.4 % of the mean annual precipitation in the study area. Projection anomalies using the best and the second best climate models under each emission path (level 3 of Table 5.5) show that potential recharge is likely to increase in 2010-2069. There is no clear trend in 2070-2099. The rcp26.csiro-mk3-6-0.10 model

projects highest potential recharge increase (+26.9 %) while rcp85.ipsl-cm5a-lr.4 model projects highest potential recharge decrease (−38.9 %) in 2070-2099. Runoff is likely to decrease through 2099 while ET is likely to increase comparing to their mean annual in 1950-2009. ET increase is not significant. Projection anomalies at level 2 show the same observations as level 1, GCMs produce wide range of potential recharge projection. In general, potential recharge is likely to increase in 2010-2069. Runoff is likely to decrease and ET is likely to slightly increase in the next century.

Table 5.5: Projected changes in mean annual potential recharge, runoff and evapotranspiration (ET) with respect to mean annuals of 1950-2009. Level 3 lists the best and the second best climate models under each emission path. Level 2 lists the best and the second best GCMs under each emission path.

Level	Climate model	Potential recharge (%) Mean annual = 337. 4 mm			Runoff (%) Mean annual = 352.8 mm			ET (%) Mean annual = 832.9 mm		
		2010-2039	2040-2069	2070-2099	2010-2039	2040-2069	2070-2099	2010-2039	2040-2069	2070-2099
3	rcp26.gfdl-esm2g.1	+11.6	+8.9	+13.4	−16.3	−15.8	−14.7	+0.5	+0.3	+0.5
	rcp26.csiro-mk3-6-0.10	+12.7	+22.0	+26.9	−17.8	−10.2	−9.1	+2.1	+4.7	+3.9
	rcp45.ipsl-cm5a-lr.4	+21.5	−2.5	−24.7	−12.2	−21.6	−27.9	+2.8	+0.3	−0.2
	rcp45.cnrm-cm5.1	+27.0	+26.9	+12.4	−14.7	−16.0	−20.7	+4.0	+5.2	+4.6
	rcp60.gfdl-esm2g.1	+18.0	+4.0	−8.9	−12.2	−18.6	−21.3	+2.5	+1.6	−0.1
	rcp60.miroc-esm-chem.1	+4.8	−2.0	−18.4	−19.9	−19.1	−27.0	+2.3	+2.5	+1.9
	rcp85.ipsl-cm5a-lr.4	+1.4	−17.7	−38.9	−20.4	−25.0	−31.9	+3.5	+2.3	−0.4
	rcp85.cnrm-cm5.1	+27.6	+28.2	+8.2	−16.2	−12.2	−20.1	+5.3	+6.4	+9.2
2	rcp26.csiro-mk3-6-0	+18.0	+22.2	+30.0	−16.3	−11.0	−7.8	+2.2	+4.0	+4.2
	rcp26.canesm2	+15.8	+32.7	+28.4	−19.7	−11.5	−12.0	+2.2	+4.0	+3.4
	rcp45.csiro-mk3-6-0	+19.5	+24.6	+25.3	−15.0	−9.3	−8.2	+2.3	+4.7	+5.6
	rcp45.ipsl-cm5a-lr	+21.1	+0.3	−23.2	−13.1	−20.4	−28.5	+2.9	+1.5	−0.1
	rcp60.gfdl-esm2g	+18.0	+4.0	−8.9	−12.2	−18.6	−21.3	+2.5	+1.6	−0.1
	rcp60.miroc-esm-chem	+4.8	−2.0	−18.4	−19.9	−19.1	−27.0	+2.3	+2.5	+1.9
	rcp85.csiro-mk3-6-0	+14.4	+9.0	−2.6	−16.5	−14.9	−17.7	+2.9	+5.0	+8.1
	rcp85.ipsl-cm5a-lr	+3.1	−17.6	−40.7	−19.7	−25.4	−33.4	+3.5	+2.9	−0.6
1	rcp26	+15.3	+17.4	+21.4	−17.4	−14.5	−12.9	+2.0	+3.2	+3.2
	rcp45	+15.2	+11.8	+7.8	−17.4	−17.1	−17.8	+2.3	+3.2	+3.2
	rcp60	+12.2	+4.9	−7.0	−17.6	−19.1	−23.6	+2.1	+2.3	+1.9
	rcp85	+10.7	+3.5	−10.3	−18.3	−18.8	−22.8	+3.4	+4.3	+4.8
Hierarch	Hierarch	+13.4	+9.8	+3.7	−17.7	−17.2	−18.8	+2.6	+3.5	+3.6

Projection anomalies at level 1 show consistent results with the development of future emissions. RCP2.6 is positive for potential recharge and projects continuous potential recharge increase for the next century owing to the assumption of strong mitigation, the lowest GHG concentration, and the least warming. RCP4.5 also shows positive for potential recharge, but with a decreasing trend over time. RCP6.0 and RCP8.5 project potential recharge increase in 2010-2069. The decreasing trend indicates lesser potential recharge in 2070-2099 than in 1950-2009. RCP8.5 shows the least potential recharge increase and the highest potential recharge decrease. All emission paths show decreasing runoff and increasing ET in the next century compared to their annual means in 2010-2069.

Using all 133 climate models, the BMA mean potential recharge in southwestern Mississippi and southeastern Louisiana is projected to increase with a decreasing trend for 30-year interval. Runoff is likely to decrease and ET is likely to increase in the next century.

5.6.3. Spatial Analysis

The BMA means of annual potential recharge, runoff and ET projections for 728 HUC12s in 2010-2039, 2040-2069, and 2070-2099 using 133 climate models are shown in Figure 5.16. The areal changes for every 30-year period are not distinguishable since the maximum changes of potential recharge, runoff and ET projections are relatively small (56.2 mm, 44.7 mm and 38.6 mm, respectively). High potential recharge rate was estimated at the outcrops of Miocene deposits in southwestern Mississippi, which are the potential recharge zones of the deep sands in southeastern Louisiana.

Projection uncertainty increases over time as shown in Figure 5.17. The BMA standard deviations of projected potential recharge, runoff and ET in 2070-2099 range 4.1-123.2 mm, 1.7-96.7 mm and 7.8-45.6 mm, respectively. The CV of projected potential recharge, runoff and ET

in 2070-2099 range 12.3-44.6 %, 8.1-24.2 % and 2.4-6.4 %, respectively. Potential recharge projection has greater uncertainty than runoff projection, followed by ET projection.

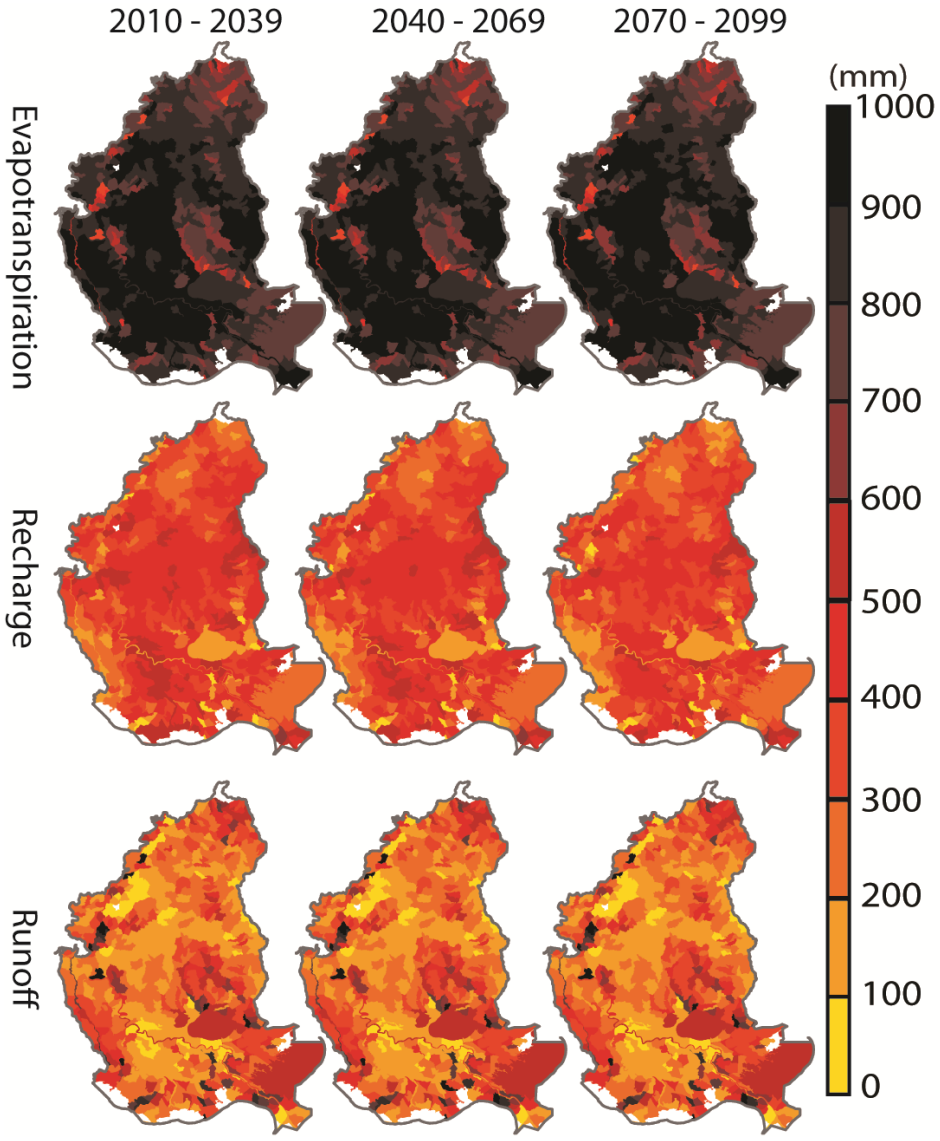

Figure 5.16: BMA mean of annual potential recharge, runoff and ET projections for 30-year interval at the hierarch level using 133 climate models.

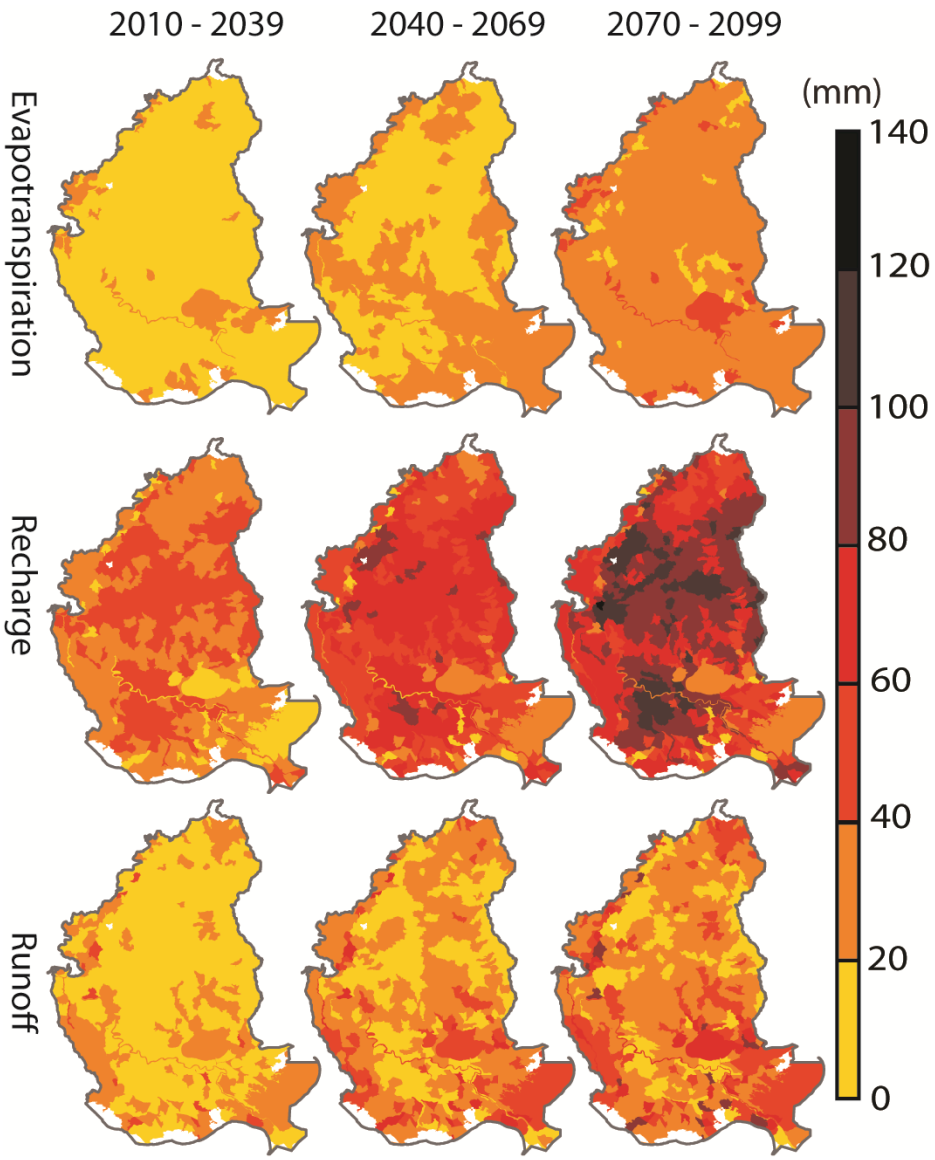

Figure 5.17: BMA standard deviation of annual potential recharge, runoff and ET projections for 30-year interval at the hierarch level using 133 climate models.

Contributions of individual sources of uncertainty to the total uncertainty of projected potential recharge in 728 HUC12s are shown in Figure 5.18. Contributions of emission paths, climate models, and initial conditions to the total uncertainty of projections is the proportion of the variances in the first, second, and third terms in Eq.(12), respectively, to the total variance $\mathrm{Var}(\Delta \mid \mathbf{D})$. The fourth term at the right-hand side of Eq.(12) represents the within-model

variance of the 133 climate models listed in Table 5.1. Since we cannot access the uncertainty of individual GCMs, this study does not consider this term. Figure 5.18 supports that GCM uncertainty is the dominant source of uncertainty in assessing climate change impacts on hydrologic projection (e.g., Wilby and Harris, 2006; Kay et al., 2009; Prudhomme and Davies, 2009; Woldemeskel et al., 2012; Teng et al., 2009). Contribution of emission path uncertainty to the total uncertainty increases every 30-year period since emission paths start to diverge significantly after mid-century, resulting in higher uncertainty in 2070-2099. This indicates that climate models' parameterizations, sensitivities and responses to greenhouse gases and other forcings grow over time and become evident. On the contrary, contribution of GCM initial condition uncertainty to the total uncertainty decreases every 30-year period, indicating that impact of GCM initial conditions on total potential recharge projection uncertainty becomes less important as emission path uncertainty increases towards the end of the century.

Means and standard deviations of uncertainty contributions of the three sources to the total uncertainty of projected potential recharge over 728 HUC12s are shown in Table 5.6. The small standard deviations indicate variations of uncertainty contributions of individual sources across the HUC12s are small. The mean uncertainty contribution from GCMs dominates and ranges from 62.2% to 77.1%. The GCMs and GCM initial conditions contribute 95.7% of total uncertainty to potential recharge projection in 2010-2039. The GCMs and emission paths contribute 91.6% of total uncertainty in 2070-2099.

Although not presented in this study, the contributions of the three sources of uncertainty to the projected runoff and ET are similar to the projected potential recharge in the study area.

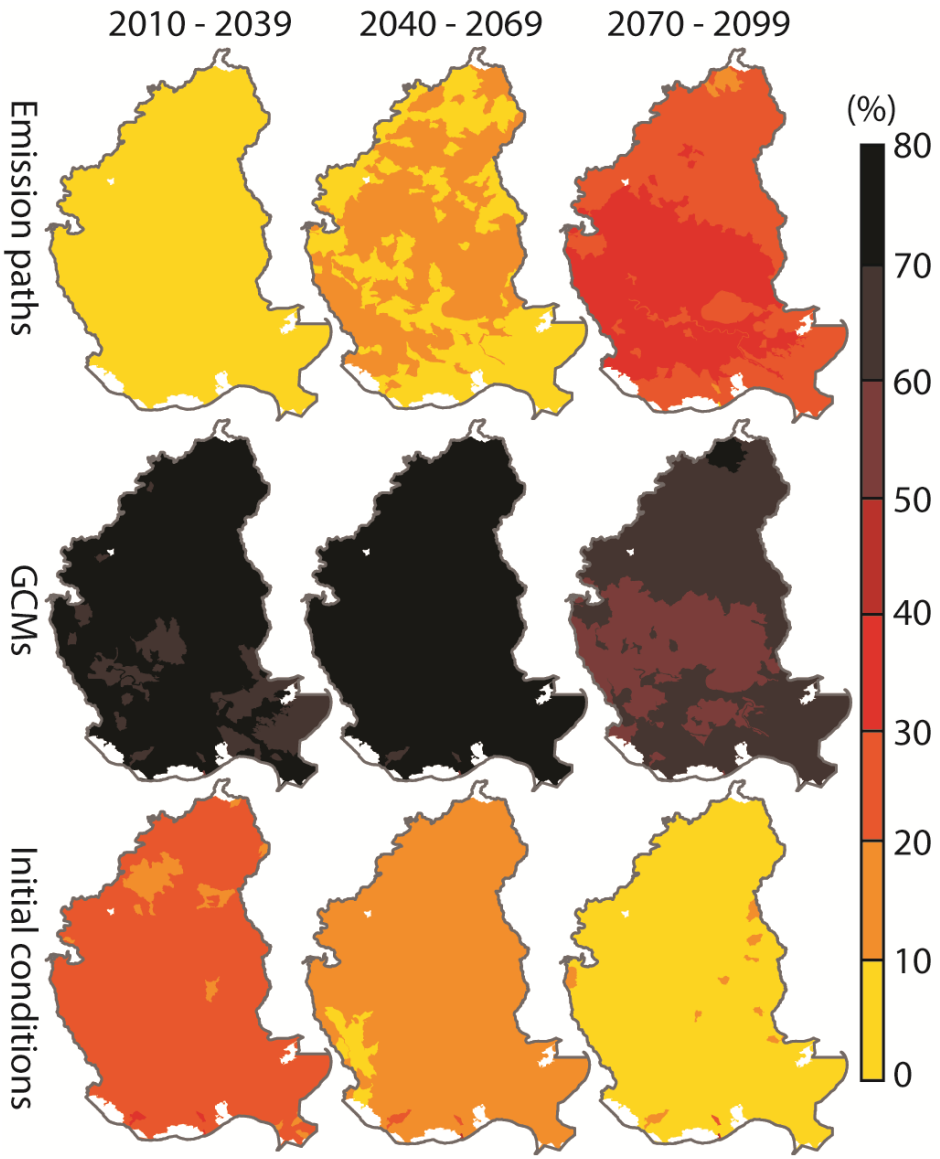

Figure 5.18: Contributions of individual sources of uncertainty to the total uncertainty of projected potential recharge for 30-year interval.

Table 5.6: Mean and standard deviation (SD) of contributions of individual sources of uncertainty to the total uncertainty of projected potential recharge over 728 HUC12s.

Uncertainty Source	2010-2039		2040-2069		2070-2099	
	Mean (%)	SD (%)	Mean (%)	SD (%)	Mean (%)	SD (%)
Emission Path	4.3	1.2	10.0	1.4	29.4	3.6
GCM	72.5	2.1	77.0	2.0	62.2	3.7
GCM Initial Condition	23.2	2.4	13.0	2.0	8.4	1.7

5.7. Conclusions

The hierarchical Bayesian model averaging (HBMA) method provides an intriguing approach to analyze different types of uncertainties existing in climate projections and consequent impacts on hydrologic projections. Working on the 133 sets of 1/8-degree-BCCA-downscaled daily precipitation and temperature projections of CMIP5, the HBMA is able to display the hierarchical nature of emission scenario uncertainty (emission paths) and climate modeling uncertainty (GCMs and GCM initial conditions) and provide hydrological projection means and variances thought Bayesian model averaging.

Quantifying climate-related hydrologic projection uncertainty is computational demanding and requires parallel computation. This study successfully demonstrates a detailed hydrologic modeling work for southwestern Mississippi and southeastern Louisiana using CPU-based multi-core supercomputers. The modeling complexity includes highly parameterized hydrologic model (2.6 million homogeneous subdivisions for the HELP3 model), 133 sets of daily precipitation and temperature projections, and a century-long simulation.

The GCM posterior model probabilities suggest that GCMs with more initial conditions in the emission paths are usually important, which, however, exhibit more projection uncertainty. The best GCM for southwestern Mississippi and southeastern Louisiana is CSIRO-Mk3.6.0 that uses 10 initial conditions in RCP2.6, RCP4.5, and RCP8.5, and is followed by IPSL-CM5A-LR, CanESM2, and MIROC5 models that use at least 3 initial conditions for projections.

The hydrologic modeling and HBMA results show higher spatial and temporal variability and variance in projected potential recharge than those in projected runoff and evapotranspiration. Evapotranspiration projection exhibits the least uncertainty. In general, future potential recharge in southwestern Mississippi and southeastern Louisiana is likely to increase in

next several decades and is not certain about its trend toward the end of the century. Runoff is likely to decrease significantly while evapotranspiration is likely to increase slightly in the next century.

The prevailing GCM uncertainty is the major contributor to the total uncertainty of future hydrologic projections in southwestern Mississippi and southeastern Louisiana. Contributions from emission path uncertainty and GCM initial condition uncertainty compensate each other over time. Contribution from the initial condition uncertainty is noticeable for first several decades and decreases over time toward the end of the century. On the contrary, contribution of the emission path uncertainty is not evident in next decades, but grows after mid-century and becomes significant at the end of the century.

This study does not discuss uncertainty from hydrological models. We acknowledge that uncertainty from hydrologic model is also very important and needs to be considered in the future study.

6. Concluding Remarks

- This study successfully developed a GIS-based water budget framework in order to estimate high spatiotemporal resolution groundwater recharge, runoff and ET estimation for large-scale humid areas. The framework involves the USGS WaterWatch runoff database to calibrate HELP3 models and uses the MODIS evapotranspiration database to verify HELP3 models. Quantifying climate-related hydrologic projection uncertainty is computational demanding and requires parallel computation. The framework includes parallel programming to divide required HELP3 model runs to multiple cores of a supercomputer to significantly reduce computing time. The parallel programming allows the methodology to be applied to century-long hydrologic projections for the area of southwestern Mississippi and southeastern Louisiana, under a large number of emission scenarios and GCMs.
- Comparative study of CMIP3 climate projections shows that the impact of climate change on potential groundwater recharge, surface runoff and ET in the study area is unclear as it highly depends on selected climate models and scenarios. It was found that the GFDL climate model projects more intense changes in future precipitation, temperature and solar radiation in the study area than the PCM model for the 21st century. Under the CMIP3 climate projections, potential recharge is likely to increase in 2010-2039 and likely to decrease in 2070-2099 with respect to the estimated historical potential recharge (1950-2009). The study area is subjected to a wide range of future potential recharge projections, decreasing in 2070-2099 by much as −58.1 % (GFDLA1FI) and to increasing by as much as +19.1 % (PCMB1 scenario).
- The future potential recharge variation is strongly correlated with the precipitation projections. It was found that potential recharge is most sensitive to the changes in future

precipitation, followed by solar radiation, and then temperature. The precipitation and temperature uncertainty analyses show that precipitation influences potential recharge more than temperature. The most pessimistic scenario, A1FI, under both CMIP3 GCMs projects the highest potential recharge sensitivity to the precipitation, temperature and solar radiation, followed by the A2 scenario, and then the B1 scenario. This order is consistent with the order of increasing of the degree of global warming in the emission scenarios. Recharge zones or subdivisions with high potential recharge demonstrated lower potential recharge sensitivity to precipitation, temperature and solar radiation.

- The hierarchical Bayesian model averaging (HBMA) method provides a robust approach to segregate and prioritize different types of uncertainties existing in climate projections and consequent impacts on hydrologic projections. The HBMA was successfully implemented to the 133 sets of 1/8-degree-BCCA-downscaled of century-long daily precipitation and temperature projections of CMIP5 incorporated with highly parameterized hydrologic model (2.6 million homogeneous subdivisions for the HELP3 model). The HBMA is able to demonstrate the hierarchical nature of emission scenario uncertainty (emission paths) and climate modeling uncertainty (GCMs and GCM initial conditions) and provide hydrological projection means and variances thought Bayesian model averaging.
- The uncertainty analysis of hydrologic projections under CMIP5 Climate projection showed that projected potential recharge is subjected to higher spatial and temporal variability and variance than those in projected runoff and evapotranspiration. Evapotranspiration projection exhibits the least uncertainty. Generally, future potential recharge projection of southwestern Mississippi and southeastern Louisiana is likely to increase in next several decades and is not

certain about its trend toward the end of the century. Runoff is likely to decrease significantly while evapotranspiration is likely to increase slightly in the next century.

- The prevailing GCM uncertainty is the major contributor to the total uncertainty of future hydrologic projections in southwestern Mississippi and southeastern Louisiana. Contributions from emission path uncertainty and GCM initial condition uncertainty compensate each other over time. Contribution from the initial condition uncertainty is noticeable for first several decades and decreases over time toward the end of the century. On the contrary, contribution of the emission path uncertainty is not evident in next decades, but grows after mid-century and becomes significant at the end of the century.
- The uncertainties in future hydrological projections arising from hydrological model uncertainly (parameter uncertainly and structural uncertainty) is not discussed in this study. We acknowledge that uncertainty from hydrologic model is also very important and needs to be considered in the future study.

References

Aguilera H, Murillo JM (2009) The effect of possible climate change on natural groundwater recharge based on a simple model: a study of four karstic aquifers in SE Spain. Environ Geol 57(5):963-974. doi:10.1007/s00254-008-1381-2

Ajami NK, Duan Q, Gao X, Sorooshian S (2006) Multimodel Combination Techniques for Analysis of Hydrological Simulations: Application to Distributed Model Intercomparison Project Results. J Hydrometeorol 7(4), 755-768, doi:10.1175/JHM519.1

Allison G, Gee G, Tyler S (1994) Vadose-zone techniques for estimating groundwater recharge in arid and semiarid regions. Soil Sci Soc Am J 58(1):6-14, doi: 10.2136/sssaj1994.03615995005800010002x

Ali R, McFarlane D, Varma S, Dawes W, Emelyanova I, Hodgson G (2012) Potential climate change impacts on the water balance of regional unconfined aquifer systems in South-Western Australia. Hydrol Earth Syst Sc 16(12):4581-4601, doi: 10.5194/hess-16-4581-2012

Allen DM, Mackie DC, Wei M (2004) Groundwater and climate change: a sensitivity analysis for the Grand Forks aquifer, southern British Columbia, Canada. Hydrogeol J 12:270–290, doi: 10.1007/s10040-003-0261-9

Batelaan O, De Smedt F (2007) GIS-based recharge estimation by coupling surface–subsurface water balances. J Hydrol 337(3), 337-355, doi: 10.1016/j.jhydrol.2007.02.001

Bates B, Kundzewicz ZW, Wu S, Palutikof J (2008) Climate change and water, Technical Paper VI of the Intergovernmental Panel on Climate Change (IPCC). Secretariat, Geneva, p. 210.

Barthel R, Reichenau TG, Krimly T, Dabbert S, Schneider K, Mauser W (2012) Integrated modeling of global change impacts on agriculture and groundwater resources. Water Resour Manag 26(7):1929-1951, doi:10.1007/s11269-012-0001-9

Beigi E, Tsai FT-C (2014) A GIS-based water budget framework for high-resolution groundwater recharge estimation of large-scale humid regions. J Hydrol Eng-ASCE 19(8) 05014004, doi:10.1061/(ASCE)HE.1943-5584.0000993.

Beigi E, Tsai F T-C (2015). Comparative study of climate-change scenarios on groundwater recharge, southwestern Mississippi and southeastern Louisiana, USA. Hydrogeol J, 1-18, doi: 10.1007/s10040-014-1228-8

Birkhoff G (1967) Lattice Theory, 3rd ed., Colloquium Publications, Vol. 25, American Mathematical Society, Providence, RI, doi: 10.2307/2268441

Bouraoui F, Vachaud G, Li LZX, Le Treut H, Chen T (1999). Evaluation of the impact of climate changes on water storage and groundwater recharge at the watershed scale. Clim Dynam 15:153–161, doi: 10.1007/s003820050274

Brakebill, J. W., Wolock, D. M., and Terziotti, S. E.: Digital hydrologic networks supporting applications related to spatially referenced regression modeling, J. Am. Water Resour. Assoc., 20 47, 916–932, doi:10.1111/j.1752-1688.2011.00578.x, 2011

Brouyere S, Carabin G, Dassargues A (2004) Climate change impacts on groundwater resources: modelled deficits in a chalky aquifer, Geer Basin, Belgium. Hydrogeol J 12:123–134, doi: 10.1007/s10040-003-0293-1

Buono A (1983) The Southern Hills regional aquifer system of southeastern Louisiana and southwestern Mississippi. U.S. Geological Survey, Water-Resources Investigations Report 83-4189, 38p.

Buser CM, Künsch HR, Lüthi D, Wild M, Schär C (2009) Bayesian multi-model projection of climate: bias assumptions and interannual variability. Clim Dynam, 33(6), 849-868, doi:10.1007/s00382-009-0588-6

Canadell J, Jackson R, Ehleringer J, Mooney H, Sala O, Schulze E-D (1996) Maximum rooting depth of vegetation types at the global scale. Oecologia 108(4):583-595, doi:10.1007/BF00329030

Calderhead AI, Martel R, Garfias J, Rivera A, Therrien R (2012) Pumping dry: an increasing groundwater budget deficit induced by urbanization, industrialization, and climate change in an over-exploited volcanic aquifer. Environ Earth Sci 66(7):1753-1767, doi:10.1007/s12665-011-1398-9

Cayan DR, Maurer EP, Dettinger MD, Tyree M, Hayhoe K (2008) Climate change scenarios for the California region. Climatic change 87(1):21-42. doi:10.1007/s10584-007-9377-6

Chen J, Brissette FP, Leconte R (2011) Uncertainty of downscaling method in quantifying the impact of climate change on hydrology. J Hydrol, 401(3), 190-202, doi:10.1016/j.jhydrol.2011.02.020

Chen J, Brissette F P, Poulin A, Leconte R (2011) Overall uncertainty study of the hydrological impacts of climate change for a Canadian watershed. Water Resour Res, 47(12), doi:10.1029/2011WR010602

Chen H, Xu C-Y, Guo S (2012) Comparison and evaluation of multiple GCMs, statistical downscaling and hydrological models in the study of climate change impacts on runoff. J Hydrol, 434–435, 36-45, doi:10.1016/j.jhydrol.2012.02.040

Chen ZH, Grasby SE, Osadetz KG (2002) Predicting average annual groundwater levels from climatic variables: an empirical model. J Hydrol 260(1–4):102–117, doi: 10.1016/s0022-1694(01)00606-0

Connolley WM, Bracegirdle TJ (2007) An Antarctic assessment of IPCC AR4 coupled models. Geophys Res Lett , 34(22), doi:10.1029/2007gl031648

Cooper DM, Wilkinson WB, Arnell NW (1995) The effects of climate changes on aquifer storage and river baseflow. Hydrol Sci J 40(5):615–631, doi:10.1080/02626669509491448

Croley TE, Luukkonen CL (2003) Potential effects of climate change on ground water in Lansing, Michigan. J Am Water Resour Assoc 39(1):149–163, doi: 10.1111/j.1752-1688.2003.tb01568.x

Crosbie RS, McCallum JL, Walker GR, Chiew, FH (2010) Modelling climate-change impacts on groundwater recharge in the Murray-Darling Basin, Australia. Hydrogeol J 18(7):1639-1656, doi: 10.1007/s10040-010-0625-x

Crosbie RS, Scanlon BR, Mpelasoka FS, Reedy RC, Gates JB Zhang L (2013). Potential climate change effects on groundwater recharge in the high plains aquifer, USA. Water Resour Res 49:3936–3951. doi:10.1002/wrcr.20292

Cubasch U, Meehl GA, Boer GJ, Stouffer RJ, Dix M, Noda A, Senior CA, Raper S, Yap KS (2001) Projections of future climate change., In: Houghton, J.T., et al. (eds.),Climate Change 2001: The Scientific Basis. Contribution of Working Group I to the Third Assessment Report of the Intergovernmental Panel on Climate Change, pp.526-582 Cambridge University Press Cambridge

Dawes W, Ali R, Varma S, Emelyanova I, Hodgson G, McFarlane D (2012) Modelling the effects of climate and land cover change on groundwater recharge in south-west Western Australia. Hydrol Earth Syst Sci 16:2709–2722, doi: 10.5194/hess-16-2709-2012

Dettinger MD (2013) Projections and downscaling of 21st century temperatures, precipitation, radiative fluxes and winds for the Southwestern US, with focus on Lake Tahoe., Climatic Change 116(1):17-33, doi: 10.1007/s10584-012-0501-x

Déqué M (2007) Frequency of precipitation and temperature extremes over France in an anthropogenic scenario: Model results and statistical correction according to observed values. Glob Plan Change, 57, 16-26, doi:10.1016/j.gloplacha.2006.11.030

Deser C, Phillips A, Bourdette V, Teng H (2012) Uncertainty in climate change projections: the role of internal variability. Clim Dynam, 38(3-4), 527-546, doi:10.1007/s00382-010-0977-x

De Vries JJ, Simmers I (2002) Groundwater recharge: an overview of processes and challenges. Hydrogeol J 10(1):5-17, doi: 10.1007/s10040-001-0171-7

Dicken, Connie L, Nicholson, Suzanne W, Horton, John D, Foose, Michael P, Mueller, Julia AL (2005) Integrated Geologic Map Databases for the United States: Alabama, Florida, Georgia, Mississippi, Louisiana, North Carolina, and South Carolina. U.S. Geological Survey, Open-File Report 2005-1323, Reston, VA.

Dripps W, Bradbury K (2007) A simple daily soil–water balance model for estimating the spatial and temporal distribution of groundwater recharge in temperate humid areas. Hydrogeol J 15(3):433-444, doi: 10.1007/s10040-007-0160-6

Dong L, Xiong L, Yu KX (2013) Uncertainty Analysis of Multiple Hydrologic Models Using the Bayesian Model Averaging Method. J Appl Math, doi:10.1155/2013/346045

Duan Q, Ajami NK, Gao X, Sorooshian S (2007) Multi-model ensemble hydrologic prediction using Bayesian model averaging. Adv Water Resour, 30(5):1371–86, doi:10.1016/j.advwatres.2006.11.014

Doblas-Reyes FJ, Pavan V, Stephenson DB (2003) The skill of multi-model seasonal forecasts of the wintertime North Atlantic Oscillation. Clim dynam, 21(5-6), 501-514, doi:10.1007/s00382-003-0350-4

Eckhardt, K., and Ulbrich, U. (2003). "Potential impacts of climate change on groundwater recharge and streamflow in a central European low mountain range." Journal of Hydrology, 284(1), 244-252, doi: 10.1016/j.jhydrol.2003.08.005

Elshall AS, Tsai FT-C (2014) Constructive epistemic modeling of groundwater flow with geological structure and boundary condition uncertainty under the Bayesian paradigm. J Hydrol, 517, 105-119, doi:10.1016/j.jhydrol.2014.05.027

Fitts CR (2002) Groundwater science. San Diego, California: Academic Press.

Foster I (1995) Designing and Building Parallel Programs: Concepts and Tools for Parallel Software Engineering. Addison-Wesley Publishing Company, Inc., Reading, MA.

Gebreyohannes T, De Smedt F, Walraevens K, Gebresilassie S, Hussien A, Hagos M, Amare K, Deckers J,Gebrehiwot K (2013) Application of a spatially distributed water balance model for assessing surface water and groundwater resources in the Geba basin, Tigray, Ethiopia. J Hydrol 499, 110-123, doi: 10.1016/j.jhydrol.2013.06.026

Gee GW, Hillel D (1988) Groundwater recharge in arid regions: review and critique of estimation methods. Hydrolo Process 2(3):255-266, doi: 10.1002/hyp.3360020306

Gleckler P, Taylor K, Doutriaux C (2008) Performance metrics for climate models. J Geophys Res, 113, D06104, doi:10.1029/2007JD008972

Giorgi F, Mearns LO (2002). Calculation of average, uncertainty range, and reliability of regional climate changes from AOGCM simulations via the ‘‘reliability ensemble averaging’’ (REA) method. J Clim, 15(10),1141–58, doi: 10.1175/1520-0442(2002)015<1141:coaura>2.0.co;2

Gogolev M I (2002) Assessing groundwater recharge with two unsaturated zone modeling technologies. Environ Geol 42(2-3):248-258, doi: 10.1007/s00254-001-0494-7

Görgen K, Beersma J, Brahmer G, Buiteveld H, Carambia M, Keizer de O, Krahe P, Nilson E, Lammersen R, Perrin C, Volken D (2010) Assessment of Climate Change Impacts on Discharge in the Rhine River Basin: Results of the RheinBlick2050 Project, CHR Rep I-23, 229 pp., Lelystad, Netherlands

Goderniaux P, Brouyère S, Fowler HJ, Blenkinsop S, Therrien R, Orban P, Dassargues A (2009) Large scale surface–subsurface hydrological model to assess climate change impacts on groundwater reserves. J Hydrol 373(1):122-138, doi: 10.1016/j.jhydrol.2009.04.017

Habets F, Boé J, Déqué M, Ducharne A, Gascoin S, Hachour A, Martin E, Pagé C, Sauquet E, Terray L, Thiéry D, Oudin L,Viennot P (2013) Impact of climate change on the hydrogeology of two basins in Northern France. Clim change 121(4), 771-785, doi:10.1007/s10584-013-0934-x

Hanson B, Boniol D (1985) Potential risks to a sole-source aquifer recharge area from waste disposal activities: a case study. Hazardous Wastes in Ground Water: A Soluble Dilemma. National Water Well Association, Dublin OH. 1985. p78-86.

Healy RW (2010) Estimating groundwater recharge. Cambridge University Press, Cambridge.

Hidalgo HG, Dettinger MD, Cayan DR (2008) Downscaling with constructed analogues: Daily precipitation and temperature fields over the United States. California Energy Commission PIER Final Project Report CEC-500-2007-123

Hiscock K, Sparkes R, Hodgens A (2012) Evaluation of future climate change impacts on European groundwater resources. Climate change effects on groundwater resources: a global synthesis of findings and recommendations. IAH International Contributions to Hydrogeology, Taylor and Francis, London, 351-366

Hoeting JA, Madigan D, Raftery AE, Volinsky CT (1999) Bayesian model averaging: A tutorial. Statistical Science, 382–401, doi: 10.1214/ss/1009212814

Huntington TG (2006) Evidence for intensification of the global water cycle: review and synthesis. J Hydrol 319(1):83-95, doi: 10.1016/j.jhydrol.2005.07.003

Holman IP, Allen DM, Cuthbert MO, Goderniaux P (2012) Towards best practice for assessing the impacts of climate change on groundwater. Hydrogeol J 20(1):1-4, doi: 10.1007/s10040-011-0805-3

Houghton JT, Meira Filho LG, Callander BA, Harris N, Katten-berg A, Maskell K (1996) Climate change 1995: The science of climate change. contribution of working group I to the second assessment report of the Intergovernmental Panel on Climate Change (Vol. 2). Cambridge University Press,UK.pp. 336

Iglewicz B, Hoaglin DC (1993) How to detect and handle outliers (Vol. 16). Milwaukee (Wisconsin): ASQC Quality Press, doi: 10.2307/1269377

Jackson CR, Meister R, Prudhomme C (2011) Modelling the effects of climate change and its uncertainty on UK Chalk groundwater resources from an ensemble of global climate model projections. J Hydrol 399(1):12-28, doi: 10.1016/j.jhydrol.2010.12.028

Jin S, Yang L, Danielson P, Homer C, Fry J, Xian G (2013) A comprehensive change detection method for updating the National Land Cover Database to circa 2011. Remote Sens Environ, 132: 159 – 175, doi:10.1016/j.rse.2013.01.012

Jyrkama MI, Sykes JF (2007) The impact of climate change on spatially varying groundwater recharge in the grand river watershed (Ontario). J Hydrol 338(3):237-250, doi: 10.1016/j.jhydrol.2007.02.036

Jyrkama MI, Sykes JF (2007) The impact of climate change on spatially varying groundwater recharge in the grand river watershed (Ontario). J Hydrol 338(3):237-250, doi: 10.1016/j.jhydrol.2007.02.036

Liang Z, Wang D, Guo Y, Zhang Y, Dai R (2013) Application of bayesian model averaging approach to multimodel ensemble hydrologic forecasting. J Hydrol Eng-ASCE, 18(11), 1426-1436, doi:10.1061/(ASCE)HE.1943-5584.0000493

Khire, M. V., Benson, C. H., and Bosscher, P. J., 1997. Water balance modeling of earthen final covers. J Geotech Geoenviron 123(8):744-754, doi:10.1061/(ASCE)1090-0241(1997)123:8(744)

Kirshen PH (2002) Potential impacts of global warming on groundwater in Eastern Massachusetts. J Water Res. Pl-ASCE. 128(3):216-226, doi: 10.1061/(ASCE)0733-9496(2002)128:3(216)

Kruger A, Ulbrich U, Speth P (2001) Groundwater recharge in Northrhine-Westfalia predicted by a statistical model for greenhouse gas scenarios. Phys Chem Earth Pt B 26(11–12):853–861, doi: 10.1016/s1464-1909(01)00097-1

Lavalle C, Micale F, Houston, TD, Camia A, Hiederer R, Lazar C, Conte C, Amatulli G, Genovese G (2009) Climate change in Europe. 3. Impact on agriculture and forestry. A review. Agron Sustain Dev 29(3):433-446, doi:10.1051/agro/2008068

Kay AL, Davies HN, Bell VA, Jones RG (2009) Comparison of uncertainty sources for climate change impacts: flood frequency in England. Clim Change 92(1-2), 41-63, doi:10.1007/s10584-008-9471-4

Kass R, Raftery A (1995) Bayes Factors. JASA, 90(430), doi:10.1080/01621459.1995.10476572

Katz RW, Craigmile PF, Guttorp P, Haran M, Sansó B, Stein M L (2013) Uncertainty analysis in climate change assessments. Nat Clim Change, 3(9), 769-771, doi:10.1038/nclimate1980

Knutti R, Furrer R, Tebaldi C, Cermak J, Meehl GA (2010) Challenges in combining projections from multiple climate models. J Clim, 23(10), 2739-2758, doi:10.1175/2009JCLI3361.1

Li X, Tsai FT-C (2009) Bayesian model averaging for groundwater head prediction and uncertainty analysis using multimodel and multimethod. Water Resour Res, 45(9), doi:10.1029/2008WR007488, 2009

Leonard R, Kuzelka B, Seacrest S (1999) Groundwater–climate change interactions. Proc., Specialty Conference on Potential Consequences of Climate Variability and Change to Water Resources of the United States, American Water Resources Association, Bethesda, Md. pp. 122.

Lerner DN, Issar A, Simmers I (1990) Groundwater recharge: a guide to understanding and estimating natural recharge. International Association of Hydrogeologists, Vol 8, Heise, Hannover, pp. 345

Lerner DN (2002) Identifying and quantifying urban recharge: a review. Hydrogeol J 10(1):143-152, doi: 10.1007/s10040-001-0177-1

Loaiciga HA, Maidment DR Valdes JB (2000) Climate-change impacts in a regional karst aquifer, Texas, USA. J Hydrol 267: 173-194, 10.1016/s0022-1694(99)00179-1

Loaiciga HA (2003) Climate change and ground water. Ann Assoc Am Geogr 93(1):30-41, doi: 10.1111/1467-8306.93103

Makanjuola M, David J, Makar T, Ahane I (2012) Estimation of groundwater recharge at NCAM, Ilorin for improved irrigation managment. C J Eng Sci 6(3):1-6

Maurer E, Wood A, Adam J, Lettenmaier, D, Nijssen B (2002). A long-term hydrologically based dataset of land surface fluxes and states for the conterminous United States. J Climate 15(22):3237-3251, doi: 10.1175/1520-0442(2002)015<3237:althbd>2.0.co;2

Maurer EP, Brekke L, Pruitt T, Duffy PB (2007) Fine resolution climate projections enhance regional climate change impact studies. Eos, Trans Am Geophys Union, 88(47), 504-504, doi:10.1029/2007EO470006

Maurer EP, Brekke L, Pruitt T, Duffy PB, Thrasher B, Long J, Arnold J et al (2013) An enhanced archive facilitating climate impacts and adaptation analysis. Bulletin of the American Meteorological Society, doi:10.1175/BAMS-D-13-00126.1

Maurer EP, Wood AW, Adam JC, Lettenmaier, DP, Nijssen B (2002). A long-term hydrologically based dataset of land surface fluxes and states for the conterminous United States. J Climate 15(22): 3237-3251, doi:10.1175/1520-0442(2002)015<3237:ALTHBD>2.0.CO;2

Maurer EP (2013) Gridded Meteorological Data: 1949-2010, Santa Clara University, http://www.engr.scu.edu/~emaurer/gridded_obs/index_gridded_obs.html. Cited 21 August 2014.

McAvaney BJ, Covert C, Joussaume S et al. (2001) Model evaluation. In: Climate Change 2001: The Scientific Basis (eds Houghton JT et al.), pp. 471–524. Cambridge University Press, New York

McCarthy JJ, Canziani OF, Leary NA, Dokken DJ, White KS (2001) Climate change 2001: impacts, adaptation, and vulnerability. contribution of Working Group II to the third assessment report of the Intergovernmental Panel on Climate Change, Cambridge University Press,UK.

McCallum JL, Crosbie RS, Walker GR, Dawes WR (2010) Impacts of climate change on groundwater in Australia: a sensitivity analysis of recharge. Hydrogeol J 18(7):1625-1638, doi: 10.1007/s10040-010-0624-y

Meinshausen M, Smith SJ, Calvin K, Daniel JS, Kainuma ML, Lamarque JF, Matsumoto K, Montzka SA, Raper SC, Riahi K, Thomson A, Velders GJ, van Vuuren DP (2011) The RCP greenhouse gas concentrations and their extensions from 1765 to 2300. Clim Change, 109, 213-241, doi:10.1007/s10584-011-0156-z.

Mileham L, Taylor RG, Todd M, Tindimugaya C, Thompson J (2009) The impact of climate change on groundwater recharge and runoff in a humid, equatorial catchment: Sensitivity of projections to rainfall intensity. Hydrolog Sci J 54(4):727-738. doi:10.1623/hysj.54.

Min SK, Simonis D, Hense A (2007) Probabilistic climate change predictions applying Bayesian model averaging. Philos Trans Roy Soc A, 365(1857), 2103-2116, doi:10.1098/rsta.2007.2070

Moss RH, Edmonds JA, Hibbard KA, Manning MR, Rose SK, Van Vuuren D P, Carter TR et al. (2010) The next generation of scenarios for climate change research and assessment. Nature, 463(7282), 747-756, doi:10.1038/nature08823

Mu Q, Heinsch FA, Zhao M, Running SW (2007) Development of a global evapotranspiration algorithm based on MODIS and global meteorology data. Remote Sens. Environ 111(4):519-536, doi:10.1016/j.rse.2007.04.015

Mu Q, Zhao M, Running SW (2011) Improvements to a MODIS global terrestrial evapotranspiration algorithm. Remote Sens Environ 115(8):1781-1800, doi:10.1016/j.rse.2011.02.019

Murphy JM., Booth BB, Collins M, Harris GR, Sexton DM, Webb MJ (2007) A methodology for probabilistic predictions of regional climate change from perturbed physics ensembles. Phil Trans Royal Soc A: Mathematical, Physical and Engineering Sciences 365(1857), 1993-2028, doi:10.1098/rsta.2007.2077

Najafi MR, Moradkhani H, Jung WI (2010). Combined effect of global climate projection and hydrologic model uncertainties on the future changes of Streamflow. ASCE Conf Proc, 371(10):1. doi:10.1061/41114(371)10.

Nakicenovic N, Swart R (eds) (2000) Special report on emissions scenarios. A special report of Working Group III of the Intergovernmental Panel on Climate Change. IPCC, University Press, Cambridge

Neukum C, Azzam R (2012) Impact of climate change on groundwater recharge in a small catchment in the Black Forest, Germany. Hydrogeol J 20(3):547-560. doi:10.1007/s10040-011-0827-x

Ng GHC, McLaughlin D, Entekhabi D, Scanlon, BR (2010) Probabilistic analysis of the effects of climate change on groundwater recharge. Water Resour Res 46(7)

NLCD (2011) USDA/NRCS National Geospatial Center of Excellence, 2011 National Land Cover Dataset, http://datagateway.nrcs.usda.gov/ Cited 25 Febuary 2014

NRCS (1986) Urban hydrology for small watersheds. US Department of Agriculture, Natural Resources Conservation Service, Technical Release 55, 164p.

NRCS (2013) U.S. General Soil Map (STATSGO2).Soil Survey Staff, Natural Resources Conservation Service, United States Department of Agriculture , <http://soildatamart.nrcs.usda.gov >, (Feb. 25, 2013)

NRCS (2014) Soil Survey Geographic (SSURGO). Soil Survey Staff, Natural Resources Conservation Service, United States Department of Agriculture , http://sdmdataaccess.nrcs.usda.gov/. Cited 25 January 2014

Oubeidillah AA, Kao SC, Ashfaq M, Naz BS, Tootle G (2014) A large-scale, high-resolution hydrological model parameter data set for climate change impact assessment for the conterminous US, Hydrol. Earth Syst. Sci., 18, 67–84, doi:10.5194/hess- 18-67-2014

Peyton RL, Schroeder PR (1988) Field verification of HELP model for landfills. J Environ Eng-ASCE. 114(2):247-269, doi 10.1061/(ASCE)0733-9372(1988)114:2(247)

Pierce DW, Barnett TP, Santer BD, Gleckler PJ (2009) Selecting global climate models for regional climate change studies. Proc Natl Acad Sci, USA, 106(21), 8441-8446. doi:10.1073/pnas.0900094106

Price CP, Nakagaki N, Hitt KJ, Clawges RM (2006) Enhanced historical land-use and land-cover datasets of the U.S. Geological Survey. U.S. Geological Survey Data Series 240, digital maps, < http://pubs.usgs.gov/ds/2006/240>, (March. 14, 2012)

Prudhomme C, Davies H (2009) Assessing uncertainties in climate change impact analyses on the river flow regimes in the UK. Part 2: future climate. Clim Change 93(1-2), 197-222, doi:10.1007/s10584-008-9461-6

Raftery AE, Zheng Y (2003) Discussion: Performance of Bayesian model averaging. J Am Statist Assoc 98(464), 931-938, doi: 10.1198/016214503000000891

Raftery AE, Gneiting T, Balabdaoui F, Polakowski M (2005) Using Bayesian model averaging to calibrate forecast ensembles. Monthly Weather Review, 133(5), 1155-1174, doi:10.1175/MWR2906.1

Raposo JR, Dafonte J, Molinero J (2013) Assessing the impact of future climate change on groundwater recharge in Galicia-Costa, Spain. Hydrogeol J 21(2):459-479, doi: 10.1007/s10040-012-0922-7

Richardson CW, Wright DA (1984) WGEN: A model for generating daily weather variables. U.S. Department ofAgriculture, Agricultural Research Service, ARS-8, pp.83.

Risser DW, Conger RW, Ulrich JE, Asmussen MP (2005) Estimates of ground-water recharge based on streamflow-hydrograph methods: Pennsylvania. U.S. Geological Survey Open-File Report 2005-1333. Reston, Virginia.

Ritchie JT (1972) A model for predicting evaporation from a row crop with incomplete
Cover. Water Resour Res 8(5), 1204-1213, 10.1029/wr008i005p01204

Rogelj J, Meinshausen M, Knutti R (2012) Global warming under old and new scenarios using IPCC climate sensitivity range estimates. Nat Clim Change 2(4): 248-253, doi:10.1038/nclimate1385

Robbins K (2013) Southern Regional Climate Center, Louisiana State University, http://www.srcc.lsu.edu, Cited 23 July 2013

Scanlon BR, Healy RW, Cook PG (2002a) Choosing appropriate techniques for quantifying groundwater recharge. Hydrogeol J 10(2):18–39, doi: 10.1007/s10040-002-0200-1

Scanlon BR, Dutton, A, Sophocleous MA (2002b) Groundwater recharge in Texas. Bureau of Economic Geology, University of Texas at Austin.

Schroeder PR, Dozier TS, Zappi PA, McEnroe BM, Sjostrom JW, Peyton RL (1994) The hydrologic evaluation of landfill performance (HELP) model: Engineering documentation for version 3. EPA/600/R-94/168b, US Environmental Protection Agency Office of Research and Development, Washington, DC.

Schroeder PR., Peyton RL (1987) Verification of the hydrologic evaluation of landfill performance (HELP) model using field data., EPA/600/S2-87/050,Hazardous Waste Engineering Research Laboratory, Office of Research and Development, US Environmental Protection Agency, Cincinnati, OH.

Schmittner A, Latif M, Schneider B (2005) Model projections of the North Atlantic thermohaline circulation for the 21st century assessed by observations. Geophys Res Lett, 32(23), doi:10.1029/2005GL024368

Schibek J, Allen DM (2006) Modelled impacts of predicted climate change on recharge and groundwater levels. Water Resour Res 42(11):W11405. doi:10.1029/2005WR004742

Scibek J, Allen DM, Cannon AJ, Whitfield PH (2007) Groundwater–surface water interaction under scenarios of climate change using a high-resolution transient groundwater model. J Hydrol 333(2):165-181, doi 10.1016/j.jhydrol.2006.08.005

Scott CA, Megdal S, Oroz LA, Callegary J, Vandervoet P (2012) Effects of climate change and population growth on the transboundary Santa Cruz aquifer. Clim Res 51(2):159

Serrat-Capdevila A, Valdés JB, Pérez JG, Baird K, Mata LJ Maddock Iii T (2007) Modeling climate change impacts - and uncertainty - on the hydrology of a riparian system: The San Pedro Basin (Arizona/Sonora). J Hydrol 347(1-2):48-66, doi: 10.3354/cr01061

Smith RL, Tebaldi C, Nychka D, Mearns L O (2009) Bayesian modeling of uncertainty in ensembles of climate models. JASA, 104(485), 97-116, doi:10.1198/jasa.2009.0007

Sophocleous MA (1991) Combining the soil water balance and water-level fluctuation methods to estimate natural groundwater recharge: practical aspects. J Hydrol 124(3):229-241, doi: 10.1016/0022-1694(91)90016-b

Solomon S, Qin D, Manning M, Marquis M, Averyt KB, Tignor M, Miller HL,Chen Z (2007) Climate change 2007-the physical science basis. Working group I contribution to the fourth assessment report of the IPCC (Vol. 4), Cambridge University Press, Cambridge, UK.

Stocker T, Dahe Q, Plattner GK, Tignor M, Midgley P (2010) IPCC Expert Meeting on Assessing and Combining Multi Model Climate Projections. Boulder, Colorado, USA, 25-27

Stoll S, Hendricks Franssen, HJ, Butts M, Kinzelbach W (2011) Analysis of the impact of climate change on groundwater related hydrological fluxes: a multi-model approach including different downscaling methods. Hydrol Earth Syst Sci 15(1):21-38, doi: 10.5194/hess-15-21-2011

Taylor KE, Stouffer RJ, Meehl GA (2012) An Overview of CMIP5 and the Experiment Design, B Am Meteorol Soc, 93(4), 485-498, doi:10.1175/BAMS-D-11-00094.1

Tebaldi C, Smith RL, Nychka D, Mearns LO (2005) Quantifying uncertainty in projections of regional climate change: a Bayesian approach to the analysis of multi-model ensembles. J Clim,18(10), 1524–1540, doi:10.1175/JCLI3363.1

Tebaldi C, Knutti R (2007) The use of multi-model ensemble in probabilistic climate projections. Phil Trans R Soc A, 365(1857), 2053–2075, doi:10.1098/rsta.2007.2076

Teng J, Vaze J, Chiew FHS, Wang B, Perraud JM (2012) Estimating the Relative Uncertainties Sourced from GCMs and Hydrological Models in Modeling Climate Change Impact on Runoff. J Hydrometeor, 13 122–139, doi:10.1175/JHM-D-11-058.1

Tilahun K, Merkel BJ (2009) Estimation of groundwater recharge using a GIS-based distributed water balance model in Dire Dawa, Ethiopia. Hydrogeol J, 17(6), 1443-1457, doi: 10.1007/s10040-009-0455-x

Toews MW, Allen DM (2009) Evaluating different GCMs for predicting spatial recharge in an irrigated arid region. J Hydrol 374(3):265-281, doi:10.1016/j.jhydrol.2009.06.022

Tsai FT-C, Elshall AS (2013) Hierarchical Bayesian model averaging for hydrostratigraphic modeling: uncertainty segregation and comparative evaluation. Water Resour Res, 49 (9), 5520–5536., doi:10.1002/wrcr.20428.

Tsai FT-C (2010) Bayesian model averaging assessment on groundwater management under model structure uncertainty. Stochastic Environ Res Risk Assess, 24(6), 845–861, doi:10.1007/s00477-010-0382-3

Tsai FT-C, Li X (2008a) Inverse groundwater modeling for hydraulic conductivity estimation using Bayesian model averaging and variance window. Water Resour Res, 44(9), doi:10.1029/2007WR006576

Tsai FT-C, Li X (2008b). Multiple Parameterization for Hydraulic Conductivity Identification, Ground Water, 46(6), 851-864. doi:10.1111/j.1745-6584.2008.00478.x

United Nations (1998), Kyoto Protocol to the United Nations Framework Convention on Climate Change, UNFCC, Geneva

UNFCCC, 2015. http://unfccc.int - Official website of the United Nations Framework Convention on Climate Change (UNFCCC). Cited 17 Fenruary 2015.

USDA, Soil Conservation Service. (1985). National engineering handbook, section 4, hydrology. US Government Printing Office, Washington, D.C.

USBR (2013). Downscaled CMIP3 and CMIP5 Climate and Hydrology Projections: Release of Downscaled CMIP5 Climate Projections, Comparison with preceding Information, and Summary of User Needs, prepared by the U.S. Department of the Interior, Bureau of Reclamation (USBR), Technical Services Center, Denver, Colorado. 47pp.

U.S.Congress (1996) The safe drinking water act. Public Law, 104-182.

U.S. Department of Agriculture, Soil Conservation Service (1985) National engineering handbook, section 4, hydrology. US Government Printing Office, Washington, D.C.

Vaccaro JJ (1992) Sensitivity of groundwater recharge estimates to climate variability and change, Columbia Plateau, Washington. J Geophys Res 97 (D3): 2821–2833, doi: 10.1029/91jd01788

Van Vuuren DP, Edmonds J, Kainuma MLT, Riahi K, Thomson A, Matsui T, Hurtt G, Lamarque J-F,Meinshausen M, Smith S, Grainer C, Rose S, Hibbard KA, Nakicenovic N, Krey V, Kram T (2011). Representative concentration pathways: An overview. Clim Change 109, 5-31, doi:10.1007/ s10584-011-0148-z

Vrugt JA, Robinson BA (2007) Treatment of uncertainty using ensemble methods: comparison of sequential data assimilation and Bayesian model averaging. Water Resour Res 43(1). doi:10.1029/2005WR004838, doi:10.1029/2005WR004838

Wagener T, Gupta HV (2005) Model identification for hydrological forecasting under uncertainty. Stoch Env Res Risk A, 19(6), 378-387, doi:10.1007/s00477-005-0006-5

Watson RT, Zinyowera MC, Moss RH (1998) The regional impacts of climate change: an assessment of vulnerability. A special report of the IPCC Working Group II. Cambridge University Press, UK.

Wegehenkel M, Kersebaum KC (2009) An assessment of the impact of climate change on evapotranspiration, groundwater recharge, and low-flow conditions in a mesoscale catchment in Northeast Germany. J. Plant Nutr. Soil Sci 172(6):737-744, doi: 10.1002/jpln.200800271

Waugh, DW, Eyring V (2008) Quantitative performance metrics for stratospheric-resolving chemistry-climate models. Atm Chem Phys, 8(18), 5699-5713, doi:10.5194/acp-8-5699-2008

Wilby R L, Harris I (2006) A framework for assessing uncertainties in climate change impacts: Low-flow scenarios for the River Thames, UK. Water Resour Res 42(2), doi:10.1029/2005WR004065

Woldemeskel FM, Sharma A, Sivakumar B, Mehrotra R (2012) An error estimation method for precipitation and temperature projections for future climates J Geophys Res: Atmospheres (1984–2012), 117(D22), doi:10.1029/2012JD018062

Wolock, D. M. (2003). "Base-flow index grid for the conterminous United States: U.S. Geological Survey Open-File Report 03–263, digital data set.", <http://water.usgs.gov/lookup/getspatial?bfi48grd>, (June. 28, 2013).

Yip S, Ferro CAT, Stephenson DB, Hawkins E (2011) A simple, coherent framework for partitioning uncertainty in climate predictions. J. Clim., 24(17), 4634–4643, doi:10.1175/2011JCLI4085.1

Yusoff I, Hiscock KM, Conway D (2002) Simulation of the impacts of climate change on groundwater resources in eastern England. In: Hiscock KM, Rivett MO, Davidson RM (eds) Sustainable groundwater development. Geol Soc Lond Spec Publ 193:325-344, doi: 10.1144/gsl.sp.2002.193.01.24

Yuan H, Dai Y, Xiao Z, Ji D, Shangguan W (2011) Reprocessing the MODIS leaf area index products for land surface and climate modelling. Remote Sens Environ 115(5):1171-1187, doi:10.1016/j.rse.2011.01.001

Yun WT, Stefanova L, Krishnamurti TN (2003) Improvement of the multimodel superensemble technique for seasonal forecasts. J Clim, 16(22), 3834-3840, doi:10.1175/1520-0442(2003)016<3834:IOTMST>2.0.CO;2

Zhang X, Srinivasan R, Bosch D (2009) Calibration and uncertainty analysis of the SWAT model using Genetic Algorithms and Bayesian Model Averaging. J Hydrol, 374(3), 307-317, doi:10.1016/j.jhydrol.2009.06.023

Vita

Ehsan Beigi was born in Tehran, Iran in December, 1981. He received his bachelor's degree in Civil Engineering from Isfahan University of Technology in December, 2005. After working as a Civil Engineer in wastewater treatment plant project, in September, 2007 he started a MS program in Civil Engineering/Water Resources Management in Sharif University of Technology. He received his MS degree in July, 2010 and moved to Baton Rouge Louisiana in January 2011 to start his Ph.D. in Louisiana State University. Ehsan Beigi is currently a candidate for the degree of Doctor of Philosophy in Civil Engineering.